

Review

# Methane Combustion over the Porous Oxides and Supported Noble Metal Catalysts

Hongxia Lin, Yuxi Liu, Jiguang Deng, Lin Jing and Hongxing Dai \*

Beijing Key Laboratory for Green Catalysis and Separation, Key Laboratory of Beijing on Regional Air Pollution Control, Key Laboratory of Advanced Functional Materials, Education Ministry of China, Laboratory of Catalysis Chemistry and Nanoscience, Department of Chemical Engineering, Faculty of Environment and Life, Beijing University of Technology, Beijing 100124, China

\* Correspondence: hxdai@bjut.edu.cn; Tel.: +86-106739-6118; Fax: +86-106739-1983

**Abstract:** Methane is the most stable hydrocarbon with a regular tetrahedral structure, which can be activated and oxidized above 1000 °C in conventional combustion. Catalytic oxidation is an effective way to eliminate lean methane under mild conditions, and the key issue is to develop the catalysts with high efficiencies, good stability, and high selectivities. Catalytic combustion of low-concentration methane can realize the light-off and deep conversion at low temperatures, thus achieving complete combustion with fewer byproducts below 500 °C. This review article summarizes the recent advances in preparation of ordered porous oxides and supported noble metal catalysts and their methane combustion applications. The results reveal that the superior performance (good hydrothermal stability and excellent moisture- or sulfur-resistant behavior) is associated with the well-ordered and developed three-dimensional porous structure, large surface area, ultrahigh component dispersion, fast mass transfer, low-temperature reducibility, reactant activation ability, and strong interaction between metal and support. In addition, the development trend of porous oxides for industrial applications in the future is also proposed.

**Keywords:** methane combustion; porous catalyst preparation; ordered porous metal oxides; supported noble metals; hydrothermal stability; sulfur dioxide resistance



**Citation:** Lin, H.; Liu, Y.; Deng, J.; Jing, L.; Dai, H. Methane Combustion over the Porous Oxides and Supported Noble Metal Catalysts. *Catalysts* **2023**, *13*, 427. <https://doi.org/10.3390/catal13020427>

Academic Editor: Leonarda Liotta

Received: 10 January 2023

Revised: 10 February 2023

Accepted: 13 February 2023

Published: 16 February 2023



**Copyright:** © 2023 by the authors. Licensee MDPI, Basel, Switzerland. This article is an open access article distributed under the terms and conditions of the Creative Commons Attribution (CC BY) license (<https://creativecommons.org/licenses/by/4.0/>).

## 1. Introduction

Methane is one of the cleanest fuel sources and can play an irreplaceable role in achieving carbon neutrality. As the main component of natural gas, incomplete CH<sub>4</sub> combustion causes resource waste and aggravates air pollution. Methane is inflammable and explosive when it is accumulated to a certain volume fraction, which causes serious property damage and casualties. The global warming potential of methane is at least 72 times higher than that of CO<sub>2</sub> over the last 20 years, which is related to the strong greenhouse effect.

Methane is the most stable hydrocarbon with a regular tetrahedral structure, which is difficult to activate and oxidize under mild conditions. Conventional combustion of natural gas requires a high temperature of above 1500 °C, which generates a large number of water vapor, sulfur dioxide, and insufficient combustion products (CO) as well as NO<sub>x</sub> (formed via the reaction of N<sub>2</sub> and O<sub>2</sub> at high temperatures). In the 1970s, Pfefferle [1] proposed a heterogeneous catalytic gas-phase combustion process to realize effective combustion of hydrocarbons and low emissions of pollutants. Catalytic combustion remarkably decreases CH<sub>4</sub> oxidation temperatures, which can reduce or avoid the formation of NO<sub>x</sub> and CO. The adsorption of NO on the active component (MnO<sub>2</sub>) and support (TiO<sub>2</sub>) was studied by the density functional theory calculations [2]. NO was adsorbed at the top sites of Mn Lewis site in the way of the O-down orientation. Although there was an electron transfer between NO and Mn, NO adsorption belonged to a weak physisorption. In the case of NO adsorption, the hybridization between Ti and NO could be found, corresponding

to a strong chemisorption. Striking is the positive influence of the catalyst regeneration by introducing  $\text{NO}_x$  for methane conversion in the transient reactivation experiment [3]. The oxidation of NO and reduction of  $\text{NO}_2$  on the catalyst surface during the methane conversion process could be able to reactivate the catalyst. Reactivation of a catalyst deactivated under the lean-burn conditions could be achieved by adding NO and/or  $\text{NO}_2$ . Öcal et al. [4] investigated the influence of high NO amount (2.3 vol%) on catalytic performance of the Pd/hexaaluminate catalyst. Increased activity was found in the presence of NO above 400 °C. The authors attributed such a behavior to the increased reoxidation of Pd during the  $\text{CH}_4$  oxidation process or to the formation of the highly reactive  $\text{O}^*$  species on the catalyst surface from the dissociation of  $\text{NO}_2$ .

$\text{CH}_4$  is weakly adsorbed on the catalyst surface, while  $\text{H}_2\text{O}$  and  $\text{SO}_2$  display strong adsorption, which induces poisoning and deactivation of the catalyst. Design and preparation of a high-performance catalyst with good low-temperature activity, excellent thermal stability, high selectivity, and admirable  $\text{H}_2\text{O}$  and  $\text{SO}_2$  resistance are crucial to achieve  $\text{CH}_4$  elimination.

A thermo-catalytic methane decomposition reactor system is thoroughly discussed to achieve optimized heat management and better methane conversion. Raza et al. [5] proposed a methane decomposition reactor system configuration for industrial and commercial application, and gave the involved working principle, technical advantages, and limitation. A suitable catalyst used in a reactor system can decrease the activation energy and accelerate the reaction process; however, catalyst deactivation and huge energy consumption are still big challenges to be overcome.

The influencing factors of catalytic activity include the reactant diffusion from the gas phase to the catalyst surface, the adsorption and activation of reactants at the surface active sites, oxidation of reactants with oxygen species at the active sites to generate products, desorption of products from the active centers, and diffusion of products from the catalyst surface to the gas phase. Generating a porous structure is one of the most available strategies to develop the high-surface-area materials, so that the number of the active sites can be increased and the catalytic activity is, thus, improved significantly. The large surface areas of porous materials are beneficial for adsorption of the reactants as well as desorption and diffusion of the products, which reduces the mass transfer resistance of methane and  $\text{O}_2$  in the reaction system and maximizes the contact capability of reactants with the surface active centers substantially. Lu and coworkers [6] prepared mesoporous  $\text{LaCoO}_3$  via a nanocasting route using an ordered mesoporous cubic (*Ia3d*) vinyl silica as template. The ordered three-dimensional mesostructured  $\text{LaCoO}_3$  displayed a high surface area of  $96.7 \text{ m}^2/\text{g}$  and showed a much lower light-off temperature of 335 °C. Further analysis demonstrated that the large surface area and well-ordered mesopore structure were associated with formation of the high-valence cobalt ions and abundant  $\text{O}_2^{2-}/\text{O}^-$  species. Hence, the mesostructured  $\text{LaCoO}_3$  catalyst exhibited a superior activity for deep oxidation of methane.

There are two main typical catalysts for methane oxidation: (i) transition-metal oxides (single- and mixed-metal oxides) and (ii) supported noble metals. The essence of improved oxidation–reduction (redox) ability of metal oxides is to optimize the oxygen storage–release properties and oxygen transfer capability, and the role of metal oxides with a high oxygen storage capacity is prospected to allow the metal to keep sustainable work in cycle. Transition-metal oxides possess multiple oxidation states and flexibly realize the oxidation and reduction processes between different cation valence states. The release of lattice oxygen and formation of oxygen vacancies in a redox cycle generate a large number of surface-adsorbed oxygen species, which are attributed to the adsorption and activation of reactants and  $\text{O}_2$ . Catalytic performance of transition-metal oxides is related to their physicochemical properties, such as surface areas, defects, redox ability, crystallinity, exposed crystal planes, and morphologies. Transition-metal oxides display poor thermal stability, whose phase transitions induced by treating with the fluctuating reaction conditions significantly affect their catalytic activities. Li and coworkers [7,8]

prepared spinel-structured  $\text{Co}_3\text{O}_4$  octahedra with a relatively strong (111) diffraction signal via a facile redox-precipitation route, which showed an inert catalytic activity for methane combustion. High-resolution transmission electron microscopic (HRTEM) studies indicated that irregular  $\text{Co}_3\text{O}_4$  nanoparticles (NPs) with predominantly exposed other crystal facets presented a more consistent activity compared with the  $\text{Co}_3\text{O}_4$  octahedra with exposed low Miller-index (111) facets that possess the lowest surface energy. The same group also fabricated manganese–cobalt oxides with various Co/Mn molar ratios to investigate the oxygen mobility that influenced methane oxidation rates below 320 °C [9]. The addition of manganese to the spinel-structured cobalt oxide multiplied the crystal defections which was contributed to an enlarged number of octahedrally-coordinated divalent cobalt ions. The –OH groups in the Mn-doped catalysts further demonstrated the dehydroxylation by the doping of Mn to produce an optimal catalyst for the combustion of methane. Similarly to the previous work, the same group pointed out that cobalt–chromium oxide with Co/Cr molar ratio = 1/2 showed excellent resistance to water vapor poisoning [10]. The investigation of excellent methane oxidation activity of the  $\text{Co}_1\text{Cr}_2$  catalyst revealed that the higher valence  $\text{Cr}^{3+}$  and  $\text{Cr}^{6+}$  species and coordination number of cations significantly enhanced adsorption of the chemisorbed oxygen species.

Perovskite-type oxides are the most available catalysts which are calcined at above 850 °C, thus exhibiting the high-temperature thermal stability in  $\text{CH}_4$  oxidation. Perovskite-type oxides remain prominent among the mixed-metal oxides with a general formula of  $\text{ABO}_3$ , in which the size of A cation is bigger than that of B cation, the A-site cations are rare-earth or alkaline-earth ions that coordinate with 12 oxygen anions, whereas the B-site cations are transition-metal ions which coordinate with six oxygen anions. The mixed-metal oxides, such as  $\text{ABO}_3$ , double perovskites ( $\text{A}_2\text{BBO}_6$ ), perovskite-like oxides ( $\text{A}_2\text{BO}_4$ ), and pyrochlore ( $\text{A}_2\text{B}_2\text{O}_7$ ), are one kind of complete oxidation catalytic material with abundant oxygen vacancies that can activate  $\text{O}_2$  into various oxygen species, and the presence of at least two kinds of metal cations in various oxidation states achieves a facile redox cycle. Structural defects and lattice oxygen mobility that is in relation with the Mars–van Krevelen mechanism are also critical factors governing the catalytic activity. The surface-adsorbed oxygen at oxygen vacancies of the  $\text{ABO}_3$  catalysts is involved in the combustion of methane at low temperatures, while surface or bulk lattice oxygen species play an important role at high temperatures. The catalytic activity of  $\text{ABO}_3$  mainly depends on the B-site ion, while the A-site ion plays an important role in stabilizing the perovskite structure. Both A and B sites can be partially substituted by heterovalent ions to regulate distributions of the B-site cation oxidation states to promote redox property of the perovskite-structured materials. However, some poisons (e.g.,  $\text{SO}_x$ , especially the progressive sulfidation of perovskite-type oxide structures) can cause a permanent loss in catalytic activity [11,12]. Hao and coworkers [13,14] investigated partial substitution of the composite metal oxide by a transition metal (Co) to achieve superior methane oxidation performance at moderate–high temperatures. The  $\text{La}_2\text{Co}_x\text{Sn}_{2-x}\text{O}_{7-\delta}$  catalysts with a pyrochlore structure were prepared via the coprecipitation route [13]. The authors found that the doping of Co ions to the pyrochlore lattice significantly influenced the thermal stability and redox property, and increased the reduction rates and oxygen vacancy amount for  $\text{CH}_4$  oxidation. The diffusion reflectance infrared Fourier transform spectroscopic (DRIFTS) measurements indicated that the lower-energy Sn–O bond strength was weakened by Co doping to achieve easier lattice oxygen release and promoted formation of oxygen vacancies. The authors concluded that the good catalytic performance of  $\text{La}_2\text{Co}_x\text{Sn}_{2-x}\text{O}_{7-\delta}$  was associated with their high surface areas, rich oxygen vacancies generated due to Co doping, and improved redox ability. The same group also examined the effect of transition metal (Mn, Fe, Co, Ni, or Cu) doping on methane oxidation activity of  $\text{La}_2\text{Zr}_2\text{O}_7$  [14]. DRIFTS spectra revealed that the introduction of a transition metal strongly influenced catalytic activity for  $\text{CH}_4$  combustion, which was related to the Zr–O bond strength and pyrochlore phase formation temperature as well as the redox properties and crystallite sizes of the pyrochlores.

Methane is the most stable hydrocarbon and the breakdown of C–H bond is considered to be the rate-determining step for methane combustion. Noble metals possess special electron states of *d*-band, which is beneficial for the activation of the C–H bond to decrease the activation energy of methane dissociation for low-temperature oxidation. Therefore, noble metals catalysts are most widely investigated in catalytic methane combustion due to its lower light-off temperature and high resistance to carbon deposition and sulfur dioxide.

Supported noble metals are constructed to be the bifunctional catalysts which reinforce resistance of the noble metals to sintering and strengthen the cooperative effect between the metal and the substrate (i.e., the dual-site mechanism). Bifunctional catalysts exhibit enhanced thermal stability and excellent catalytic performance as well as inhibit side reactions. Small-sized noble metal NPs possess high surface energies with exceptional properties and favored reactants activation, thus showing good low-temperature activities. Cargnello et al. [15] developed a novel tactic to successfully stabilize the noble metal catalysts with ultrafine Pt dispersion without NPs agglomeration using the template and impregnation methods at high temperatures. The Pt NPs were first uniformly dispersed on the surface of the porous organic framework (POF) through a wet impregnation approach, and a new polymer solution was introduced to overlay Pt/POF samples. Then, an alumina precursor infiltrated into the channel of the polymer, and the removal of template after calcination at 600 °C realized the encapsulation of Pt NPs inside the porous alumina framework. The encapsulated Pt catalyst after sintering at 800 °C in the presence of oxygen and steam with a slight size change showed a difference of 3 °C in reaction temperature for propylene conversion compared with the fresh sample, while the conventional Pt catalyst displayed a loss of 78% Pt surface area (the average Pt size increased from 3.8 to 17.2 nm) with a conversion temperature being increased by 35 °C under the similar reaction conditions. These authors also prepared the Pd–Pt bimetallic catalysts to realize higher hydrothermal stability to inhibit PtO<sub>2</sub> consumption by inducing appropriate Pd. The encapsulated Pd–Pt bimetallic catalyst maintained a small size after treatment at 1100 °C in air and steam and did not show significant deactivation.

Another effective scheme is appreciated to enhance the catalytic performance of supported materials with less noble metal consumption by adding a small amount of a base metal to modify microstructure and redox property of the particles. Supported noble metal catalysts exhibit lower light-off temperatures and remarkable sulfur tolerance in methane combustion, while sintering under the thermal treatment conditions is well known to lead to initial small particle growth to be larger ones with irreversible catalyst deactivation. Hutchings and coworkers [16] carried out a number of valuable works on development and refinement of fabricating supported bimetallic NPs with controlled morphological properties, such as small sizes, metal oxidation states, and metal–support interaction. The introduction of a second metal was favorable for the adjustment of electronic and geometrical properties; thus, the bimetallic catalysts achieved notably enhanced catalytic activities with good stability and high selectivity. AuPd colloidal NPs with a high selectivity of 90–92% for methane transformation were synthesized via a surfactant-assisted route by using polyvinyl pyrrolidone (PVP) instead of polyvinyl alcohol (PVA) as stabilizer in the presence of O<sub>2</sub> and H<sub>2</sub>O<sub>2</sub> [17]. The mechanism was revealed to be radical-based due to the presence of both •OH and •CH<sub>3</sub> radicals during the reaction process. Furthermore, O<sub>2</sub> instead of H<sub>2</sub>O<sub>2</sub> was confirmed to be the oxidant by <sup>18</sup>O<sub>2</sub> labeling. The primary CH<sub>3</sub>OOH was produced by recombination of •CH<sub>3</sub> with the dissolved O<sub>2</sub>; thus, promoted oxygen incorporation through generation of the CH<sub>3</sub>OO• radicals could be achieved by inducing O<sub>2</sub>.

In summary, porous transition-metal oxides with good intrinsic activities can be used to disperse and stabilize the active noble metal phases, thus promoting improvements in selectivity and activity of the supported noble metal catalysts and in the meanwhile reinforcing the optimized utilization of noble metals. A three-dimensionally well-ordered porous structure facilitates adsorption and diffusion of the reactants and O<sub>2</sub> molecules, and the facile mass transfer, large surface area, increased active sites, and ultrahigh ac-

tive noble metals dispersion are responsible for the excellent catalytic performance and good hydrothermal stability of porous transition-metal oxides-supported noble metals for CH<sub>4</sub> combustion. Dai and coworkers [18–28] systematically investigated multifunctional metal oxides with porous structures and generated a number of high-surface-area 3DOM-structured porous-oxides-supported noble metal materials (e.g., CoPd/3DOM CeO<sub>2</sub> [27], AuPd/meso-Co<sub>3</sub>O<sub>4</sub> [28], meso-PdPt [29], and PdPt/3DOM LaMnAl<sub>11</sub>O<sub>19</sub> [20]) using the surfactant-assisted PMMA- or KIT-6-templating methods in the last 15 years. The same group demonstrated that large surface area and well-developed pore architecture were the key factors for the high performance of the catalysts in methane combustion. The surfactants were anchored by the noble metals and removed after calcination; thus, noble metal NPs occupied partial adsorption sites of pore structures with high dispersion and smaller sizes. The modification of noble metal NPs and the reasonable specific support remarkably promoted the resistance to sintering, and the addition of a base metal to noble metal(s) improved the hydrothermal stability with a high utilization efficiency of noble metals.

In the past years, several reviews on catalytic methane combustion have been reported in the literature [30–34]. For example, Ciuparu et al. [30] reviewed the Pd-based catalysts for methane conversion and discussed the catalytic performance, redox mechanism and CH<sub>4</sub> activation at the PdO site. The kinetics of methane combustion and the sulfur-dioxide-poisoning behaviors, as well as the effect of metal NPs on catalytic performance of the noble metal catalysts, were reported [31]. Yang et al. summarized the outstanding methane oxidation activities of nanostructured perovskite oxides and proposed the novel catalysts design strategy via lattice oxygen activation, lattice oxygen mobility, and materials morphology engineering [32]. Bashan et al. reported the perovskite preparation methods and the substitution effects of the doped perovskites as well as the sulfur-dioxide-poisoning behaviors of the perovskite catalysts [33]. Nkinahamira et al. summarized the noble-metals- and transition-metal-based catalysts for methane activation and discussed physicochemical properties of the promoters, such as reduction/oxidation potential, acidity/basicity, reducibility, and oxygen storage capacity [34].

Generally speaking, CH<sub>4</sub> can be adsorbed and activated on the transition-metal oxides and supported noble metals catalysts. In a view of relevant studies, significant efforts were emphasized to synthesize numerous novel catalysts with excellent performance and protected active sites. Generating a porous structure is one of the most available strategies to develop the high-surface-area materials, so that the number of active sites can be increased and the catalytic activity is thus improved significantly. Up to now, however, a systematic and comprehensive review on catalytic materials with well-ordered meso- or macroporous structure and large-surface-area supports to facilitate uniform and ultrahigh noble metal dispersion and low loadings has not been seen in the literature. Hence, such a review that summarizes the recent advances in ordered meso- and macroporous oxides and supported noble metals catalysts for methane complete oxidation is highly needed.

In this review article, we focus on the recent advancements in synthesis of porous single- and mixed-transition-metal oxides and supported transition-metal oxides or noble metals and their catalytic applications in CH<sub>4</sub> combustion. The overview and advances in nanoporous metal oxide fabrication, redox properties of the catalysts, and structure–performance relationships are briefly summarized. In addition, limitations and promising work are also proposed for further development and industrial applications of the catalytic materials.

## 2. Synthesis of Porous Composite Metal Oxides

### 2.1. Preparation of Templates

The template synthesis method is an important route for nanocomposites fabrication using the nanostructural, shape-controlled, and low-cost solid or colloidal crystals as a template. The related materials are first deposited into the holes or on the surface of the template via the physical or chemical routes, and the template is then removed to obtain the nanomaterials with the standard template-specific morphologies and controlled

porosity. The template route is the most frequently used strategy to design and construct multifunctional materials with specific properties and pore-structure morphologies to meet the actual applications. Various templates, such as activated carbon, silicas (SBA-15, KIT-6, and silica xerogel), and colloidal crystals [35], are employed to assist the preparation of ordered porous materials.

Most of the three-dimensionally ordered macroporous (3DOM) materials are synthesized by the colloidal-crystal-templating method. The colloidal crystal templates, such as polystyrene (PS), poly(methyl methacrylate) (PMMA), poly(styrene-methyl methacrylate-acrylic acid), and SiO<sub>2</sub> colloidal microspheres, can be fabricated simply, accurately, and uniformly on a laboratory scale, and are the most commonly used for preparing well-constructed 3DOM materials [36]. The 3DOM materials were first successfully generated via a colloidal crystal template approach in the 1990s [37]. The as-obtained material displayed a three-dimensionally ordered arrangement of pore structures where the average pore sizes were all over 50 nm (up to a few microns), and avoided the shortcomings that molecular sieves and mesoporous materials with small pore structures did not allow macromolecules to enter the cavities. Usually, the colloidal microspheres used as the template are chemically stable and readily impregnated by the precursor solution. The pore diameter of a 3DOM material can be controlled by regulating the average particle size of colloidal microspheres. PS and PMMA microspheres are usually synthesized via the emulsion polymerization [38] or dispersion polymerization process [39], whereas SiO<sub>2</sub> colloidal microspheres are usually obtained using the classical Stöber method [40]. SiO<sub>2</sub> microspheres are resistant to high temperatures and a weaker pore shrinkage appears after the template removal, while it is limited for further application due to the fact that the silica template can only be left out by the highly corrosive HF solution or the hot strong alkali aqueous solution. In contrast, polymer microspheres can be easily removed through calcination or extraction with an organic solvent and are more commonly used in the colloidal crystal templating method. The formation of colloidal template always undergoes a self-assembly process of colloidal microspheres in suspension. Such a self-assembly process of polymer microspheres is the most crucial step for the fabrication of 3DOM materials, and the arrangement of colloidal crystal templates directly determines the final degree of pore order and porosity structure of 3DOM materials. In order to control the self-assembly process of monodisperse colloidal microspheres to be converted into three-dimensionally ordered colloidal templates, several methods have been investigated, such as centrifugation, sedimentation, and electrophoresis. Centrifugation is considered to be the best method due to its low cost and flexible operation as well as the obtained highly ordered assembly colloidal crystal template.

A typical emulsion polymerization route of the colloidal crystal template can be illustrated by the PMMA-templating fabrication (Figure 1). Such a method involves several steps: The uniform dispersion of the precursor (methyl methacrylate, MMA) in a N<sub>2</sub> atmosphere at a given temperature in a water bath under stirring, the introduction of an inducer (K<sub>2</sub>S<sub>2</sub>O<sub>8</sub>), polymerization at above the glass transition temperature, centrifugation, washing for the removal of inorganic K<sup>+</sup> and SO<sub>4</sub><sup>2-</sup> ions, and gravity evaporation. After drying overnight at room temperature (RT), the as-synthesized PMMA microspheres are ready for use as a template. Gravity evaporation is a key step to ensure the ordering of PMMA microspheres. The PMMA microspheres obtained by drying emulsion with a specific concentration can be employed as colloidal template. Colloidal particles can self-assemble into a highly ordered three-dimensionally compact stacking structure through emulsion polymerization. The polymerization is well controlled and the sizes of microspheres are uniformly adjusted by controlling the reaction temperature and duration time. Higher temperature and longer reaction time will give rise to an excessive polymerization, thus resulting in larger particle sizes and possible aggregation of polymer microspheres. The initiator influences the surface charge on the polymer microspheres, which governs the interaction with the precursor. After polymerization, the polymer microspheres must be

cleaned many times with deionized water to protect the catalytic material from being polluted by the residual impurities using the microspheres as a template.

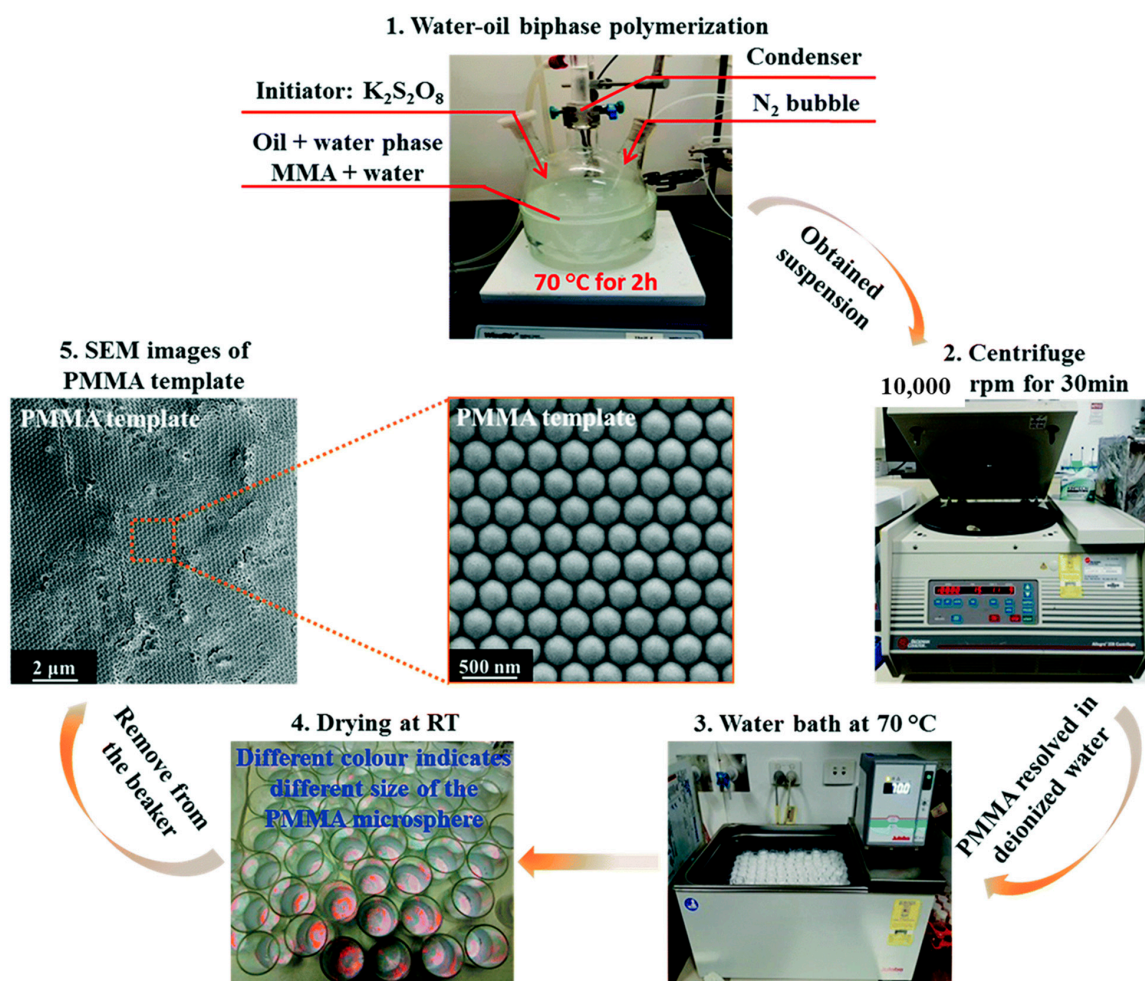


**Figure 1.** Equipment and process used to synthesize the PMMA microspheres template. Reprinted with permission from Ref. [35]. Copyright 2018, copyright Royal Society of Chemistry.

Mesoporous materials are mainly divided into silicon-based and nonsilicon-based samples. The synthesis mechanisms of mesoporous silica materials (such as liquid crystal template and synergistic effect mechanisms) and synthesis methods (such as hydrothermal and sol–gel methods) were studied. Nonsilicon mesoporous materials include mesoporous metal oxides/composites, mesoporous carbon, mesoporous metals, and mesoporous aluminum phosphate. The synthesis of nonsilicon mesoporous materials (especially mesoporous metal oxides) is more difficult than the silicon-based materials due to the diverse components, uncontrolled hydrolysis rates, and variable chemical valence states. The Pd/ $Al_2O_3$  catalyst with adjustable and uniform pore sizes was prepared via the sol–gel route by adjusting the template (deoxycholic acid and polyvinyl pyrrolidone acid) amounts. The as-obtained Pd/ $Al_2O_3$  catalyst with relatively large pore sizes (ca. 12 nm) exhibited an efficient and sustained catalytic methane combustion performance under a variety of operating conditions compared with the catalyst with small pore sizes (5–7 nm) [41]. Cobalt-doped ordered mesoporous alumina with intrinsic activity for methane combustion were synthesized using the sol–gel method with a P123 template. The as-obtained Pd–Co bimetallic catalyst exhibited a lower activation energy and a higher activity, which was attributed to the abundant active oxygen species for stabilizing the active PdO phase [42].

There are two kinds of templates for preparing mesoporous materials: soft template and hard template. The soft template method is to form the inorganic–organic composite

mesoporous structure through the molecular self-assembly of inorganic precursors and soft template agents, and the soft template is then removed to obtain the corresponding mesoporous materials. Soft template is a kind of surfactant; biomacromolecules or supramolecule (PEO-PPO-PEO, PE10300) with special structures are assembled into an ordered arrangement in dissolved solution, which plays a structure-oriented role in the fabrication of mesoporous materials. Amorphous mesoporous metal oxides are formed by the soft template method at lower temperatures, at which insufficient thermal treatment is offered to form crystalline materials, but they can be converted to crystalline oxides by calcination.

Ryoo's research group developed the technique of preparing ordered mesoporous materials via nanoreplication with ordered mesoporous silicon or carbon as hard template [43]. A typical synthesis of the KIT-6 template involves several steps: The uniform dispersion of the precursor (polyethylene oxide–polypropylene oxide–polyethylene, P123) in a water bath at 50 °C under stirring, the addition of an inducer (H<sub>2</sub>SO<sub>4</sub>, 1-butanol), polymerization (tetraethyl orthosilicate, TOES) under stirring at 35 °C, thermal treatment in a Teflon-lined autoclave at 100 °C for 24 h, filtration and drying, and calcination. The hard template method is used to successfully synthesize mesoporous materials by introducing the precursor solution into the channels of the hard template (SBA-15, KIT-6 or FDU-1) and calcination to form nanochannel crystal oxides. The big challenge of ordered mesoporous catalysts derived from the hard template route is determining how to completely fill the mesoporous channels of the hard template with the precursor solution so that the obtained target products possess regular pore structures and continued channels.

## 2.2. Macroporous or Mesoporous Composite Oxides

Generally speaking, the colloidal crystal template method is the most commonly employed to synthesize 3DOM materials (Figure 2). The precursor solution infiltrates sufficiently into the microsphere gaps for achieving the filling replication to obtain the regularly arranged large pore walls. The materials derived from such a route display a high degree of pore order and a well-controlled porosity that is a replica of the template. This method includes the following four steps: (i) Monodisperse PMMA microspheres are first synthesized by the emulsion-free polymerization, colloidal crystal templates are then obtained by the constant-temperature suspension method; (ii) according to the stoichiometry of each metal element in the target product, the product is configured into a homogeneous solution that dissolves the metal source, citric acid, and surfactant (e.g., triblock copolymer P123, F127, *L*-lysine, *L*-tryptophan, or xylitol); (iii) the PMMA hard template is impregnated in the precursor solution for a certain time and dried; and (iv) the sample is calcined in a tubular furnace under a N<sub>2</sub> atmosphere at low temperatures, in which the amorphous carbon formed due to partial carbonization of PMMA is served as a harder and heat-resistant template. Then, the above sample is further calcined in air at high temperatures to obtain the 3DOM material with a high surface area and a good pore structure. The precursor solution infiltrates the colloidal gap through the capillary action and must satisfy the following points: (i) The solution soaks the template fully without dissolving the template to avoid destroying ordered arrangement of the structure; (ii) the appropriate precursor solution concentration should be ensured to fabricate a three-dimensionally macroporous skeleton with good mechanical strength, but the liquid with a high concentration with a high density has difficulty infiltrating into the narrow channels; (iii) metal precursor solutions should be of mild reactivity to let the liquid enter the voids flexibly, and the metal precursors with strong reactivity may interact with the functional groups on the template surface or moisture in the air to avoid the infiltration of the precursor solutions; and (iv) the melting point of the dried metal oxide precursor must be higher than decomposition temperature of the template in air. It is relatively available to prepare the 3DOM metal oxide using metal alkoxide as precursor. However, metal salts (nitrates, acetates, and chlorides) are cheap and available compared with most of the metal alcohols, especially the low-valence transition metals and rare-earth metals. Yan et al. [44] synthesized a series of 3DOM transition-metal

oxides ( $\text{Fe}_2\text{O}_3$ ,  $\text{Cr}_2\text{O}_3$ ,  $\text{Mn}_2\text{O}_3$ , and  $\text{Co}_3\text{O}_4$ ) using the PMMA-template and impregnation methods with the transition-metal nitrate or acetate as precursor and ethanol or acetic acid as solvent. Precursor solution was deposited into the template gaps via the impregnation and evaporation routes. Since the melting point of nitrate or acetate is low, oxalate ions are introduced and react with the metal ions to form oxalates with higher melting points. The oxalates are decomposed directly to obtain 3DOM metal oxides, with the template being removed at high temperatures simultaneously. Sadakane et al. [45] prepared the 3DOM  $\text{Fe}_2\text{O}_3$ ,  $\text{Cr}_2\text{O}_3$ ,  $\text{Mn}_2\text{O}_3$ ,  $\text{Mn}_3\text{O}_4$ , and  $\text{Co}_3\text{O}_4$  using the PMMA-templating method with metal nitrates as precursors. Zhao and coworkers [46] carbonized the surface carboxyl-modified PMMA-templates in an inert atmosphere and calcined at 700 °C to generate the 3DOM  $\text{La}_{1-x}\text{K}_x\text{CoO}_3$  catalysts. Dai and coworkers [18,19] carried out a number of valuable works on this topic, and prepared various 3DOM-structured materials (e.g.,  $\text{Cr}_2\text{O}_3$ ,  $\text{Fe}_2\text{O}_3$ ,  $\text{Mn}_2\text{O}_3$ ,  $\text{Co}_3\text{O}_4$ ,  $\text{TiO}_2$ ,  $\text{CeO}_2$ ,  $\text{LaMnO}_3$ ,  $\text{LaSrCoO}_3$ , and  $\text{LaMnAl}_{11}\text{O}_{19}$ ) with high surface areas through the surfactant-aided PMMA-templating approaches. These authors claimed two kinds of the as-prepared macroporous walls with regular nano-bulk materials or accumulation of NPs. The macroporous walls which consisted of NPs accumulation displayed an irregular mesoporous structure and exhibited higher pore capacity than nano-bulk walls. The NPs accumulation walls showed high catalytic activity similar to the small-sized NPs. It is difficult to obtain porous crystalline structure of perovskite-type oxides via the colloidal crystals template route after they are calcined at high temperatures (above 1000 °C). However, our group successfully synthesized 3DOM  $\text{LaMnAl}_{11}\text{O}_{19}$  using a two-step calcination method via a PMMA-template route at 1100 °C [20]. The samples were first calcined in a  $\text{N}_2$  atmosphere at 400 °C to form a hard and heat-resistant partially carbonized framework to maintain a good pore structure. Then, the well-ordered pore hexaaluminate crystal phase was slowly formed after the high-temperature calcination at 1100 °C in an air atmosphere.

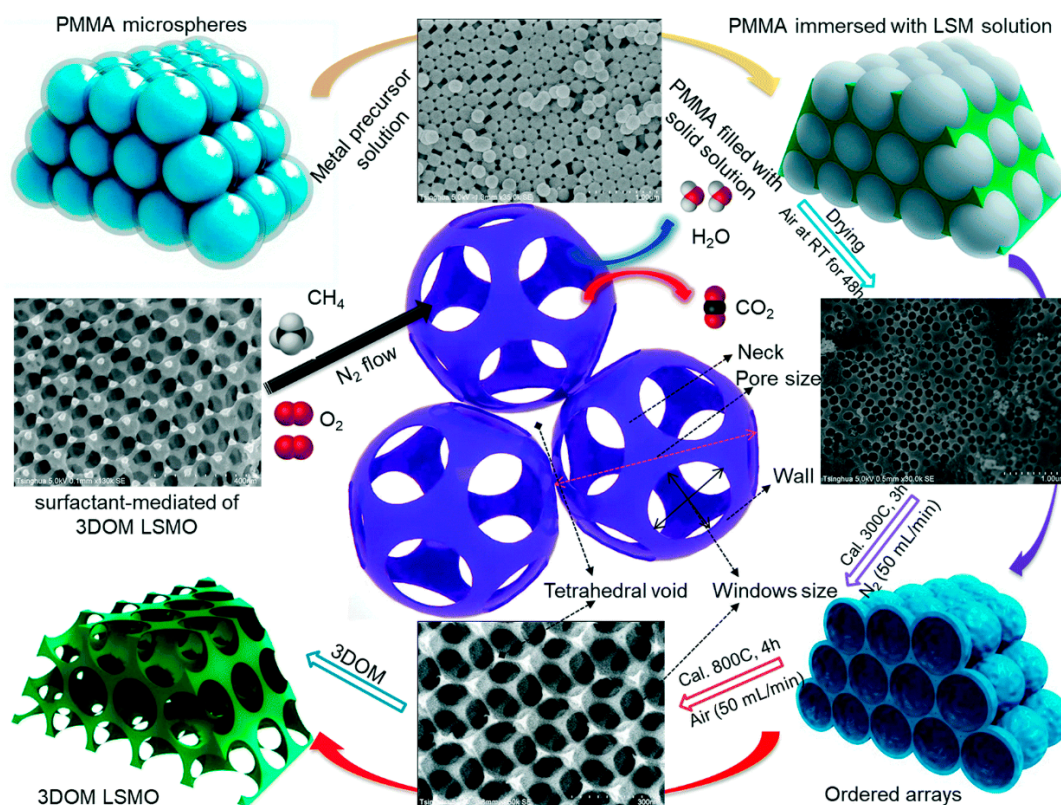


**Figure 2.** Preparation of rhombohedrally crystallized 3DOM LSMO catalysts using the PMMA-templating method. Reprinted with permission from Ref. [35]. Copyright 2018, copyright Royal Society of Chemistry.

The mesoporous structure was obtained by introducing metal salt solution into the pores of the hard template (KIT-6, SBA-15, or FUD-1) to achieve the solid-to-solid replication (i.e., so-called “nanocasting”). The big challenge in synthesizing ordered mesoporous catalysts via the hard template route is determining how to completely fill the mesoporous channels with metal precursors to ensure consistency and stability, so as to obtain the target products with well-ordered regular structures and continuous porous channels. The 3D ordered mesoporous (3DOMeso)  $\text{CrO}_x$  was prepared by the solvent-free and two-step calcination methods with KIT-6 as template [21]. Chromium nitrate was first melted in a sealed autoclave with a melting point of 60 °C and filled mesoporous channels of the KIT-6 template. The pressure in the autoclave increased with the decomposition of metal salts in the channel above 125 °C, which was beneficial for filling the channels of KIT-6 by the molten salts. The 3DOMeso  $\text{Fe}_2\text{O}_3$  [22] and 3DOMeso  $\text{Co}_3\text{O}_4$  [23] were fabricated by the vacuum-assisted nanocasting method with the alcohol solution of metal nitrate as the precursor source and KIT-6 or SBA-16 as the template. The hard-template powders were first treated under vacuum and airtight conditions, and then the metal nitrate alcohol solution of an appropriate concentration was added until no obvious superfluous solution was prospected. The 3DOMeso oxide was generated after the silicon template was removed with 10 vol% HF aqueous solution. The 3DOMeso  $\text{MnO}_2$  [24] was fabricated via an ultrasound-assisted SBA-16 template route with a high surface area of 266  $\text{m}^2/\text{g}$ . Ultrasonic treatment expelled the gas effectively and promoted the liquid–solid mass transfer and the metal precursors dispersion to maximize the filling of silicon channels, with the lowest possibility of forming oxides outside the silicon template. Well-ordered 3DOMesoporous frameworks are associated with the precursor solution concentration, since a diluted salt solution is too low to fully fill the template channel after drying.

### 2.3. Supported Metal Oxides or Noble Metals

High surface areas of ordered macro- or mesopores and increased surface oxygen species concentrations are beneficial for constructing bifunctional catalysts with high dispersion of the active phase(s) via supporting metal oxides or noble metals NPs. The particle sizes of noble metals mainly affect exposure of the active sites and utilization of the noble metals. Noble metal NPs exhibit good low-temperature catalytic activities, which is associated with their small particle sizes and good ability to flexibly activate reactant molecules. However, noble metal NPs can be agglomerated to big particles during the reaction process at high temperatures, thus resulting in poor thermal stability and irreversible catalyst deactivation. The coordinative environment of the noble metals is also the key factor influencing catalytic efficiencies of the supported noble metal catalysts, especially the oxidation states of noble metals and the strong interaction between the noble metal and the support. The strategies to regulate the coordinative environment of the noble metals mainly involve selection of the pretreatment atmosphere, modification of the noble metal NPs, and adjustment in physicochemical property of the support. Transition-metal oxides possess multiple metal oxidation states, and phase transition takes place after treatments at different temperatures. A suitable support is very important due to dispersing the active components of metals and increasing stability, selectivities, and activities of the supported noble metal catalysts. The well-developed catalysts with 3D porous structures favor adsorption and diffusion of the reactants and  $\text{O}_2$  molecules, and the large surface areas can efficiently disperse noble metal and/or metal oxide NPs to improve catalytic activities and thermal stability of the supported materials.

Ordered porous materials possess the advantages of stabilizing metal or metal oxide NPs, increasing surface active sites, and improving ultrahigh NPs dispersion [47] (Figure 3), as compared with micron-scale bulk samples. The traditional methods of loading metal NPs include the incipient wetness impregnation and adsorption. Dai and coworkers developed a novel strategy to generate a series of uniform-sized noble metals NPs supported on 3DOM-structured high-surface-area materials (e.g., Au–Pd–Co/3DOM  $\text{Mn}_2\text{O}_3$  [25], Au–Pd–CoO/3DOM  $\text{Co}_3\text{O}_4$  [26], CoPd/3DOM  $\text{CeO}_2$  [27], AuPd/3DOM

CoCr<sub>2</sub>O<sub>4</sub> [48], AuPd/3DOM La<sub>0.6</sub>Sr<sub>0.4</sub>MnO<sub>3</sub> [49], PdPt/3DOM LaMnAl<sub>11</sub>O<sub>19</sub> [20,50], and PdPt/MnO<sub>x</sub>/3DOM CoFe<sub>2</sub>O<sub>4</sub> [51]) by the PVA- or PVP-protected reduction and surfactant-assisted PMMA-templating approaches. For example, this group prepared the supported Au–Pd–M (M = Cr, Mn, Fe, and Co) catalysts by the acid-modified PVA-protected N<sub>2</sub>-bubbling reduction method [25,26]. The mixed solutions of PVA, HCl, chlorate, HAuCl<sub>4</sub>, and NaPdCl<sub>4</sub> after magnetic stirring were used as the noble metal precursor. The sodium borohydride was quickly introduced into the precursor solution as a reducing agent to prohibit the growth and agglomeration of Au–Pd–M NPs. The as-prepared 3DOM oxide was well-wetted via ultrasonic-assisted dispersion in a mixture solution with mild N<sub>2</sub> bubbling. After being washed with deionized water and ethanol before drying and calcination in furnace, the supported Au–Pd–M NPs possessed well-controlled particle sizes, ultrahigh dispersion, and stabilized metal NPs. Very recently, the same group developed a novel in situ noble-metal-embedded fabrication approach to synthesize Pt-embedded 3DOM Mn<sub>2</sub>O<sub>3</sub> via the PMMA-templating and ethylene glycol reduction routes [52]. The Pt-embedded 3DOM Mn<sub>2</sub>O<sub>3</sub> materials were fabricated by the one-step calcination method via the mixing of Pt-ethylene glycol solution and manganese nitrate precursor solution (which was dissolved in methanol). Part of the Pt NPs (with a size of 3.6–4.4 nm) were embedded in the skeleton of 3DOM Mn<sub>2</sub>O<sub>3</sub>, which exhibited an excellent thermal stability in the durative on-stream reaction, as compared with the sample derived from the gas-bubble-aided colloid adsorption route. On this basis, the same research group also successfully obtained the PtRu-embedded 3DOM Ce<sub>0.7</sub>Zr<sub>0.3</sub>O<sub>2</sub> catalysts with excellent thermal stability by adopting the PMMA-templating and ethylene-glycol-reduction approaches [53]. The embedded PtRu catalysts preserved changeless performance for toluene oxidation after thermal treatment at 800 °C, since the thermally treated sample showed a slight size increase of the average PtRu NPs from 4.2 to 6.7 nm, which was attributed to the embedded architecture to facilitate generation of a larger number of Pt–O–Ce-like bonds to stabilize the noble metals. However, the supported PtRu sample prepared by the colloidal adsorption method displayed a remarkable loss of PtRu surface area with an average enlarged PtRu size from 5.1 to 17.3 nm under the similar reaction conditions, resulting in a sharp decline in catalytic activity.

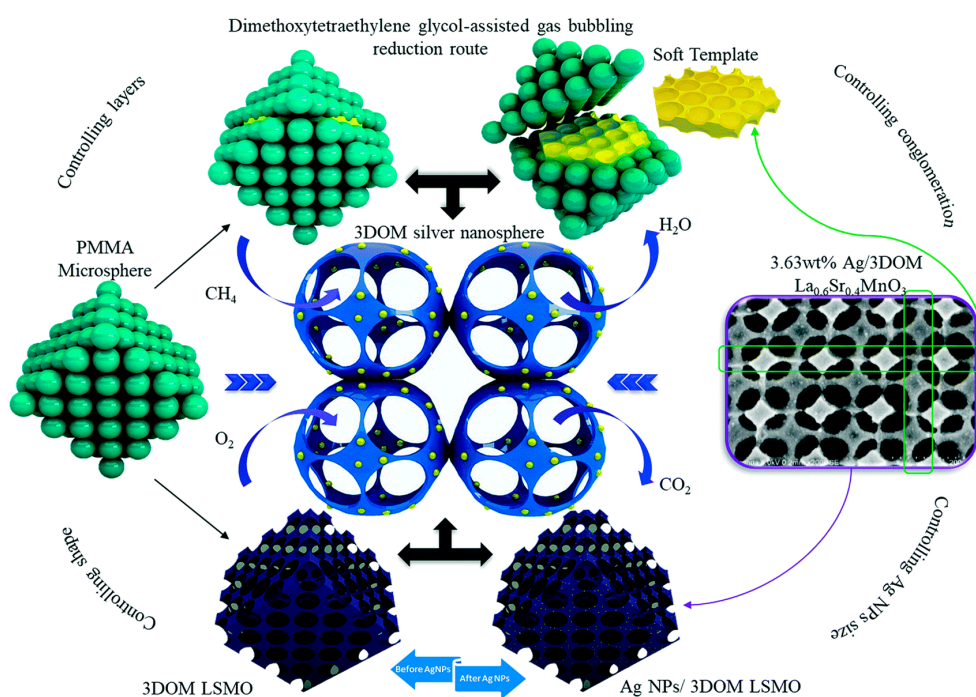


**Figure 3.** Schematic illustration of loading Ag NPs on 3DOM LSMO. Reprinted with permission from Ref. [47]. Copyright 2013, copyright Royal Society of Chemistry.

### 3. Applications for Methane Combustion

#### 3.1. Porous Composite Metal Oxides

Composite metal oxides exhibit an attractive potential in heterogeneous catalysis due to their suitable active components, appropriate structures, good surface electronic properties, and superior thermal stability. The multifunctional catalysts prepared by the specific chemical-tailoring methods (such as morphology construction or crystalline structure design) show high methane catalytic combustion performance [27,28,54]. Activity of a multifunctional catalyst can be improved by enlarged surface area and ordered pore structure; after all, the reaction rate is often proportional to surface area. The pore structure of a catalyst facilitates mass transfer of CH<sub>4</sub> in the reaction system and reduces the mass transfer resistance of CH<sub>4</sub> and O<sub>2</sub>, further facilitating a better contact with the surface active centers. Meanwhile, the developed and well-interconnected 3D pore structure is beneficial for the adsorption and diffusion of CH<sub>4</sub> and O<sub>2</sub> molecules, making a significant contribution to high catalytic efficiency. Wu et al. [28] prepared 3D ordered mesopore-structured cubic Co<sub>3</sub>O<sub>4</sub> (meso-Co<sub>3</sub>O<sub>4</sub>) using the KIT-6-templating approach with a high surface area of 106 m<sup>2</sup>/g and a crystallite size of 14.4 nm (Figure 4). The meso-Co<sub>3</sub>O<sub>4</sub> sample showed a high CH<sub>4</sub> combustion activity, with the  $T_{10\%}$ ,  $T_{50\%}$ , and  $T_{90\%}$  being 293, 345, and 440 °C at a SV of 20,000 mL/(g h), respectively, and the apparent activation energy ( $E_a$ ) being 81.9 kJ/mol. Xie et al. [27] generated the 3DOM CeO<sub>2</sub> catalyst with a macropore diameter of 155–165 nm and a surface area of 41.2 m<sup>2</sup>/g via the PMMA-templating route. The 3DOM CeO<sub>2</sub> sample showed high catalytic performance ( $T_{50\%} = 599$  °C at a SV of 40,000 mL/(g h)) and an  $E_a$  of 112 kJ/mol, as well as excellent (hydro)thermal stability in methane oxidation.

Acidity and basicity are mainly discussed in zeolite supports, and the positive effect of acidic sites is to anchor the active PdO component. Migration of PdO NPs on external surface of the zeolitic support and formation of larger PdO NPs during the hydrothermal treatment process may also contribute to the catalyst deactivation. The presence of the Brønsted acid sites in zeolite may facilitate the ion exchange of Pd and stabilize the dispersed PdO NPs; however, the presence of the Brønsted acid sites in the catalyst would eventually result in poor stability of the catalyst under the reaction conditions due to conversion of the PdO NPs into the Pd cations through “protonolysis” at the acid sites [55].

The addition of alkali metal ions could significantly improve the activity and onstream stability of aluminosilicates or siliceous zeolitic catalysts with a relatively low Si/Al ratio (<100) [56]. The promotion effect of Na<sup>+</sup> was confirmed to significantly enhance stability of the catalyst in the wet feedstock, especially in the step after Pd was already deposited on the zeolitic support [57]. The incorporation of Co<sup>2+</sup> ions into Pd/BEA (Si/Al = 13) promoted the formation of PdO NPs, thus significantly improving methane combustion performance [58].

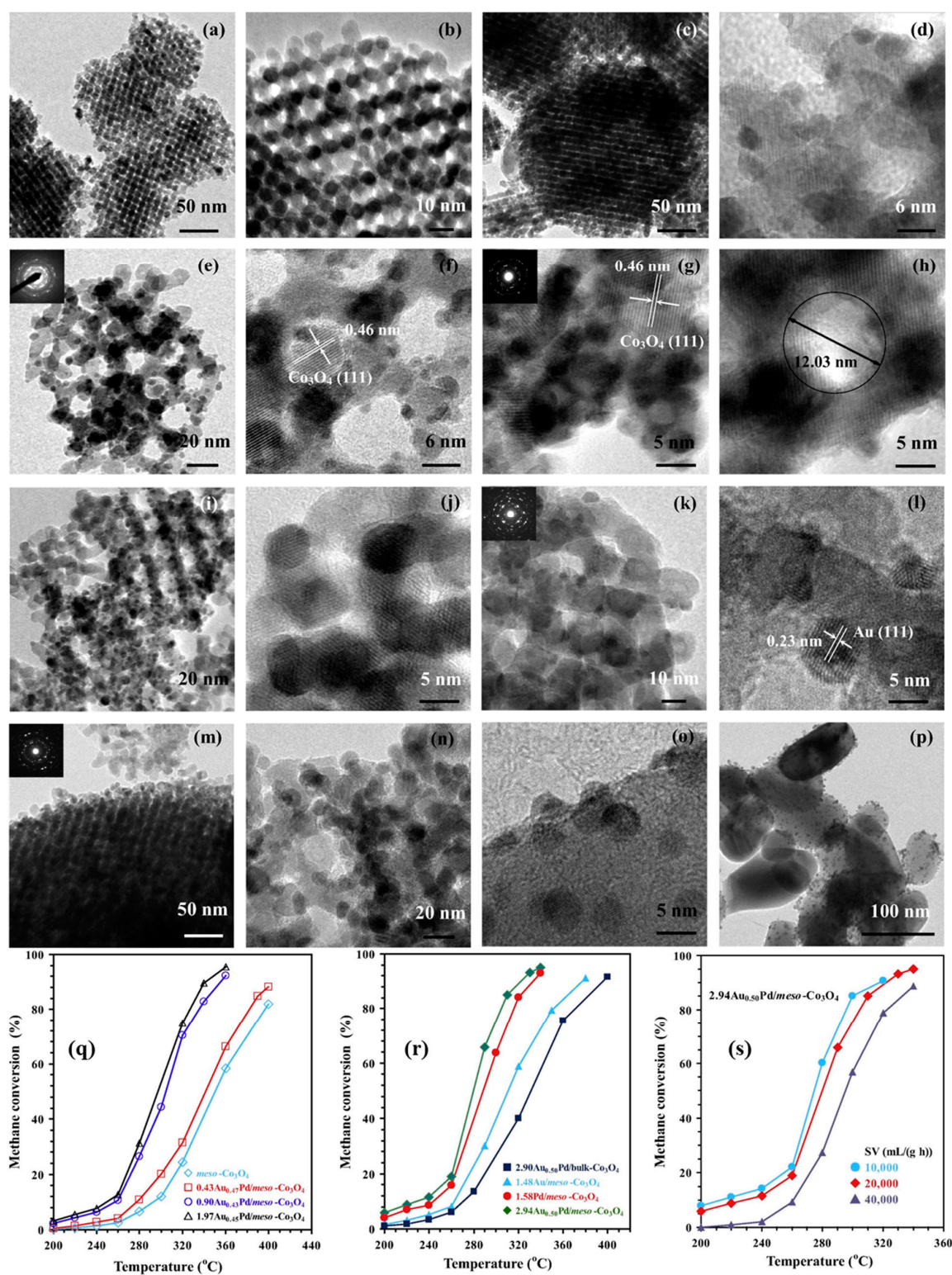


**Figure 4.** TEM images and SAED patterns (insets) of (a,b) meso- $\text{Co}_3\text{O}_4$ , (c,d)  $0.43\text{Au}_{0.47}\text{Pd}/\text{meso-}\text{Co}_3\text{O}_4$ , (e,f)  $0.90\text{Au}_{0.43}\text{Pd}/\text{meso-}\text{Co}_3\text{O}_4$ , (g,h)  $1.97\text{Au}_{0.45}\text{Pd}/\text{meso-}\text{Co}_3\text{O}_4$ , (i,j)  $2.94\text{Au}_{0.50}\text{Pd}/\text{meso-}\text{Co}_3\text{O}_4$ , and (k,l)  $1.48\text{Au}/\text{meso-}\text{Co}_3\text{O}_4$ , (m,n)  $1.58\text{Pd}/\text{meso-}\text{Co}_3\text{O}_4$ , and (o,p)  $2.90\text{Au}_{0.50}\text{Pd}/\text{bulk-}\text{Co}_3\text{O}_4$ ; (q,r) methane conversion as a function of reaction temperature over the as-prepared samples at SV = 20,000 mL/(g h); and (s) effect of SV on methane oxidation over the  $2.94\text{Au}_{0.50}\text{Pd}/\text{meso-}\text{Co}_3\text{O}_4$  sample. Reprinted with permission from Ref. [28]. Copyright 2015, copyright Elsevier Ltd.

Mixed-metal oxides, such as  $ABO_3$ ,  $A_2BO_4$ , and  $A_2B_2O_x$ , show better catalytic performance than their single-metal counterparts for the complete oxidation of organics. It was found that lattice defects (i.e., catalytically active sites) in the crystal structure favor the deep oxidation of reactants. For example,  $ABO_3$  is a typical compound where both A and B cation sites can be isomorphically substituted by heterovalent ions, in which the A-site cations are usually rare-earth or alkaline-earth ions, while the B-site cations are transition-metal ions. The complete or partial substitution of the two cationic sites induces changes in oxygen vacancy (defect) concentration and adjusts oxidation states of the transition-metal ions, thus modifying physicochemical property of an  $ABO_3$ . If oxygen molecules can be readily activated into various oxygen species, oxidation and reduction processes of a catalyst are easy to realize. Due to abundant oxygen vacancies and coexisting of B-site transition-metal ions in various oxidation states of mixed-metal oxides,  $O_2$  can be easily activated into various active oxygen species. Therefore, mixed-metal oxides are one kind of excellent complete oxidation catalysts that exhibit high activities for  $CH_4$  combustion. For example, Wang et al. [48] prepared 3DOM-structured cubic  $CoCr_2O_4$  using a PMMA-templating method with a high-quality 3DOM architecture and a surface area of 33–36  $m^2/g$ . For methane combustion, the 3DOM  $CoCr_2O_4$  sample performed excellently ( $T_{50\%} = 370$  °C and  $T_{90\%} = 440$  °C at  $SV = 20,000$  mL/(g h)), and its activity was much better than that over the bulk  $CoCr_2O_4$  catalyst ( $T_{50\%} = 400$  °C and  $T_{90\%} = 490$  °C at  $SV = 20,000$  mL/(g h)). The turnover frequency (TOF =  $0.168 \times 10^{-3}$   $s^{-1}$ ) of 3DOM  $CoCr_2O_4$  was much higher than that ( $0.0936 \times 10^{-3}$   $s^{-1}$ ) of bulk  $CoCr_2O_4$ . The authors claimed that the superior methane oxidation activity of 3DOM  $CoCr_2O_4$  was associated with its larger surface area, higher  $O_{ads}$  species concentration, better low-temperature reducibility, and unique nanovoid-containing 3DOM structure. After investigating methane combustion over the cubically-crystallized 3DOM  $MnCo_2O_4$  catalyst derived from the PMMA-templating route, Han et al. [59] found that 3DOM  $MnCo_2O_4$  possessed a high-quality 3DOM architecture and a high catalytic activity:  $T_{50\%}$  and  $T_{90\%}$  were 435 and 524 °C at  $SV = 40,000$  mL/(g h), respectively. The authors concluded that the enhanced surface area, high  $O_{ads}$  species concentration, and unique pore structure were accountable for the good catalytic performance of 3DOM  $MnCo_2O_4$  for methane combustion. Li et al. [51] prepared 3DOM  $CoFe_2O_4$  using the PMMA-templating and incipient wetness impregnation strategies, and observed that the as-prepared samples exhibited a high-quality 3DOM structure (103 ± 20 nm in pore size) and a surface area of 19–28  $m^2/g$ , which performed well ( $T_{50\%} = 500$  °C and  $T_{90\%} = 598$  °C at  $SV = 20,000$  mL/(g h)) for methane combustion.

Rare-earths (REs) are widely used as dopants to modify physicochemical properties of the perovskite-type oxide materials due to their various multivalent ions and electron configurations. The variable valence states and unique electronic structures render RE ions to be of flexible redox properties, and functional perovskite-type oxide materials exhibit satisfactory methane oxidation activities by incorporating RE ions into the perovskite nanostructures. Chen et al. [60] fabricated a series of 3D porous perovskite-type oxides ( $LaCoO_3$ ,  $LaMnO_3$ ,  $LaFeO_3$ ,  $La_{0.8}Sr_{0.2}CoO_3$ , and  $La_{0.9}Ce_{0.1}CoO_3$ ) nanofibers with partial substitution of La by Sr or Ce through an electrospinning route. The above perovskite-type oxide nanofiber samples exhibited the  $T_{90\%}$  values of 510, 520, 540, 470, and 490 °C at  $SV = 104,000$  mL/(g h), respectively. The interconnected nanofibers formed a 3D porous architecture with high porosity, a surface area of 40–60  $m^2/g$ , and a pore diameter of 100–200 nm. The authors believed that large surface areas and 3D porous architectures were accountable for the remarkable methane combustion activity. Arandiyani et al. prepared the 3D highly ordered macro- or mesoporous multifunctional  $La_{1-x}Ce_xCoO_3$  nanohybrid frameworks (Figures 5 and 6) with surface areas of 16.5–35.4  $m^2/g$  via the facile meso-molding route in a 3D macroporous perovskite-type oxide (MTMP) [61].

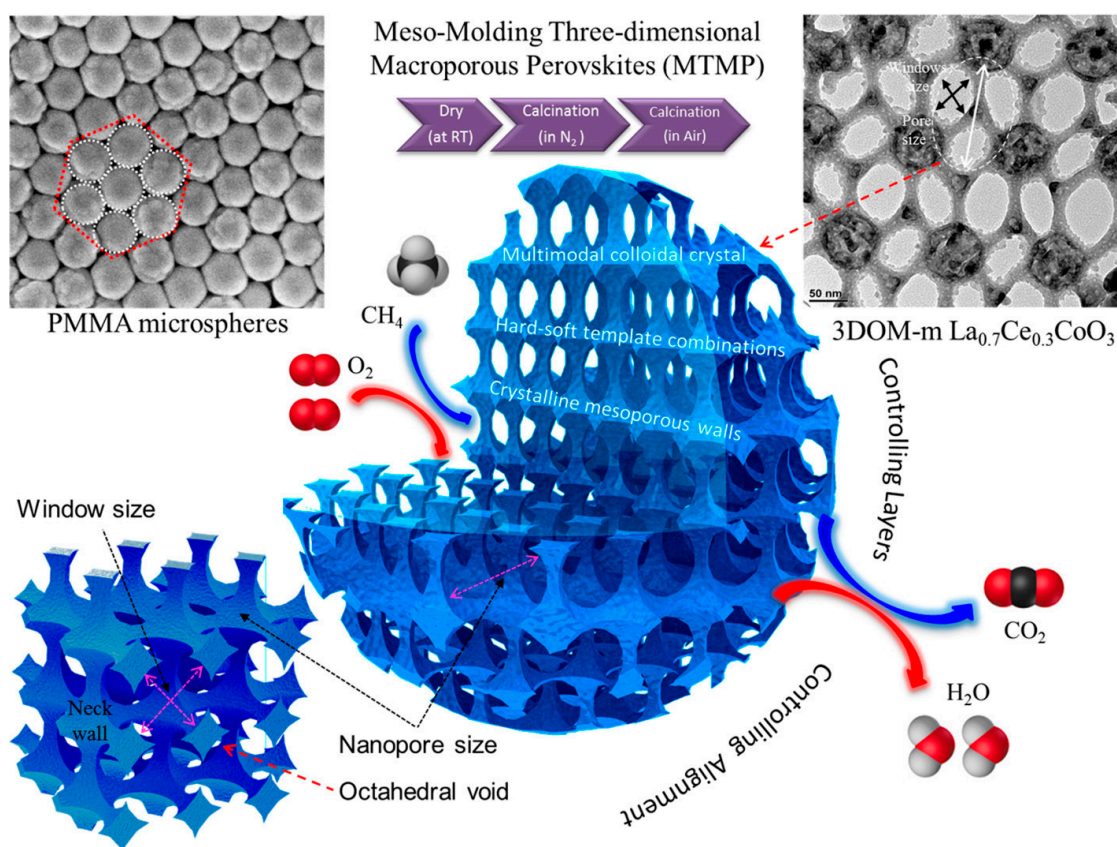


**Figure 5.** Schematic illustration of the 3DOM-m  $\text{La}_{1-x}\text{Ce}_x\text{CoO}_3$  catalysts. Reprinted with permission from Ref. [60]. Copyright 2015, copyright American Chemical Society.

More available macropores (205–195 nm in diameter) were synthesized to reduce diffusion restrictions, thus preserving the relatively short diffusion pathways on the mesopore walls (10.2–11.9 nm in diameter). It is worth noting that the 3DOM  $\text{La}_{0.7}\text{Ce}_{0.3}\text{CoO}_3$  sample showed a higher methane oxidation activity ( $T_{50\%} = 479\text{ }^\circ\text{C}$  and  $T_{90\%} = 555\text{ }^\circ\text{C}$  at  $\text{SV} = 30,000\text{ mL}/(\text{g h})$ ) with a lower  $E_a$  of 53 kJ/mol. The incorporation of Ce was attributed to the improved thermal stability, and the higher oxygen vacancy density facilitated the adsorption and activation of  $\text{O}_2$ . The authors found that the superior methane combustion activity was due to its larger surface area, better low-temperature reducibility, higher  $\text{O}_{\text{ads}}$  species concentration, higher surface-to-volume ratio, and unique nanovoid-like 3DOM-mesoporous structure. The 3D ordered macroporous orthorhombically crystallized perovskite-like oxide  $\text{La}_2\text{CuO}_4$  with a surface area of up to  $46\text{ m}^2/\text{g}$  and a pore size range of 68–136 nm was synthesized using the PMMA-templating strategy [62]. The 3DOM-structured  $\text{La}_2\text{CuO}_4$  material performed well in methane oxidation with a  $T_{90\%}$  value of  $672\text{ }^\circ\text{C}$  and a  $\text{CH}_4$  reaction rate of ca.  $40\text{ mmol}/(\text{g h})$  at  $\text{SV} = 50,000\text{ mL}/(\text{g h})$ . The authors concluded that the higher surface area, better reducibility, and 3DOM architecture were the desirable features for high catalytic performance. Wang et al. [6] generated an ordered mesoporous  $\text{LaCoO}_3$  perovskite via the nanocasting route using ordered mesoporous vinyl silica template and investigated its catalytic activity for the complete oxidation of methane. The hierarchical cellular architecture sample displayed a high surface area of  $96.7\text{ m}^2/\text{g}$  and an average pore size of 6.7 nm. This mesoporous  $\text{LaCoO}_3$  perovskite exhibited superior physiochemical properties (e.g., a high surface area with 3D ordered mesoporous channels, high valent cobalt ions, and high  $\text{O}_2^{2-}/\text{O}^-$  species content), thus showing a much higher activity in methane combustion ( $T_{50\%} = 470\text{ }^\circ\text{C}$  and  $T_{90\%} = 600\text{ }^\circ\text{C}$  at  $\text{SV} = 60,000\text{ mL}/(\text{g h})$ ), as compared with the conventional bulk  $\text{LaCoO}_3$  perovskite ( $T_{50\%} = 595\text{ }^\circ\text{C}$  and  $T_{90\%} = 670\text{ }^\circ\text{C}$  under the same conditions). Gao et al. [63] developed a facile novel route to generate mesopore zirconia nanobelts with high surface areas and

well-distributed mesopores (3.4–3.6 nm in pore diameter) for methane combustion. The meso-Zr<sub>0.8</sub>Fe<sub>0.2</sub>O<sub>2</sub> sample showed a good methane oxidation activity ( $T_{50\%} = 650\text{ }^{\circ}\text{C}$  and  $T_{90\%} = 750\text{ }^{\circ}\text{C}$  at  $\text{SV} = 25,000\text{ mL}/(\text{g h})$ ) with an  $E_a$  of 135 kJ/mol. Zhang et al. [64] adopted the cetyltrimethyl ammonium bromide (CTAB)-aided hydrothermal strategy to prepare the nanosized mesoporous polycrystalline Ce<sub>0.6</sub>Zr<sub>0.3</sub>Y<sub>0.1</sub>O<sub>2</sub> (CZY) material with a high surface area of 90 m<sup>2</sup>/g and an average pore diameter of 4.4 nm. At  $\text{SV} = 50,000\text{ mL}/(\text{g h})$ , the  $T_{50\%}$  and  $T_{90\%}$  values for methane oxidation were 840 and 870 °C, respectively. Hexaaluminates (AAl<sub>12</sub>O<sub>19</sub>: A is an alkali, alkaline-earth, or rare-earth metal ion) possess a  $\beta$ -Al<sub>2</sub>O<sub>3</sub> structure and high surface areas (>20 m<sup>2</sup>/g even after calcination at temperatures above 1200 °C). Thus, AAl<sub>12</sub>O<sub>19</sub> materials after partial substitution of Al ions by transition metal (e.g., Cr, Mn, Fe, Co, Ni, or Cu) ions were regarded as excellent candidate catalysts for methane combustion. For example, Xu et al. [50] prepared the good-quality 3DOM structure LaMnAl<sub>11</sub>O<sub>19</sub> catalyst with an average macropore size of 116 nm and a surface area of 27.2 m<sup>2</sup>/g using a PMMA-templating method. The  $T_{10\%}$ ,  $T_{50\%}$ , and  $T_{90\%}$  values over 3DOM LaMnAl<sub>11</sub>O<sub>19</sub> were 426, 535, and 625 °C, which were much lower than those (478, 602, and 720 °C) over bulk LaMnAl<sub>11</sub>O<sub>19</sub>, respectively. The enhanced catalytic activity was owing to the well-prepared porous structure and large surface area, resulting in the shortening of contact time between the catalyst and the reactants.

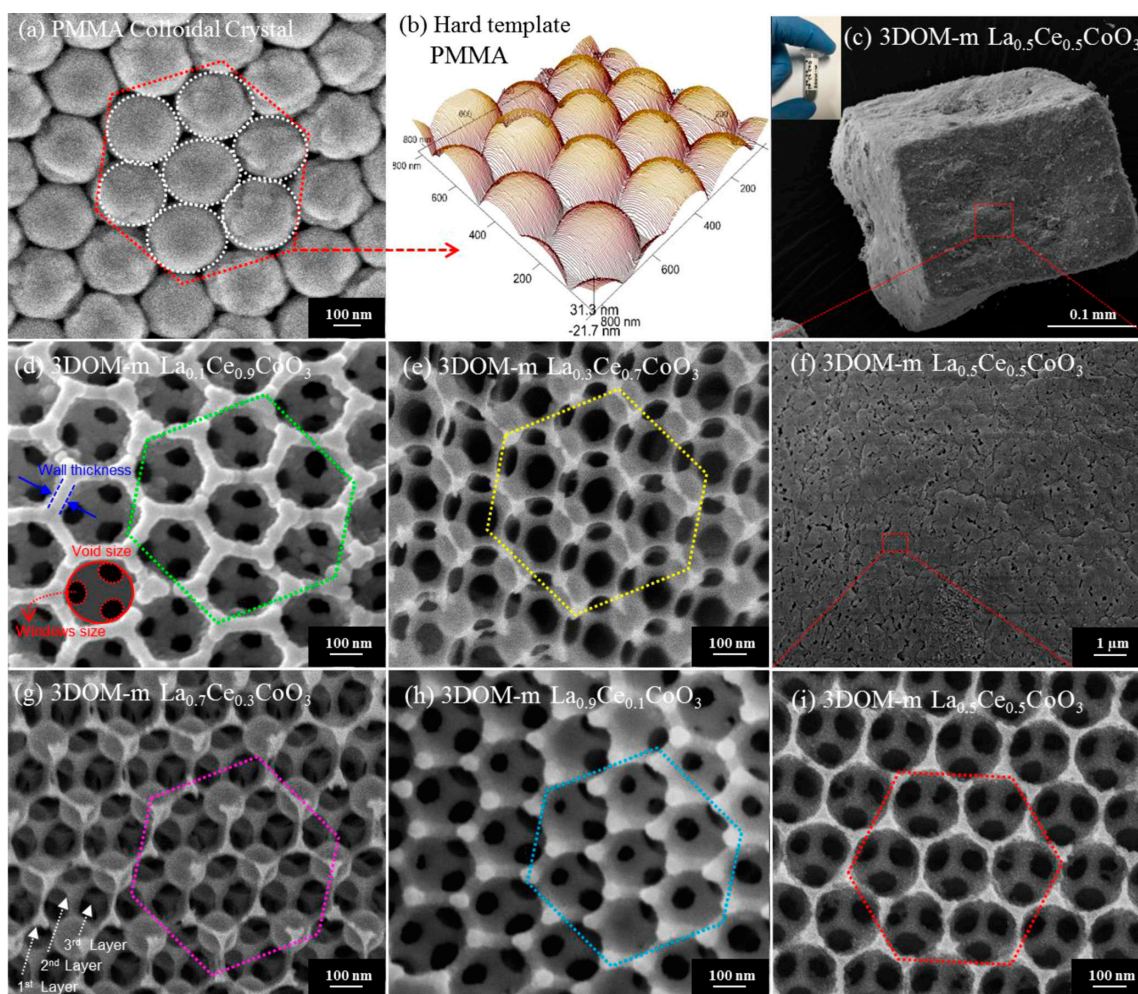


**Figure 6.** FE-HRSEM and 3D-eAFM images of (a,b) the PMMA and 3DOM-m La<sub>1-x</sub>Ce<sub>x</sub>CoO<sub>3</sub> catalysts where  $x =$  (c,f,i) 0.5, (d) 0.9, (e) 0.7, (g) 0.3, and (h) 0.1. Reprinted with permission from Ref. [60]. Copyright 2015, copyright American Chemical Society.

Perovskite-type oxides have broad prospects of fabricating multifunctional materials via partial substitution of cations with noble metals. Such heterogeneous catalysts with incorporation of highly dispersed noble metals to the lattice in the crystal structure show superior methane combustion activities. Adopting the PMMA-template and in situ reduction methods, Zhao et al. [65] obtained the rhombohedral 3DOM-structured  $\text{La}_{0.6}\text{Sr}_{0.4}\text{MnO}_3$  and  $\text{La}_{0.6}\text{Sr}_{0.4}\text{Mn}_{0.96}\text{Pd}_{0.04}\text{O}_3$  catalysts with Pd being incorporated to the perovskite lattice, and investigated their catalytic activities for methane combustion. The as-obtained heterogeneous catalyst displayed a good 3DOM structure with uniform close-packed periodic voids (180–190 nm in average pore size) and a surface area of  $24.5 \text{ m}^2/\text{g}$ . The sample with a 1.18 wt% Pd content performed well, and methane conversion temperature followed the order of 3DOM  $\text{La}_{0.6}\text{Sr}_{0.4}\text{Mn}_{0.96}\text{Pd}_{0.04}\text{O}_3 > 3\text{DOM } \text{La}_{0.6}\text{Sr}_{0.4}\text{MnO}_3$ , with the  $T_{50\%}$  and  $T_{90\%}$  values being 458 and  $550 \text{ }^\circ\text{C}$  at  $\text{SV} = 40,000 \text{ mL}/(\text{g h})$ , respectively. The in situ reduction of the Pd-containing samples was beneficial for the excellent catalytic performance, resulting in good thermal stability, strong  $\text{SO}_2$ -tolerant ability, and strong interaction between Pd and substrate. Guo et al. [66] reported the successful fabrication of 3DOM  $\text{LaMnPdO}_3$  with a large surface area of  $31.7 \text{ m}^2/\text{g}$  using the PMMA-templating and self-regeneration methods. High lattice parameters were obtained after the doping of Pd, since  $\text{Pd}^{2+}$  (0.086 nm) is larger than high-spin  $\text{Mn}^{3+}$  (0.064 nm) and high-spin  $\text{Mn}^{2+}$  (0.067 nm). This result indicated that Pd infiltrated into the crystal lattice of  $\text{LaMnO}_3$ . The catalytic oxidation of methane over 3DOM  $\text{LaMn}_{0.97}\text{Pd}_{0.03}\text{O}_3$  displayed the highest activity ( $T_{50\%} = 412 \text{ }^\circ\text{C}$  and  $T_{90\%} = 504 \text{ }^\circ\text{C}$  at  $\text{SV} = 32,000 \text{ mL}/(\text{g h})$ ) and the lowest apparent activation energy of  $51.5 \text{ kJ}/\text{mol}$ , and furthermore the specific reaction rate ( $10.9 \times 10^{-2} \text{ mmol}_{\text{CH}_4}/(\text{g}_{\text{Pd}} \text{ s})$ ) was much higher than that reported in the literature. The authors thought that the excellent performance of such a catalyst was associated with its ordered porous structure, rich  $\text{O}_{\text{ads}}$  species, large surface area, and strong metal–support interaction between the segregated Pd and  $\text{LaMnO}_3$ .

Table 1 gives an activity overview of the various porous catalysts for methane oxidation reported in the literature. It can be realized from the above investigations that the macro- mesoporous composite metal oxides (including transition-metal oxides, perovskite-type oxides, and hexaaluminates) with large surface areas and high-quality pore structures exhibited high performance for methane combustion. Such specifically morphological composite metal oxides showed good catalytic performance for the combustion of  $\text{CH}_4$ , which was associated with the unique well-ordered 3D pore structure, good thermal stability, high surface area, good low-temperature reducibility, abundant oxygen vacancies, and high  $\text{O}_{\text{ads}}$  species concentration.

**Table 1.** Catalytic performance for  $\text{CH}_4$  combustion over the ordered porous composite oxide catalysts.

Catalyst	Template	Pore Diameter (nm)	BET Surface Area ( $\text{m}^2/\text{g}$ )	$\text{CH}_4$ Concentration (vol%)	SV ( $\text{mL}/(\text{g h})$ )	$T_{50\%}$ ( $^\circ\text{C}$ )	$T_{90\%}$ ( $^\circ\text{C}$ )	Ref.
meso- $\text{Co}_3\text{O}_4$	KIT-6	14.4	106.3	2.5	20,000	345	440	[28]
meso- $\text{Mn}_2\text{O}_3$	KIT-6	11.0	104.8	2.5	20,000	486	>500	[54]
3DOM $\text{CeO}_2$	PMMA	155–165	41.2	2.5	40,000	599	>600	[27]
3DOM $\text{CoFe}_2\text{O}_4$	PMMA	83–123	20.0	2.5	20,000	500	598	[51]
3DOM $\text{CoCr}_2\text{O}_4$	PMMA	120–180	33.2	2.5	20,000	370	440	[48]
3DOM $\text{MnCo}_2\text{O}_4$	PMMA	180–200	26.5	2.5	40,000	435	524	[59]
$\text{LaMnO}_3$ nanofibers	PVP	100–200	55.2	0.2	104,000	450	520	[61]
$\text{LaFeO}_3$ nanofibers	PVP	100–200	40.1	0.2	104,000	470	540	[61]
$\text{LaCoO}_3$ nanofibers	PVP	100–200	57.3	0.2	104,000	472	510	[61]
$\text{La}_{0.8}\text{Sr}_{0.2}\text{CoO}_3$ nanofibers	PVP	100–200	63.6	0.2	104,000	400	470	[61]
$\text{La}_{0.9}\text{Ce}_{0.1}\text{CoO}_3$ nanofibers	PVP	100–200	60.8	0.2	104,000	415	490	[61]
3DOM $\text{LaCeCoO}_3$	MTMP	195–205	31.5	2.0	30,000	479	555	[60]
3DOM $\text{La}_2\text{CuO}_4$	PMMA	68–136	46	2.0	50,000	560	672	[62]
Meso- $\text{LaCoO}_3$	Vinyl silica	6.7	96.7	0.8	60,000	470	600	[6]
3DOM $\text{LaMnPdO}_3$	PMMA	$180 \pm 10$	31	1.0	32,000	412	504	[66]
Meso- $\text{Zr}_{0.8}\text{Fe}_{0.2}\text{O}_2$	P-123	3.4–3.6	51.2	1.99	25,000	650	750	[63]
3DOM $\text{La}_{0.6}\text{Sr}_{0.4}\text{MnO}_3$	PMMA	180–195	24.3	2.5	40,000	479	592	[65]
3DOM $\text{La}_{0.6}\text{Sr}_{0.4}\text{MnO}_3$	PMMA	140–153	32.4	5.0	50,000	384	508	[49]
3DOM $\text{La}_{0.6}\text{Sr}_{0.4}\text{MnPd}_{0.04}\text{O}_3$	PMMA	180–190	24.2	2.5	40,000	458	550	[65]
3DOM $\text{LaMnAl}_{11}\text{O}_{19}$	PMMA	116	27.2	2.5	20,000	535	625	[50]
Meso- $\text{Ce}_{0.6}\text{Zr}_{0.3}\text{Y}_{0.1}\text{O}_2$	CTAB	4.4	90	2.5	50,000	840	870	[64]

### 3.2. Supported Metal Oxide Catalysts

Transition-metal (e.g., Mn, Co, Cr, Ni, Fe, V, and Cu) oxides are considered to be practical and versatile catalysts for methane combustion and possess high catalytic activities owing to their multiple oxidation states, lattice defects (i.e., oxygen vacancies), strong oxygen mobility, easy desorption and activation of reactant molecules, and improved thermal stability. The low cost and facile synthesis of transition-metal oxide catalysts make them a prominent research topic, and much attention has been paid to the oxide structures accountable for the good performance. The cation states (e.g.,  $\text{Co}^{3+}/\text{Co}^{2+}$ ,  $\text{Sn}^{4+}/\text{Sn}^{2+}$ ,  $\text{Fe}^{2+}/\text{Fe}^{3+}$ ,  $\text{Cu}^{2+}/\text{Cu}^+/\text{Cu}^0$ , and  $\text{Mn}^{4+}/\text{Mn}^{3+}/\text{Mn}^{2+}$ ) in the crystal structures are the most likely active sites for adsorption and activation of reactants and  $\text{O}_2$  as well as for the high catalytic performance. For instance, a high-throughput investigation carried out by Saalfrank and Maier in 2004 substantiated the good performance of the noble-metal-free catalysts for CO oxidation [67].

The transition metal (e.g., Cu, Fe, Co, Ni, Mn, and Ce) oxides with typical multiple valence states help to form redox cycles of the catalytic process between the high and low oxidation states, thereby restoring and releasing the lattice oxygen species. Phase transition of the active components may affect thermal stability and catalytic performance of the catalyst [68].  $\text{Co}_3\text{O}_4$  has the weakest metal–oxygen bond, and the easy reduction of  $\text{Co}^{3+}$  in  $\text{Co}_3\text{O}_4$  to  $\text{Co}^{2+}$  could accelerate formation of the oxygen vacancies at low temperatures [69].  $\text{CeO}_2$  is one of the most effective metal oxides due to its excellent redox property and oxygen storage ability [70]. However, the high-temperature redox cycle presents a remarkable challenge for structure and reactivity of the catalyst and limits the oxygen-carrying capacity of pure  $\text{CeO}_2$ .  $\text{MnO}_x$  has flexible valence states (i.e.,  $\text{Mn}^{2+}$ ,  $\text{Mn}^{3+}$ , and  $\text{Mn}^{4+}$ ), among which the nanocubic  $\text{MnO}_2$  sample exhibited the best low-temperature reducibility [71].  $\text{ZrO}_2$  as an excellent stabilizer can effectively overcome the sintering challenge caused by a sharp decrease of surface area in the high-temperature redox cycle [72]. However, thermal stability of the unmodified active NiO catalysts was poor, which could be combined with other metals for the utilization of catalytic lean methane combustion [73]. For methane combustion in the presence of sulfur dioxide, metal oxide catalysts can form sulfates at a high temperature (e.g., 550 °C), which gives rise to an irreversible deactivation of the catalysts.

Most of the transition metals exhibit a virtually constant heat of adsorption in a large range of oxygen coverage; however, the chemisorption heat produced on noble metals (Rh, Pd, and Pt) decreases continuously with the rise in oxygen coverage [74]. Cobalt oxides are one of the most widely investigated transition-metal oxides.  $\text{Co}_3\text{O}_4$  is the most stable oxide in the range of 350–900 °C, and shows the best catalytic activity due to its two valence states ( $\text{Co}^{3+}$  and  $\text{Co}^{2+}$ ). Above 900 °C,  $\text{Co}_3\text{O}_4$  loses oxygen spontaneously to form CoO.  $\text{Co}_3\text{O}_4$  displays an ideal spinel-type structure, in which one-eighth of the tetrahedral sites is occupied by  $\text{Co}^{2+}$  ions, whereas half of the octahedral sites is occupied by  $\text{Co}^{3+}$  ions. The copresence of  $\text{Co}^{3+}$  and  $\text{Co}^{2+}$  pairs in the same catalysts seems to be critical for the good performance. The  $\text{Co}_3\text{O}_4/\text{CeO}_2$  catalyst was used to study methane combustion under the reaction conditions of (1.0 vol%  $\text{CH}_4$  + 4.0 vol%  $\text{O}_2$  + Ar (balance) and  $\text{SV} = 30,000 \text{ mL}/(\text{g h})$ ) [75]. The best  $\text{CH}_4$  oxidation activity ( $T_{50\%} = 401 \text{ °C}$  and  $T_{90\%} = 490 \text{ °C}$ ) was achieved over the sample with a  $\text{Co}/(\text{Co} + \text{Ce})$  atomic ratio of 0.75, which was due to the enhanced oxygen vacancy concentration, good reducibility, and strong mutual interaction between Ce and Co. The supported three-component (12 wt%  $\text{Co}_3\text{O}_4$  + 3 wt%  $\text{Fe}_2\text{O}_3$  + 3 wt%  $\text{MnO}_2$ ) monolithic catalysts on a mixture of modified Ce–Zr–O solid solution and YSZ– $\text{Al}_2\text{O}_3$  showed a superior performance ( $T_{50\%} = 358 \text{ °C}$  and  $T_{90\%} = 378 \text{ °C}$  at  $\text{SV} = 12,000 \text{ mL}/(\text{g h})$ ), which was associated with the synergistic effect of cobalt, iron, and manganese oxides and the high thermal stability for methane combustion [76].

The  $\text{Al}_2\text{O}_3$ - or  $\text{ZrO}_2$ -supported CuO,  $\text{Co}_3\text{O}_4$ , and NiO catalysts exhibited good activities for CO oxidation, which was associated with uniform dispersion of the active phases (copper, cobalt, and nickel oxides) on alumina or zirconia. The intrinsic activity was not enhanced over the supported  $\text{Cr}_2\text{O}_3$  samples, which was due to poor dispersion of chromia

on alumina or zirconia at high temperatures. The CuO/SrTiO<sub>3</sub> sample (Figures 7 and 8) was synthesized by the one-step method, and used for methane combustion due to its low price, outstanding thermal stability, and extraordinary adaptability [77]. The 15 wt% CuO/SrTiO<sub>3</sub> catalyst with a strong metal–support interaction and excellent low-temperature reducibility exhibited the optimal activity ( $T_{50\%} = 527\text{ }^{\circ}\text{C}$  and  $T_{90\%} = 645\text{ }^{\circ}\text{C}$  at SV = 60,000 mL/(g h)) and the highest TOF<sub>Cu</sub> at 400 °C ( $1.08 \times 10^{-3}\text{ s}^{-1}$ ). The authors concluded that the SrTiO<sub>3</sub> perovskite could effectively weaken the copper sintering at high temperatures, which was beneficial for the resistance to sintering and water-induced deactivation. The TiO<sub>2</sub>-supported CuO materials with different crystalline structures were prepared to investigate the support effect and catalytic activity for methane combustion [78]. The 7 wt% CuO/rutile sample obtained a 90% methane conversion at 550 °C at SV = 30,000 mL/(g h). The authors claimed that the superior activity was related to the easily formed Cu species and various chemical states of Cu elements on the stable rutile crystallite. The SnO<sub>2</sub>/In<sub>2</sub>O<sub>3</sub> (i.e., 20 wt% tin oxide + 80 wt% indium oxide) sample showed a complete methane conversion at 600 °C and SV = 30,000 mL/(g h) [79]. Deactivation of the SnO<sub>2</sub>/In<sub>2</sub>O<sub>3</sub> catalyst in the presence of a large amount of water vapor was irreversible. However, the as-prepared sample showed an enhanced SO<sub>2</sub>-tolerant performance by loading of the highly SO<sub>2</sub>-resistant Sn on In<sub>2</sub>O<sub>3</sub>. The authors found that the high performance was attributed to the extra crystal deflection and enhanced oxygen vacancies due to the loading of SnO<sub>2</sub>.

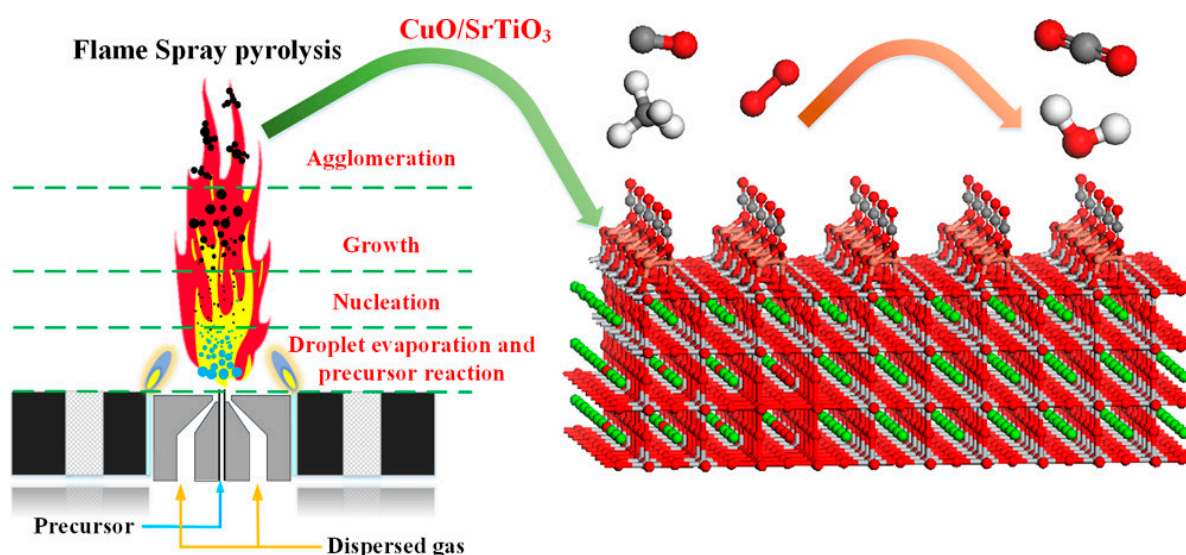


**Figure 7.** Reaction scheme for CuO/SrTiO<sub>3</sub> catalysts. Reprinted with permission from Ref. [77]. Copyright 2021, copyright American Chemical Society.

Manganese is usually used with other elements (e.g., Cu, Co, Ni, and La) to form manganites or manganates, which perform well due to the fact that manganese oxidation states are constantly oscillated between Mn<sup>4+</sup> and Mn<sup>3+</sup>. For example, the manganese-cobalt oxide with a Co/Mn molar ratio of 5:1 achieved the highest methane conversion of 90% at 320 °C and SV = 36,000 mL/(g h) [9], in which the authors pointed out that crystal defects in spinel-type Co<sub>3</sub>O<sub>4</sub> were enhanced after doping an appropriate amount of manganese, which increased the number of the octahedrally coordinated Co<sup>2+</sup> ions, facilitated oxygen mobility, and accelerated the dihydroxylation process.

It is generally known that particle size, surface area, oxygen deficiency density, and porosity are important factors in governing catalytic performance of a catalyst; however, the major drawback of a bulk catalyst is its rapid deactivation caused by sintering of the metal active sites and deposition of carbon. A large surface area is beneficial for the good dispersion of the active sites on the support, and a uniform pore-size distribution is favorable for the inhibition of agglomeration of the active phases, hence enhancing the high-temperature stability and catalytic performance. Ceria is a widely used support

for methane combustion, which exhibits a moderate activity (a low light-off temperature around 300 °C) and a large oxygen-storage capacity. Zeng et al. [80] reported that the  $\text{CeO}_2/\text{Co}_3\text{O}_4$  catalyst with double pore distributions provided a larger number of the active sites as well as the good gas circulation channels, which reduced the internal diffusion resistance and improved the catalytic performance for  $\text{CH}_4$  reforming. Andrey et al. [81] adopted a reverse microemulsion route to obtain ultrahigh dispersion of ceria on the discrete barium hexaaluminate that showed a good high-temperature industrial application potential. The 25 wt%  $\text{CeO}_2/\text{BaAl}_2\text{O}_9$  sample exhibited a low light-off temperature of 400 °C with an  $E_a$  of 145 kJ/mol. Complete methane conversion was achieved over 25 wt%  $\text{CeO}_2/\text{BaAl}_2\text{O}_9$  at 600 °C and  $\text{SV} = 60,000 \text{ mL}/(\text{g h})$ . However, full methane conversion performance was observed during the heating–cooling–restarting cycles in the presence of  $\text{H}_2\text{S}$  and  $\text{H}_2\text{O}$  at 1100 °C. The authors concluded that the superior methane oxidation activity of 25 wt%  $\text{CeO}_2/\text{BaAl}_2\text{O}_9$  was related to its high surface area, low-temperature reducibility, high-temperature thermal stability, excellent poisoning resistance, and synergistic chemical/electronic effect.

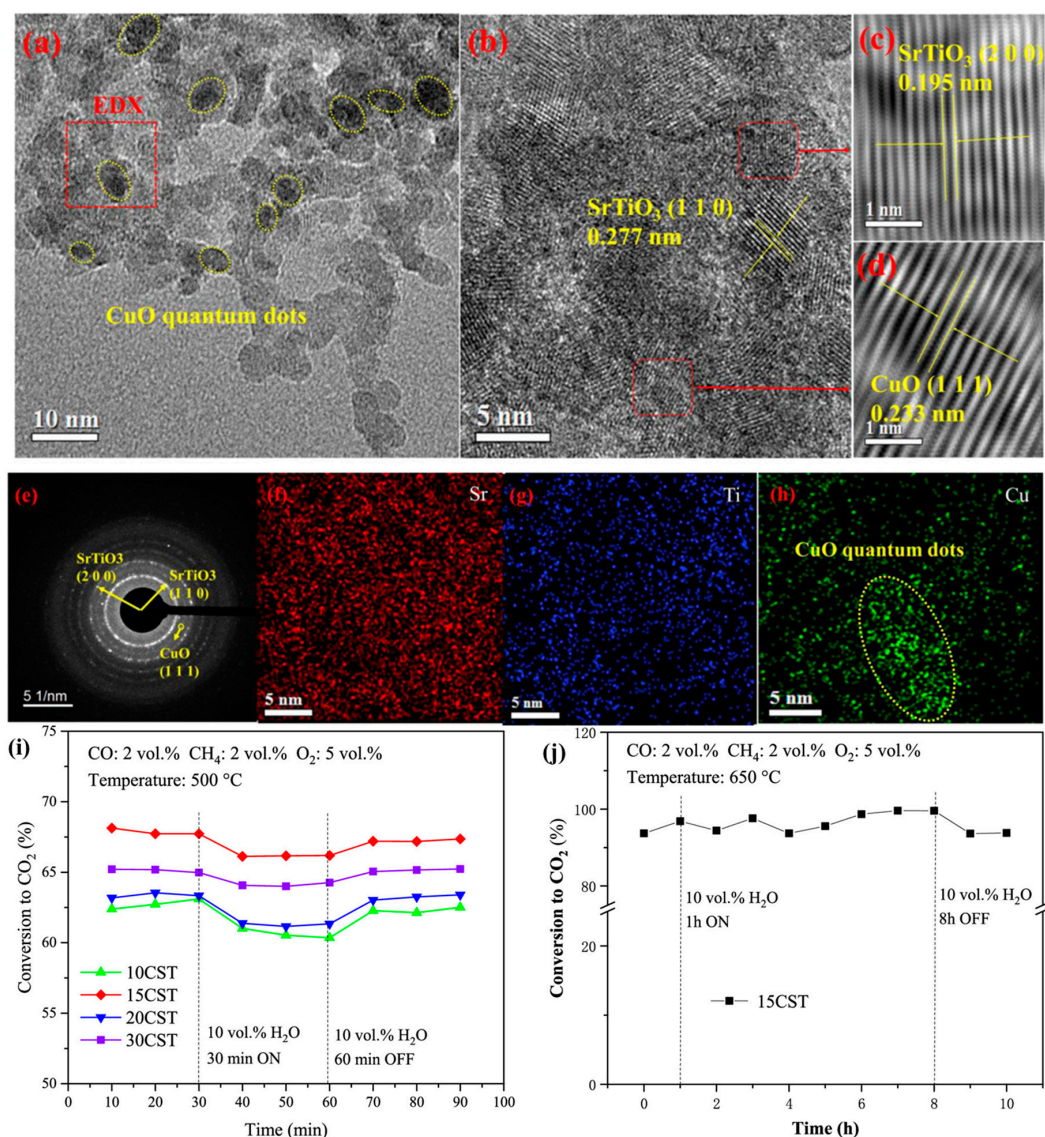


**Figure 8.** TEM analysis of the 15 wt%  $\text{CuO}/\text{SrTiO}_3$  catalysts: HRTEM micrographs (a,b); inverse fast Fourier transform images (c,d); SAED patterns (e); and elemental mapping (f–h); time on stream and in the presence of 10%  $\text{H}_2\text{O}$ : four  $\text{CuO}-\text{SrTiO}_3$  catalysts (i) and 15 wt%  $\text{CuO}/\text{SrTiO}_3$  (j). Reprinted with permission from Ref. [77]. Copyright 2021, copyright American Chemical Society.

Provided that the composite metal oxides do not react with each other under the synthesis conditions, the nanocomposite design and ultrahigh component dispersion achieved through the flexible facile route can be widely used in developing the complex-oxide catalysts with good reactivity and thermal stability for methane conversion. Mesoporous nanocrystalline MgO/Al<sub>2</sub>O<sub>3</sub> materials with surface areas of 253–302 m<sup>2</sup>/g and an average pore size of 7.62 nm were generated using a simple sol–gel approach [82]. The MgO/Al<sub>2</sub>O<sub>3</sub> catalyst showed high methane oxidation activity as well as good resistance against carbon formation. The meso-Fe<sub>2</sub>O<sub>3</sub>-loaded ZrO<sub>2</sub> porous nanobelts with an Fe/Zr molar ratio of 0.25 displayed good methane oxidation activity ( $T_{50\%} = 580\text{ }^{\circ}\text{C}$  and  $T_{90\%} = 650\text{ }^{\circ}\text{C}$  at SV = 25,000 mL/(g h); and  $E_a = 97.9\text{ kJ/mol}$ ) [63]. The mesoporous alumina-supported PdO sample performed well with a 90% methane conversion at 400 °C, which was related to the highly dispersed PdO NPs in the meso-Al<sub>2</sub>O<sub>3</sub> channels [83]. Zhang et al. generated a series of the cordierite monolith-based catalysts by adding CeO<sub>2</sub>, ZrO<sub>2</sub>, La<sub>2</sub>O<sub>3</sub>, or CeO<sub>2</sub>–ZrO<sub>2</sub> as the promoter to form Cu–Mn-complex oxides and tested their methane combustion activities [84]. The introduction of the promoter increased the surface area and appropriately adjusted the porous structure, which favored the ultrahigh dispersion of the active component and the enhancement of oxygen species concentration. The Cu–Mn–Zr–O/Al<sub>2</sub>O<sub>3</sub>/COR monolithic material showed a 90% methane conversion at 570 °C and SV = 20,000 mL/(g h).

Chen and coworkers [85–89] generated the multicomponent catalysts by doping the oxygen-storing rare-earth elements, which exhibited enhanced hydrothermal stability and good CH<sub>4</sub> oxidation activities. This research group demonstrated that the addition of a rare-earth element to the catalyst improved H<sub>2</sub>O tolerance significantly, and initial specific surface area was kept after annealing at 1000 °C. The ZnZrAlO<sub>x</sub> composite with 15 wt% ZnO displayed the light-off and complete conversion temperatures for methane combustion of 278 and 314 °C at SV = 50,000 mL/(g h), while those in the presence of H<sub>2</sub>O were 342 and 371 °C [88], respectively. The TiZrAlO<sub>x</sub> composite with 5 wt% TiO<sub>2</sub> performed the best for CH<sub>4</sub> oxidation, with the  $T_{50\%}$  and  $T_{90\%}$  being 254 and 280 °C at SV = 30,000 mL/(g h) [89], respectively. Du et al. synthesized the cobalt-based monolithic catalysts supported on YSZ–γ-Al<sub>2</sub>O<sub>3</sub> or CeO<sub>2</sub>–Y<sub>2</sub>O<sub>3</sub>–ZrO<sub>2</sub> using the impregnation method, and studied their catalytic activities for CH<sub>4</sub> oxidation [85]. It was found that the CoAl<sub>2</sub>O<sub>4</sub> phase was not formed in the mixture support, thus making the CeO<sub>2</sub>–Y<sub>2</sub>O<sub>3</sub>–ZrO<sub>2</sub> or YSZ–γ-Al<sub>2</sub>O<sub>3</sub> (γ-Al<sub>2</sub>O<sub>3</sub> modified by Y<sub>2</sub>O<sub>3</sub> and ZrO<sub>2</sub>) a multifunctional catalytic support. The loading of 20 wt% Co<sub>3</sub>O<sub>4</sub> on the support made the catalyst perform the best with a 90% methane conversion at 436 °C, which was related to its high surface area, rich oxygen vacancy density, and good thermal stability. Svensson et al. prepared the MgO-based nanocomposite catalysts by adding 20 wt% LaMnO<sub>3</sub> for methane combustion [90]. The sample fabricated by surface precipitation of LaMnO<sub>3</sub> with the Mg nitrate precursor performed the best below 1100 °C. It was reported that NiO/Ce<sub>0.75</sub>Zr<sub>0.25</sub>O<sub>2</sub> with a surface area of 77.9 m<sup>2</sup>/g displayed the  $T_{50\%}$  and  $T_{90\%}$  of 500 and 560 °C for CH<sub>4</sub> oxidation at SV = 36,000 mL/(g h) [91], respectively. The reaction order determined was in good agreement with a pseudo-first order toward CH<sub>4</sub> concentration, and the rate-determining step was the interaction of the dissociatively O<sub>ads</sub> species with CH<sub>4</sub>; furthermore the  $E_a$  values over NiO and Ce<sub>0.75</sub>Zr<sub>0.25</sub>O<sub>2</sub> were 63 and 74 kJ/mol, respectively. Chen et al. synthesized the CeO<sub>2</sub>–Al<sub>2</sub>O<sub>3</sub>–ZrO<sub>2</sub>-supported Fe<sub>2</sub>O<sub>3</sub> catalysts using an impregnation strategy and tested their catalytic activities for methane oxidation [86]. The 8 wt% Fe<sub>2</sub>O<sub>3</sub>-loaded sample performed the best with a 90% methane conversion at 530 °C and SV = 15,000 mL/(g h). The authors believed that the high performance of the 8 wt% Fe<sub>2</sub>O<sub>3</sub>-loaded sample was related to its good thermal stability, high surface area, and ultrahigh component dispersion. Zhang et al. generated the cubically-structured, cauliflower-shaped Ce<sub>0.6</sub>Zr<sub>0.35</sub>Y<sub>0.05</sub>O<sub>2</sub>-supported PdO catalyst with a high surface area of 129 m<sup>2</sup>/g using a hexadecyl trimethyl ammonium bromide template [92]. The 4 wt% PdO/Ce<sub>0.6</sub>Zr<sub>0.35</sub>Y<sub>0.05</sub>O<sub>2</sub> sample with a stable active phase showed a higher methane conversion ( $T_{50\%} = 320\text{ }^{\circ}\text{C}$  and  $T_{90\%} = 360\text{ }^{\circ}\text{C}$  at SV = 50,000 mL/(g h)). The hysteresis phenomenon of methane conversion versus temperature was remarkably decreased by loading

PdO. Dai and coworkers [93] reported the 3D wormhole-like mesopore-structured cubic  $\text{Ce}_{0.6}\text{Zr}_{0.35}\text{Y}_{0.05}\text{O}_2$ -supported  $\text{Ag}_2\text{O}$  catalysts, in which 2.0 wt%  $\text{Ag}_2\text{O}/\text{Ce}_{0.6}\text{Zr}_{0.35}\text{Y}_{0.05}\text{O}_2$  with a high surface area of  $65 \text{ m}^2/\text{g}$  showed the highest activity for methane oxidation ( $T_{50\%} = 540 \text{ }^\circ\text{C}$  and  $T_{90\%} = 600 \text{ }^\circ\text{C}$  at  $\text{SV} = 50,000 \text{ mL}/(\text{g h})$ ), which was related to the stable active  $\text{Ag}_2\text{O}$  phase, strong oxygen storage-release ability, and large surface area. Chen et al. prepared the oxygen-storage  $\text{Ce}_{0.35}\text{Zr}_{0.55}\text{Y}_{0.07}\text{La}_{0.03}\text{O}_{1.95}$ - and  $\text{La}-\text{Al}_2\text{O}_3$ -supported  $\text{Fe}_2\text{O}_3$  catalysts, and evaluated their methane combustion activities [87]. The former sample presented a surface area of  $83 \text{ m}^2/\text{g}$ , over which the  $T_{50\%}$  and  $T_{90\%}$  for methane conversion were 516 and  $565 \text{ }^\circ\text{C}$  at  $\text{SV} = 60,000 \text{ mL}/(\text{g h})$ , respectively. The authors thought that the excellent catalytic activity was attributed to the large surface area, rich  $\text{O}_{\text{ads}}$  species, and strong interaction between  $\text{Fe}_2\text{O}_3$  and  $\text{Ce}_{0.35}\text{Zr}_{0.55}\text{Y}_{0.07}\text{La}_{0.03}\text{O}_{1.95}$ .

Table 2 summarizes catalytic activities of the ordered porous composite oxide and supported metal oxide catalysts for methane oxidation reported in the literature. It can be realized from the above investigations that high methane combustion performance is associated with the unique well-ordered 3D pore structure, high surface area, good thermal stability, and abundant oxygen vacancies of a catalyst.

**Table 2.** Catalytic performance for  $\text{CH}_4$  combustion over the ordered porous composite oxide and supported metal oxide catalysts.

Catalyst	Pore Size (nm)	Surface Area ( $\text{m}^2/\text{g}$ )	Loading (wt%)	$\text{CH}_4$ Concentration (vol%)	SV ( $\text{mL}/(\text{g h})$ )	$T_{50\%}$ ( $^\circ\text{C}$ )	$T_{90\%}$ ( $^\circ\text{C}$ )	Ref.
$\text{Co}_3\text{O}_4/\text{CeO}_2$	–	64.0	7.7	1.0	30,000	401	490	[75]
$\text{Co}_3\text{O}_4/\text{Fe}_2\text{O}_3$	–	–	18	1.0	12,000	480	500	[76]
$\text{Co}_3\text{O}_4/\text{Mn}_2\text{O}_3$	–	–	18	1.0	12,000	400	416	[76]
$\text{Co}_3\text{O}_4/\text{Fe}_2\text{O}_3/\text{Mn}_2\text{O}_3$	–	–	18	1.0	12,000	358	378	[76]
$\text{Co}_3\text{O}_4/\text{MnO}_x$	–	147.65	5:1	1.0	36,000	293	320	[9]
$\text{CuO}/\text{SrTiO}_3$	–	49	15.53	2.0	60,000	527	645	[77]
$\text{CuO}/\text{TiO}_2$	18.9	25.7	7	1.0	30,000	450	550	[78]
$\text{SnO}_2/\text{In}_2\text{O}_3$	–	55.47	20	1.0	30,000	463	505	[79]
$\text{Co}_3\text{O}_4/\gamma\text{-Al}_2\text{O}_3$	–	150	10	1.0	15,000	337	395	[94]
$\text{CeO}_2/\text{ZrO}_2$	100–200	48	20	5.0	30,000	450	>450	[95]
Porous $\text{CeO}_2/\text{Co}_3\text{O}_4$	14	91	40.8	1.0	8000	<700	700	[80]
$\text{CeO}_2/\text{BaAl}_{12}\text{O}_{19}$	–	160	25	1.0	60,000	510	575	[81]
Meso- $\text{MgO}/\text{Al}_2\text{O}_3$	7.62	301.6	2.0	1.0	18,000	600	>700	[82]
Meso- $\text{Fe}_2\text{O}_3/\text{ZrO}_2$	3.4	55.0	0.25	1.99	25,000	580	650	[63]
$\text{PdO}/\text{Meso-}\text{Al}_2\text{O}_3$	–	245	0.98	0.5	6000	350	400	[83]
$\text{Co}_3\text{O}_4/\text{Y}_2\text{O}_3\text{-ZrO}_2\text{-}\gamma\text{-Al}_2\text{O}_3+\text{CeO}_2\text{-Y}_2\text{O}_3\text{-ZrO}_2$	–	115.6	20	1.0	20,000	402	436	[85]
$\text{LaMnO}_3/\text{MgO}$	–	11.5	20	1.5	100,000	670	750	[90]
$\text{NiO}/\text{Ce}_{0.75}\text{Zr}_{0.25}\text{O}_2$	–	77.9	5	3.0	39,000	500	560	[91]
$\text{Y}_2\text{O}_3/\text{YBa}_2\text{Cu}_3\text{O}_7$	–	6.1	–	0.1	50,000	649	711	[96]
$\text{Fe}_2\text{O}_3/\text{Ce}_{0.67}\text{Zr}_{0.33}\text{O}_2\text{-}\text{Al}_2\text{O}_3$	–	164.5	8	1.0	15,000	515	530	[86]
$\text{MnO}_x/3\text{DOM CoFe}_2\text{O}_4$	83–123	21.1	6.7	2.5	20,000	425	520	[51]
$\text{Co}_3\text{O}_4/3\text{DOM MnCo}_2\text{O}_4$	180–200	41.1	18.2	2.5	40,000	350	480	[59]
$\text{AuO}_x/\text{meso-}\text{Ce}_{0.6}\text{Zr}_{0.3}\text{Y}_{0.1}\text{O}_2$	5.0	88	0.2	2.5	50,000	600	660	[64]
$\text{PdO}/\text{meso-}\text{Ce}_{0.2}\text{Zr}_{0.35}\text{Y}_{0.05}\text{O}_2$	3–7	120.1	4.0	2.5	50,000	320	360	[92]
$\text{Ag}_2\text{O}/\text{meso-}\text{Ce}_{0.2}\text{Zr}_{0.35}\text{Y}_{0.05}\text{O}_2$	6.5	65	2.0	2.5	50,000	540	600	[93]
$\text{Cu-Mn-O}/\text{Al}_2\text{O}_3/\text{COR}$	3.7	30.6	13.1	1.0	20,000	468	>700	[84]
$\text{Cu-Mn-Ce-O}/\text{Al}_2\text{O}_3/\text{COR}$	4.0	34.6	13.1	1.0	20,000	420	640	[84]
$\text{Cu-Mn-Zr-O}/\text{Al}_2\text{O}_3/\text{COR}$	4.2	37.4	13.1	1.0	20,000	400	581	[84]
$\text{Cu-Mn-La-O}/\text{Al}_2\text{O}_3/\text{COR}$	3.8	31.6	13.1	1.0	20,000	440	630	[84]
$\text{Cu-Mn-Ce-Zr-O}/\text{Al}_2\text{O}_3/\text{COR}$	4.1	34.3	13.1	1.0	20,000	430	650	[84]
$\text{Fe}_2\text{O}_3/\text{Ce}_{0.35}\text{Zr}_{0.55}\text{Y}_{0.07}\text{La}_{0.03}\text{O}_{1.95}/\text{LaAl}_2\text{O}_3$	–	83	8	1.0	50,000	516	565	[87]

### 3.3. Supported Noble Metal Catalysts

Noble metals catalysts are studied for low light-off temperatures and good C–H activation ability. However, uniformly dispersed noble metals NPs are easily sintered and aggregated to form nanoclusters at high temperatures with increased sizes, leading to poor thermal stability and irreversible catalyst deactivation. The design and preparation of the active components with specific structures can greatly improve thermal stability of the catalysts, and the addition of a base metal to noble metal(s) presents an optimized noble metals utilization efficiency with a less cost. The noble metal reduction is one of the most promising prospects for commercial applications by enhancing the efficiency of noble metal utilization, such as monoatomic, noble metal transition metal alloy, core–shell structure design, and suitable support selection. Recently, Dai's group successfully embedded partially Pt NPs in the skeleton of a 3DOM  $\text{Mn}_2\text{O}_3$  support, which exhibited an excellent thermal stability and catalytic performance compared with the catalyst derived from the PVA-

protecting reduction approach [52]. Another innovative strategy was developed by coating noble metals with metal oxides to construct the shell (metal oxide)-core (noble metal) structure to protect the active component. Xie et al. [27] designed core-shell-structured Pd@Co (core: Pd; shell: Co) NPs to successfully stabilize Pd NPs and avoid sintering of the noble metal. Multiple core-shell confinement was used to fabricate the confined ultrathin Pd@CeO<sub>x</sub> nanowire (2.4 nm in diameter) catalysts with superior hydrothermal stability below 800 °C [97]. The multiple core-shell confinement effectively enhanced the interaction between metal and oxide with an ultrahigh component dispersion. The confinement and shielding effect significantly restricted the active center in the support to avoid sintering and agglomeration. The use of rare-earths or transition-metal oxides as catalyst modifiers can improve the dispersion and thermal stability of noble metals and reduce their use quantities, while the use of the more thermally stable and catalytically active oxides (e.g., perovskites and hexaaluminates) as supports can achieve the same target.

The unoccupied *d*-electron orbitals of noble metals are beneficial for adsorption and activation of the reactants, which is responsible for good low-temperature reducibility and strong sulfur-dioxide-tolerant ability of a supported noble metal material. Appropriate supports (e.g., transition-metal oxides and perovskite-type oxides) can obviously promote the improvements in thermal stability and low-temperature selectivity as well as enhance catalytic activities of their supported precious metal catalysts. Meanwhile, the noble metal particle size mainly determines the number of the exposed active sites, thus playing an important part in catalytic oxidation and maximal utilization of noble metals. Another important reason for deactivation of the supported precious metal catalysts is agglomeration during the sintering process. Taking all of these factors into account, loading precious metals on the surface of a 3D ordered macro- or mesoporous metal oxide is a creditable strategy to protect the noble metals from being sintered. The active noble metals are uniformly dispersed on the surface of a substrate, and such supported catalysts show enhanced catalytic activities and thermal stability for CH<sub>4</sub> combustion due to a strong metal–support interaction. Zhao et al. [29] adopted the KIT-6-templating method to successfully generate mesoporous cubic Pd, Pt, and Pd<sub>x</sub>Pt ( $x = 0.43\text{--}8.52$ ) for CH<sub>4</sub> oxidation. It was found that Pd and Pt were uniformly distributed in the ordered mesoporous Pd<sub>x</sub>Pt alloys with surface areas of 26–32 m<sup>2</sup>/g and average pore sizes of 13.7–19.8 nm. The redox property of Pd showed a significant adjustment by Pt doping, and the Pt–Pd oxide (i.e., PdO–PtO<sub>2</sub>) exhibited better catalytic activity than the metallic Pt<sup>0</sup>–Pd<sup>0</sup> with a good thermal stability. The meso-Pd, meso-Pt, and meso-Pd<sub>2.41</sub>Pt showed the  $T_{50\%}$  and  $T_{90\%}$  values of 350, 372, 303, and 368, 506, and 322 °C at SV = 100,000 mL/(g h), respectively, among which meso-Pd<sub>2.41</sub>Pt performed the best, with the highest TOF<sub>Pd+Pt</sub> and specific reaction rate of  $0.59 \times 10^{-3} \text{ s}^{-1}$  and 4.46 μmol/(g<sub>cat</sub> s) at 280 °C, respectively. Partial deactivation of the Pd<sub>2.41</sub>Pt catalyst caused by the introduction of carbon dioxide or water vapor was reversible, while the deactivation caused by the addition of SO<sub>2</sub> was irreversible. The authors believed that the well-ordered and developed mesoporous structure and good oxygen activation ability were accountable for the high catalytic activity. Cargnello et al. [98] developed a supramolecular approach to deposit a palladium (Pd) core and a ceria (CeO<sub>2</sub>) shell on a modified hydrophobic alumina. The commercial alumina substrate was highly hydrophilic, while the active component Pd@CeO<sub>2</sub> was hydrophobic. The hydrophobic Pd@CeO<sub>2</sub> structure presented an agglomeration instead of adhering to alumina, resulting in irreversible deactivation of such a catalyst. The authors aimed to develop an efficiency strategy to regulate special properties of alumina surface to be hydrophobic and deposit the active component as a single unit on the substrate surface. The alumina surface was decorated by organosilane triethoxy(octyl)silane to ensure the surface would be covered by the formed alkyl chain, leading to a larger adsorption capacity of the Pd@CeO<sub>2</sub> structure without deactivation. The droplets of water deposited on the hydrophobic alumina were repulsed instead of the favorable interaction with the OH groups in alumina, which further confirmed the adopted tactic. The as-prepared sample showed a remarkable higher methane oxidation activity ( $T_{50\%} = 250 \text{ °C}$   $T_{90\%} = 300 \text{ °C}$  at SV = 200,000 mL/(g h)), with

the highest TOF and the lowest  $E_a$  of  $47 \times 10^{-3} \text{ s}^{-1}$  and  $103 \text{ kJ/mol}$  at  $250 \text{ }^\circ\text{C}$ , respectively. Furthermore, the supported catalyst remained intact without segregation or agglomeration during the calcination process at  $850 \text{ }^\circ\text{C}$ . The authors pointed out that excellent complete methane oxidation activity was associated with the strong metal–support synergy interaction, well-defined ordered mesoporous structure, and good thermal stability under the adopted reaction conditions.

Generally speaking, it is accepted that the microstructure and function of single-noble-metal NPs can be modified by introducing a trace amount of a transition metal (Cr, Mn, Fe, or Co) or a noble metal (Au, Pd, Pt, or Ru). On this basis, Dai's group investigated methane combustion over the supported noble–M (M = Au, Pd, Pt, Ru, Cr, Mn, Fe, and Co) NPs with enhanced oxygen activation ability and less noble metal use. Numerous experiments demonstrated that the facilely formed noble alloy NPs showed an excellent methane oxidation activity and good thermal stability as well as the valid noble metal utilization. Over the last 15 years, Dai's group fabricated a series of the 3DOM-structured macro- or mesoporous mixed-metal-oxides-supported precious metal (Au, Pd, Pt, Ru, and alloy) catalysts with high surface areas and ordered porous channels using the PMMA- or KIT-6-templating and PVA-protecting reduction approaches, such as AuPd/meso- $\text{Co}_3\text{O}_4$  (mesopore diameter = 11–15 nm and surface area =  $104\text{--}115 \text{ m}^2/\text{g}$ ) [28], PdPt/meso- $\text{Mn}_2\text{O}_3$  (mesopore diameter = 9.3–12.6 nm and surface area =  $76.5\text{--}95.3 \text{ m}^2/\text{g}$ ), AuRu/meso- $\text{Mn}_2\text{O}_3$  (mesopore diameter = 9.9–20.2 nm and surface area =  $98.8\text{--}104.8 \text{ m}^2/\text{g}$ ) [54], AuPd/3DOM  $\text{CoCr}_2\text{O}_4$  (macropore diameter = 120–180 nm and surface area =  $33\text{--}36 \text{ m}^2/\text{g}$ ) [48], AuPd/3DOM  $\text{La}_{0.6}\text{Sr}_{0.4}\text{MnO}_3$  (macropore diameter = 126–150 nm and surface area =  $32.0\text{--}33.6 \text{ m}^2/\text{g}$ ) [49], PdPt/3DOM  $\text{LaMnAl}_{11}\text{O}_{19}$  (macropore diameter = 97–113 nm and surface area =  $26.3\text{--}29.0 \text{ m}^2/\text{g}$ ) [20,50], PdPt/ $\text{MnO}_x$ /3DOM  $\text{CoFe}_2\text{O}_4$  (macropore diameter = 83–123 nm and surface area =  $19\text{--}28 \text{ m}^2/\text{g}$ ) [51], Au–Pd–Co/3DOM  $\text{Mn}_2\text{O}_3$  (macropore diameter = 175–205 nm and surface area =  $36.9\text{--}38.5 \text{ m}^2/\text{g}$ ) [25], Au–Pd–CoO/3DOM  $\text{Co}_3\text{O}_4$  (macropore diameter = 115–185 nm and surface area =  $27\text{--}47 \text{ m}^2/\text{g}$ ) [26], CoPd/3DOM  $\text{CeO}_2$  (macropore diameter = 145–165 nm and surface area =  $36.7\text{--}41.2 \text{ m}^2/\text{g}$ ) [27], Ag/3DOM  $\text{La}_{0.6}\text{Sr}_{0.4}\text{MnO}_3$  (macropore diameter = 101 nm and surface area =  $41.5 \text{ m}^2/\text{g}$ ) [47], and Pt/3DOM  $\text{Ce}_{0.6}\text{Zr}_{0.3}\text{Y}_{0.1}\text{O}_2$  (macropore diameter = 121–147 nm and surface area =  $84\text{--}95 \text{ m}^2/\text{g}$ ) (Figure 9) [99]. Dai and coworkers systematically studied the correlation between noble metal and several diverse supports in methane oxidation. It was observed that AuPd NPs were uniformly distributed on the surface of meso- $\text{Co}_3\text{O}_4$  with an average size of 2.7–4.5 nm [28]. The  $2.94\text{Au}_{0.50}\text{Pd}/\text{meso-}\text{Co}_3\text{O}_4$  exhibited an excellent activity and possessed the highest specific reaction rate at  $260 \text{ }^\circ\text{C}$  ( $1.47 \mu\text{mol}/(\text{g}_{\text{cat}} \text{ s})$ ,  $91.7 \mu\text{mol}/(\text{g}_{\text{noble metal}} \text{ s})$  or  $1.50 \mu\text{mol}/(\text{g}_{\text{Co}_3\text{O}_4} \text{ s})$ ). Over the  $2.94\text{Au}_{0.50}\text{Pd}/\text{meso-}\text{Co}_3\text{O}_4$  sample at a SV of  $20,000 \text{ mL}/(\text{g h})$ , the  $T_{10\%}$ ,  $T_{50\%}$ , and  $T_{90\%}$  were 230, 280, and  $324 \text{ }^\circ\text{C}$  with the lowest  $E_a$  and the highest TOF<sub>AuPd</sub> of  $44.4 \text{ kJ/mol}$  and  $12.23 \times 10^{-3} \text{ s}^{-1}$ , respectively. Similarly, among the meso- $\text{Mn}_2\text{O}_3$ -supported PdPt alloy (2.1–2.8 nm in particle size) samples [100],  $1.41(\text{Pd}_{5.1}\text{Pt})/\text{meso-}\text{Mn}_2\text{O}_3$  showed the best methane oxidation performance: The  $T_{10\%}$ ,  $T_{50\%}$ , and  $T_{90\%}$  were 265, 345, and  $425 \text{ }^\circ\text{C}$ , respectively; the highest TOF<sub>PdPt</sub> was  $1.02 \times 10^{-3} \text{ s}^{-1}$ , and the best specific reaction rate was  $6.39 \mu\text{mol}/(\text{g}_{\text{cat}} \text{ s})$  or  $6.48 \mu\text{mol}/(\text{g}_{\text{Mn}_2\text{O}_3} \text{ s})$  at  $400 \text{ }^\circ\text{C}$ . In addition, the as-prepared sample displayed the increased endurance performance in the presence of  $\text{SO}_2$ ,  $\text{CO}_2$ , or  $\text{H}_2\text{O}$  by introducing an appropriate amount of Pt. Moreover, AuRu/meso- $\text{Mn}_2\text{O}_3$  was generated to improve the reducibility, and the  $0.97\text{AuRu}/\text{meso-}\text{Mn}_2\text{O}_3$  sample showed the highest activity ( $T_{50\%} = 470 \text{ }^\circ\text{C}$  and  $T_{90\%} = 540 \text{ }^\circ\text{C}$  at SV =  $20,000 \text{ mL}/(\text{g h})$ ) [54]. The same group investigated the Cr-based spinel-type-oxides-supported gold–palladium alloy materials with abundant  $\text{O}_{\text{ads}}$  concentrations and good reducibility for methane combustion. The  $1.93\text{AuPd}_{1.95}/3\text{DOM } \text{CoCr}_2\text{O}_4$  catalyst exhibited the highest methane conversion ( $T_{50\%} = 353 \text{ }^\circ\text{C}$  and  $T_{90\%} = 394 \text{ }^\circ\text{C}$  at SV =  $20,000 \text{ mL}/(\text{g h})$ ) with the superior TOF<sub>AuPd</sub> ( $0.271 \times 10^{-3} \text{ s}^{-1}$ ) and the highest specific reaction rate ( $1.15 \mu\text{mol}/(\text{g}_{\text{cat}} \text{ s})$ ) at  $320 \text{ }^\circ\text{C}$  [48]. The presence of  $\text{SO}_2$  in the reaction system over the  $0.97\text{AuRu}/\text{meso-}\text{Mn}_2\text{O}_3$  sample caused a permanent loss in activity, while the partial deactivation due to moisture introduction was reversible. The AuPd/3DOM  $\text{La}_{0.6}\text{Sr}_{0.4}\text{MnO}_3$  bimetallic catalysts (Figure 10) were prepared with a good thermal stability and rich adsorbed oxygen species [49], among

which 2.92AuPd/3DOM La<sub>0.6</sub>Sr<sub>0.4</sub>MnO<sub>3</sub> with the appropriate Au/Pd molar ratio of 1:2 exhibited the  $T_{50\%}$  and  $T_{90\%}$  values of 314 and 336 °C at SV = 50,000 mL/(g h) for CH<sub>4</sub> oxidation. This sample exhibited the highest TOF<sub>AuPd</sub> ( $10.2 \times 10^{-3} \text{ s}^{-1}$ ) and the lowest  $E_a$  (72.4 kJ/mol). The size of the bimetallic Au–Pd catalyst increased from 2.15 to 3.76 nm upon exposure to water, indicating that the presence of water vapor caused an irreversible deactivation. AAl<sub>2</sub>O<sub>3</sub> is regarded as a promising catalyst candidate due to its sintering temperature at above 1200 °C (i.e., it possesses a good thermal stability). The same research group also tested methane combustion activities over PdPt/3DOM LaMnAl<sub>11</sub>O<sub>19</sub> with noble metal particle sizes of 3–5 nm [20,50]. The 1.14Pd<sub>2.8</sub>Pt/3DOM LaMnAl<sub>11</sub>O<sub>19</sub> sample showed the best activity, with the  $T_{10\%}$ ,  $T_{50\%}$ , and  $T_{90\%}$  values being 284, 372, and 456 °C at SV = 20,000 mL/(g h), respectively. The ex situ X-ray photoelectron spectroscopy (ex situ XPS) was used to investigate formation of the active PdO species during the oxidation process of Pd in 1.14Pd<sub>2.8</sub>Pt/3DOM LaMnAl<sub>11</sub>O<sub>19</sub> at different temperatures. Doping with an appropriate amount of Pt to the supported Pd catalyst could improve H<sub>2</sub>O, CO<sub>2</sub>, and SO<sub>2</sub> tolerance. Recently, the same group investigated the ternary catalysts (which were combined with noble metal NPs, transition-metal oxide, and porous spinel-type mixed oxide) for methane combustion. The as-prepared PdPt/MnO<sub>x</sub>/3DOM CoFe<sub>2</sub>O<sub>4</sub> sample with a PdPt particle size of 2.2–3.0 nm exhibited the highest O<sub>ads</sub> species concentration and the best low-temperature reducibility [51]. The 1.81PdPt/6.7MnO<sub>x</sub>/3DOM CoFe<sub>2</sub>O<sub>4</sub> sample showed the highest activity ( $T_{10\%} = 255 \text{ °C}$ ,  $T_{50\%} = 301 \text{ °C}$ , and  $T_{90\%} = 372 \text{ °C}$  at SV = 20,000 mL/(g h);  $E_a = 59 \text{ kJ/mol}$ ; TOF<sub>Noble metal</sub> =  $37.44 \times 10^{-3} \text{ s}^{-1}$ , and TOF<sub>CoFe<sub>2</sub>O<sub>4</sub></sub> =  $0.28 \times 10^{-3} \text{ s}^{-1}$ ).

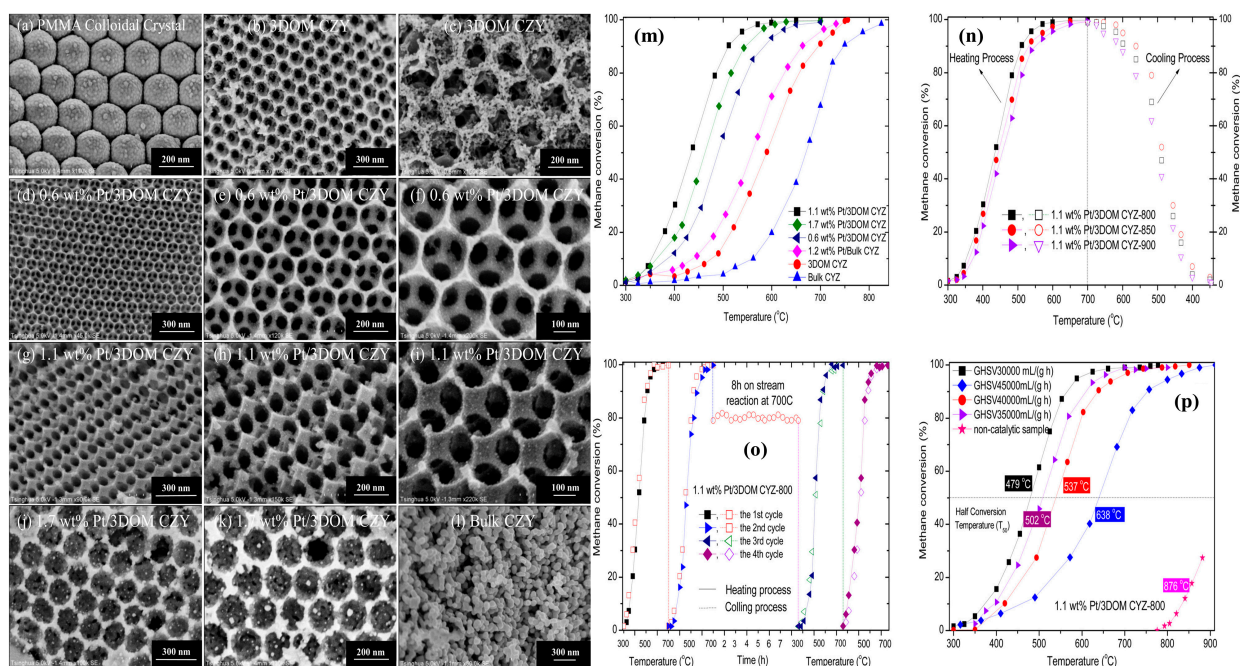


**Figure 9.** (a–l) HRSEM images of the 3DOM Ce<sub>0.6</sub>Zr<sub>0.3</sub>Y<sub>0.1</sub>O<sub>2</sub> support and  $x$  wt% Pt/3DOM Ce<sub>0.6</sub>Zr<sub>0.3</sub>Y<sub>0.1</sub>O<sub>2</sub> and Bulk Ce<sub>0.6</sub>Zr<sub>0.3</sub>Y<sub>0.1</sub>O<sub>2</sub> catalysts; (m) methane conversion versus temperature over the 3DOM Ce<sub>0.6</sub>Zr<sub>0.3</sub>Y<sub>0.1</sub>O<sub>2</sub>,  $x$  wt% Pt/3DOM Ce<sub>0.6</sub>Zr<sub>0.3</sub>Y<sub>0.1</sub>O<sub>2</sub>, and bulk Ce<sub>0.6</sub>Zr<sub>0.3</sub>Y<sub>0.1</sub>O<sub>2</sub> catalysts; (n) methane conversion versus temperature on different calcination; (o) catalytic stability of the 1.1 wt% Pt/3DOM Ce<sub>0.6</sub>Zr<sub>0.3</sub>Y<sub>0.1</sub>O<sub>2</sub> catalyst; (p) effect of GHSV on the catalytic activity over the 1.1 wt% Pt/3DOM Ce<sub>0.6</sub>Zr<sub>0.3</sub>Y<sub>0.1</sub>O<sub>2</sub> catalyst at GHSV = 30,000 mL/(g h) under the conditions of 2 vol% CH<sub>4</sub> + 20 vol% O<sub>2</sub> + 78 vol% N<sub>2</sub> (balance) and total flow of 41.6 mL/min. Reprinted with permission from Ref. [99]. Copyright 2015, copyright American Chemical Society.

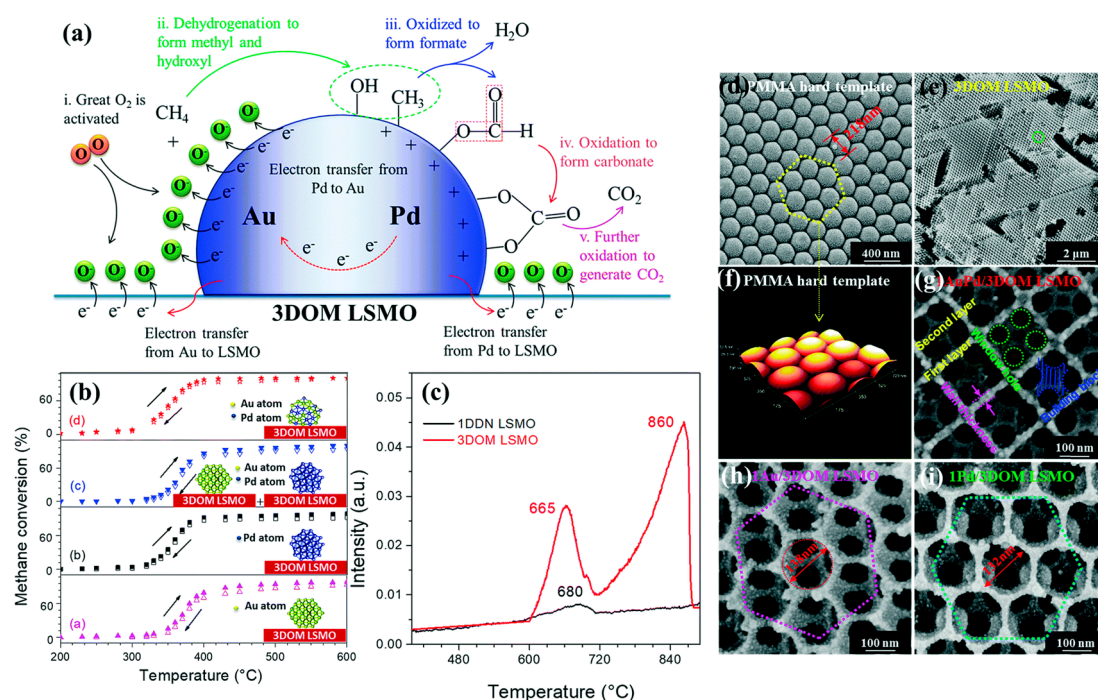


**Figure 10.** (a) Proposed elementary steps for the oxidation of methane over 1AuPd/3DOM LSMO; (b) methane conversion; (c) NH<sub>3</sub>-TPD profiles of 1DDN LSMO and 3DOM LSMO samples; (d–i) HRSEM and 3D-eAFM images of PMMA, 3DOM LSMO, and noble-metal-supported 3DOM LSMO. Reprinted with permission from Ref. [49]. Copyright 2016, copyright American Chemical Society.

After a brief discussion, we can realize from the data summarized in Table 3 that methane combustion activity over the various 3DOM-structured mixed-metal-oxides-supported noble metal (Au, Pd, Pt, Ru, and alloy) catalysts decrease in the order of 2.94Au<sub>0.50</sub>Pd/meso-Co<sub>3</sub>O<sub>4</sub> ( $T_{90\%} = 324\text{ }^{\circ}\text{C}$ ) > 2.92AuPd/3DOM La<sub>0.6</sub>Sr<sub>0.4</sub>MnO<sub>3</sub> ( $T_{90\%} = 336\text{ }^{\circ}\text{C}$ ) > 1.81PdPt/6.7MnO<sub>x</sub>/3DOM CoFe<sub>2</sub>O<sub>4</sub> ( $T_{90\%} = 372\text{ }^{\circ}\text{C}$ ) > 1.93AuPd<sub>1.95</sub>/3DOM CoCr<sub>2</sub>O<sub>4</sub> ( $T_{90\%} = 394\text{ }^{\circ}\text{C}$ ) > 1.41(Pd<sub>5.1</sub>Pt)/meso-Mn<sub>2</sub>O<sub>3</sub> ( $T_{90\%} = 425\text{ }^{\circ}\text{C}$ ) > 1.14Pd<sub>2.8</sub>Pt/3DOM LaMnAl<sub>11</sub>O<sub>19</sub> ( $T_{90\%} = 456\text{ }^{\circ}\text{C}$ ) > 0.97AuRu/meso-Mn<sub>2</sub>O<sub>3</sub> ( $T_{90\%} = 540\text{ }^{\circ}\text{C}$ ). The authors assigned high methane oxidation activity of the typical catalyst to its high surface area with well-ordered and developed porous structure, abundant active oxygen species, good thermal stability, good low-temperature reducibility, and strong interaction between noble metal NPs and 3DOM-structured support.

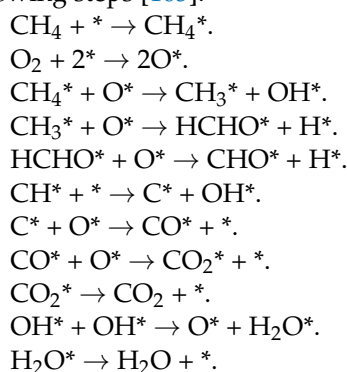
**Table 3.** Catalytic performance for CH<sub>4</sub> combustion over the ordered porous composite oxide and supported noble metal catalysts.

Catalyst	Pore Size (nm)	Surface Area (m <sup>2</sup> /g)	Mean Noble Metal Particle Size (nm)	Noble Metal Loading (wt%)	CH <sub>4</sub> Concentration (vol%)	SV (mL/(g h))	T <sub>50%</sub> (°C)	T <sub>90%</sub> (°C)	Ref.
Meso-Pd <sub>2.41</sub> Pt	18.1	25.5	7.1	–	2.5	100,000	303	322	[29]
Meso-Pd	19.8	30.2	9.4	–	2.5	100,000	350	368	[29]
Meso-Pt	13.7	31.1	6.8	–	2.5	100,000	372	506	[29]
Porous Pd/CeO <sub>2</sub> /Al <sub>2</sub> O <sub>3</sub>	15	43	2.2	1	0.5	200,000	250	300	[98]
Pd/meso-Co <sub>3</sub> O <sub>4</sub>	13.6	108.1	4.5	1.58	2.5	20,000	288	334	[28]
Au/meso-Co <sub>3</sub> O <sub>4</sub>	13.4	109.6	2.7	1.48	2.5	20,000	312	378	[28]
AuPd/meso-Co <sub>3</sub> O <sub>4</sub>	13.5	114.5	3.5	1.94	2.5	20,000	280	324	[28]
Pd/meso-Mn <sub>2</sub> O <sub>3</sub>	9.3	89.9	2.8	1.40	2.5	20,000	380	460	[100]
Pt/meso-Mn <sub>2</sub> O <sub>3</sub>	9.9	83.5	2.5	1.42	2.5	20,000	400	495	[100]
1.41PdPt/meso-Mn <sub>2</sub> O <sub>3</sub>	9.6	85.1	2.5	1.42	2.5	20,000	345	425	[100]
Au/meso-Mn <sub>2</sub> O <sub>3</sub>	10.1	100.6	2–5	0.49	2.5	20,000	480	580	[54]
Ru/meso-Mn <sub>2</sub> O <sub>3</sub>	10.0	99.7	2–5	0.48	2.5	20,000	465	530	[54]
AuRu/meso-Mn <sub>2</sub> O <sub>3</sub>	9.9	98.8	2–5	0.97	2.5	20,000	470	540	[54]
AuPd <sub>1.95</sub> /3DOM CoCr <sub>2</sub> O <sub>4</sub>	120–180	34.9	3.3	1.93	2.5	20,000	353	394	[48]
Au/3DOM La <sub>0.6</sub> Sr <sub>0.4</sub> MnO <sub>3</sub>	130–145	32.6	2.4	0.94	5.0	50,000	375	402	[49]
Pd/3DOM La <sub>0.6</sub> Sr <sub>0.4</sub> MnO <sub>3</sub>	135–150	32.0	2.3	0.85	5.0	50,000	358	378	[49]

Table 3. Cont.

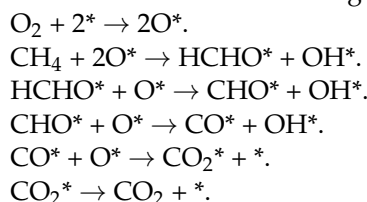
Catalyst	Pore Size (nm)	Surface Area (m <sup>2</sup> /g)	Mean Noble Metal Particle Size (nm)	Noble Metal Loading (wt%)	CH <sub>4</sub> Concentration (vol%)	SV (mL/(g h))	T <sub>50%</sub> (°C)	T <sub>90%</sub> (°C)	Ref.
AuPd/3DOM La <sub>0.6</sub> Sr <sub>0.4</sub> MnO <sub>3</sub>	128–135	33.8	2.2	2.92	5.0	50,000	314	336	[49]
Pt/3DOM LaMnAl <sub>11</sub> O <sub>19</sub>	113	27.6	4.4	0.94	2.5	20,000	437	515	[20]
PdPt/3DOM LaMnAl <sub>11</sub> O <sub>19</sub>	107	28.9	4.3	1.14	2.5	20,000	487	549	[20]
Pd/3DOM LaMnAl <sub>11</sub> O <sub>19</sub>	97	28.8	2–5	0.97	2.5	20,000	308	343	[50]
Pt/MnO <sub>x</sub> /3DOM CoFe <sub>2</sub> O <sub>4</sub>	83–123	19	2.3	0.93	2.5	20,000	420	527	[51]
Pd/MnO <sub>x</sub> /3DOM CoFe <sub>2</sub> O <sub>4</sub>	83–123	19.8	2.2	0.89	2.5	20,000	409	491	[51]
PdPt/MnO <sub>x</sub> /3DOM CoFe <sub>2</sub> O <sub>4</sub>	83–123	27.8	3.0	2.10	2.5	20,000	301	372	[51]
Au–Pd/3DOM Mn <sub>2</sub> O <sub>3</sub>	180–195	37.7	3.7	1.97	2.5	40,000	393	440	[25]
Au–Pd–Co/3DOM Mn <sub>2</sub> O <sub>3</sub>	175–205	38.1	3.6	1.94	2.5	40,000	365	442	[25]
Au–Pd/3DOM Co <sub>3</sub> O <sub>4</sub>	115–135	35	2.6	1.99	2.5	20,000	337	379	[26]
Au–Pd–CoO/3DOM Co <sub>3</sub> O <sub>4</sub>	130–140	35	2.7	1.99	2.5	20,000	312	341	[26]
Au–Pd–CoO/3DOM Mn <sub>2</sub> O <sub>3</sub>	175–185	47	3.1	1.97	2.5	20,000	430	500	[26]
Au–Pd–CoO/3DOM Al <sub>2</sub> O <sub>3</sub>	150–160	27	3.0	1.95	2.5	20,000	543	625	[26]
Co/3DOM CeO <sub>2</sub>	150–165	37.9	3.5	0.71	2.5	40,000	590	>600	[27]
CoPd/3DOM CeO <sub>2</sub>	150–160	36.7	4.1	0.77	2.5	40,000	430	480	[27]
Ag/3DOM La <sub>0.6</sub> Sr <sub>0.4</sub> MnO <sub>3</sub>	101	41.5	3.2	3.63	2.0	30,000	454	524	[47]
AuPd/Co <sub>3</sub> O <sub>4</sub> /3DOM MnCo <sub>2</sub> O <sub>4</sub>	180–200	53.1	4.6	1.98	2.5	40,000	340	408	[59]
Pd/3DOM La <sub>0.6</sub> Sr <sub>0.4</sub> MnO <sub>3</sub>	175–185	23.6	5.5	1.18	2.5	40,000	489	583	[65]
Pt/3DOM Ce <sub>0.6</sub> Zr <sub>0.3</sub> Y <sub>0.1</sub> O <sub>2</sub>	120–147	84–95	2v5	0.6	2.0	30,000	489	543	[99]

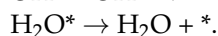
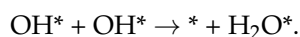
Supported noble metals catalysts are generally divided into two forms: metallic state and oxidized state. The oxygen on the surface of the metal phase is usually adsorbed oxygen, which exhibits a low adsorption energy. Methane dissociation is generally considered to be a rate-determining step, and reaction kinetics are discussed according to the Eley-Rideal (E-R) [101] and Langmuir-Hinshelwood (L-H) mechanisms [102]. Metal oxides always coordinate with metal atoms and lattice oxygen, where the adsorption energy of lattice oxygen is higher than that of the adsorbed oxygen. The consumed lattice oxygen during the catalytic methane oxidation process is then made up by gaseous oxygen. In this case, the Mars-van Krevelen (MvK) mechanism is proposed to discuss the redox process [103]. Methane and oxygen are adsorbed on the surface of a catalyst according to the L–H mechanism. Different intermediates are formed by adsorption and activation of methane during the dehydrogenation process. The dehydrogenation process from CH<sub>4</sub> to the C\* species on the Pd surface was revealed by the first-principles simulation [104]. The reaction process of the adsorbed methane and oxygen species can be described using the following steps [105]:



Here, \* represents the active adsorption sites, and X\* represents the adsorbed X species at the active sites.

The reaction process of the gaseous methane and adsorbed oxygen species in the E-R mechanism can be described using the following steps:





The mechanism of methane oxidation with lattice oxygen vacancy formation via the MvK redox steps over PdO (101) was investigated. Rate-controlling analysis reveals that the dissociative CH<sub>4</sub> adsorption via hydrogen abstraction over the Pd<sub>cus</sub>-O<sub>cus</sub> site-pairs was the rate-determining step during the light-off process. Methane is first adsorbed on the surface of a catalyst and then reacts with lattice oxygen to form CO<sub>2</sub> and H<sub>2</sub>O in the MvK redox mechanism. Detailed methane oxidation reaction path analysis (RPA) has been discussed for the dry and the wet reaction mixture with 12 vol% water in the feedstock at 1 bar to elucidate the preferential pathway. Methane is adsorbed and reacted with lattice oxygen to generate the side products in sequence under the dry condition and temperatures of 200–400 °C: CH<sub>4</sub> → CH<sub>3</sub> → CH<sub>2</sub>OH → CH<sub>2</sub>O → CHO → CO → CO<sub>2</sub>. Molecular H<sub>2</sub>O adsorption or desorption contributes to vacancy formation through O<sub>2</sub> adsorption from gas-phase and hydroxide formation or decomposition. The preferential path under the dry condition and temperatures above 400 °C is similar to that under the wet condition: CH<sub>4</sub> → CH<sub>3</sub> → CH<sub>2</sub> → CH<sub>2</sub>O → CHO → CO → CO<sub>2</sub>. The major difference is reaction sequence of the hydroxyl-methyl intermediates, which is due to water competitive adsorption [106].

To probe the mechanism of CH<sub>4</sub> combustion over the 3DOM-structured metal-oxide-supported bimetallic NPs, methane temperature-programmed desorption (CH<sub>4</sub>-TPD) and in situ reflectance Fourier transform infrared spectroscopic (in situ DRIFTS) experiments were intensively carried out by Dai's group. The Au-Pd-*x*CoO/3DOM Co<sub>3</sub>O<sub>4</sub> sample (Figure 11) retained an excellent sustainable catalytic performance by doping an appropriate amount of CoO [26]. The cobalt was present in the form of a CoO phase, and the PdO-CoO interface was generated in the supported Au-Pd sample. Au-Pd-0.4CoO/3DOM Co<sub>3</sub>O<sub>4</sub> showed the highest methane oxidation activity ( $T_{50\%} = 312$  °C and  $T_{90\%} = 341$  °C at SV = 20,000 mL/(g h)) with the highest TOF<sub>Pd</sub> ( $11.8 \times 10^{-3}$  s<sup>-1</sup>) and the highest specific reaction rate (110.5 μmol/(g<sub>Pd</sub> s)) at 280 °C, which was a result due to formation of the unique PdO-CoO interface in the supported noble metal catalyst that was beneficial for CH<sub>4</sub> activation and O<sub>ads</sub> species concentration enhancement. The CoO inclusion significantly favored the generation of Pd<sup>2+</sup> species and facilitated the inhibition of hydroxyl formation, greatly improving moisture tolerance. The CH<sub>4</sub>-TPD profile displayed a lower methane desorption temperature (345 °C) on the CoO surface in Au-Pd-*x*CoO/3DOM Co<sub>3</sub>O<sub>4</sub>, which could be owing to the strong interaction between PdO and CoO and enhanced O<sub>ads</sub> species concentration. Methane could be activated flexibly on the PdO surface in Au-Pd-*x*CoO/3DOM Co<sub>3</sub>O<sub>4</sub>, and the adsorbed methane reacted with the O<sub>ads</sub> species to form CO<sub>2</sub> and H<sub>2</sub>O. Methane oxidation species generated over the Au-Pd-3.61CoO/3DOM Co<sub>3</sub>O<sub>4</sub> sample were detected by the in-situ DRIFTS experiments using an O<sub>2</sub>/CH<sub>4</sub> (molar ratio = 4) gas mixture. The obtained intermediate products, such as the H<sub>2</sub>O, CH<sub>4</sub>, CO<sub>2</sub>, CH<sub>3</sub><sup>-</sup>, H<sub>2</sub>CO, HCOO<sup>-</sup>, and CH<sub>2</sub>OH<sup>-</sup> species, further demonstrated that CoO was the active site for methane adsorption and activation. In addition, Co was doped into Pd/3DOM CeO<sub>2</sub> to generate a high O<sub>ads</sub> or CH<sub>4</sub> concentration and display good thermal stability [27]. Co was oxidized into CoO<sub>*x*</sub> easily at 340–450 °C, which gave rise to the enhanced methane oxidation performance, and PdCo<sub>*x*</sub> exhibited a better thermal stability than Pd or Co. The Co<sub>3.5</sub>Pd/3DOM CeO<sub>2</sub> sample exhibited the best methane combustion activity ( $T_{50\%} = 430$  °C and  $T_{90\%} = 480$  °C at SV = 40,000 mL/(g h)) with the lowest  $E_a$  (58 kJ/mol), the highest specific reaction rate ( $1334.3 \times 10^{-6}$  mol/(g<sub>Pd</sub> s)), and the highest TOF<sub>Co</sub> (0.04 s<sup>-1</sup>).

Similarly, it was reported that the addition of gold to AuPd/3DOM La<sub>0.6</sub>Sr<sub>0.4</sub>MnO<sub>3</sub> accelerated the methane oxidation rate [49]. The in-situ DRIFTS absorption bands of Pd/3DOM La<sub>0.6</sub>Sr<sub>0.4</sub>MnO<sub>3</sub> could be separated into three significant spectral zones, which led to a more efficient methane combustion mechanism to facilitate complete oxidation. The first-zone absorption bands were attributed to gas-phase CH<sub>4</sub> and CH<sub>3</sub><sup>-</sup>. The antisymmetric stretching vibration at 3014 cm<sup>-1</sup> and the deformation vibration at 1300 cm<sup>-1</sup> of the C–H bonds were ascribed to the CH<sub>4</sub> molecule, while the absorption band at 1450 cm<sup>-1</sup> belonged to the asymmetric stretching of C–H in CH<sub>3</sub><sup>-</sup>. The second-zone absorption

bands were attributed to gas-phase  $\text{CO}_2$  with the absorption bands at 2330 and 2360  $\text{cm}^{-1}$  due to the C=O stretching vibration. The third-zone absorption bands were related to the other byproduct species. The bands at 1060 and 1155  $\text{cm}^{-1}$  were ascribed to the O–O stretching vibration of the  $\text{O}_2^-$  species, while the ones at 1250 and 1415  $\text{cm}^{-1}$  represented the stretching vibration of C–H in formaldehyde. The strong C–O asymmetric stretching vibration at 1550 and 1690  $\text{cm}^{-1}$  as well as the C=O stretching vibration at 1840  $\text{cm}^{-1}$  were associated with the formate species. A new bidentate carbonate species appeared at 1170  $\text{cm}^{-1}$  for the AuPd/3DOM  $\text{La}_{0.6}\text{Sr}_{0.4}\text{MnO}_3$  catalyst, instead of stretching vibration (at 1250 and 1415  $\text{cm}^{-1}$ ) of C–H in formaldehyde ( $\text{H}_2\text{CO}$ ) for the Pd/3DOM  $\text{La}_{0.6}\text{Sr}_{0.4}\text{MnO}_3$  catalyst. The reaction rate was determined by the activation of C–H bond. The C–H bonds at 1300  $\text{cm}^{-1}$  appeared at 200 and 300 °C over AuPd (or Pd)/3DOM  $\text{La}_{0.6}\text{Sr}_{0.4}\text{MnO}_3$ , which revealed that the doping of Au gave rise to the lower  $\text{CH}_4$  activation temperature and higher methane oxidation activity. The methane oxidation mechanism over AuPd/3DOM  $\text{La}_{0.6}\text{Sr}_{0.4}\text{MnO}_3$  can be summarized as two separate sequences of elementary steps based on the in-situ DRIFTS results: The  $\text{O}_2$  is activated by the involved transferred electrons to form  $\text{O}_{\text{ads}}$  species on the more electronegative surface caused by Au doping, thus the formed  $\text{O}_{\text{ads}}$  species cause the C–H bonds in  $\text{CH}_4$  to dehydrogenate into  $\text{CH}_3^-$  and  $\text{OH}^-$ . The  $\text{CH}_3^-$  species is subsequently bonded to the unsaturated sites and dissociated into the  $\text{HCOO}^-$  species, or the  $\text{CH}_3^-$  species is further H-abstracted directly into the  $\text{H}^+$  and  $\text{HCOO}^-$  species (which explains the lack of the  $\text{CH}_2\text{O}$  species in the in-situ DRIFTS spectra over AuPd/3DOM  $\text{La}_{0.6}\text{Sr}_{0.4}\text{MnO}_3$  compared with those over Pd/3DOM  $\text{La}_{0.6}\text{Sr}_{0.4}\text{MnO}_3$ ). In addition, the above result indicated that the  $\text{CH}_3^-$  species could transfer freely and interact with the additional  $\text{O}_{\text{ads}}$  species more readily, leading to acceleration of the oxidation reaction. The  $\text{H}^+$  could combine with  $\text{O}_{\text{ads}}$  to generate  $\text{H}_2\text{O}$ , while  $\text{H}_2\text{CO}$  was first activated to form  $\text{HCOO}^-$  and then completely oxidized to  $\text{CO}_2$  and  $\text{H}_2\text{O}$ .

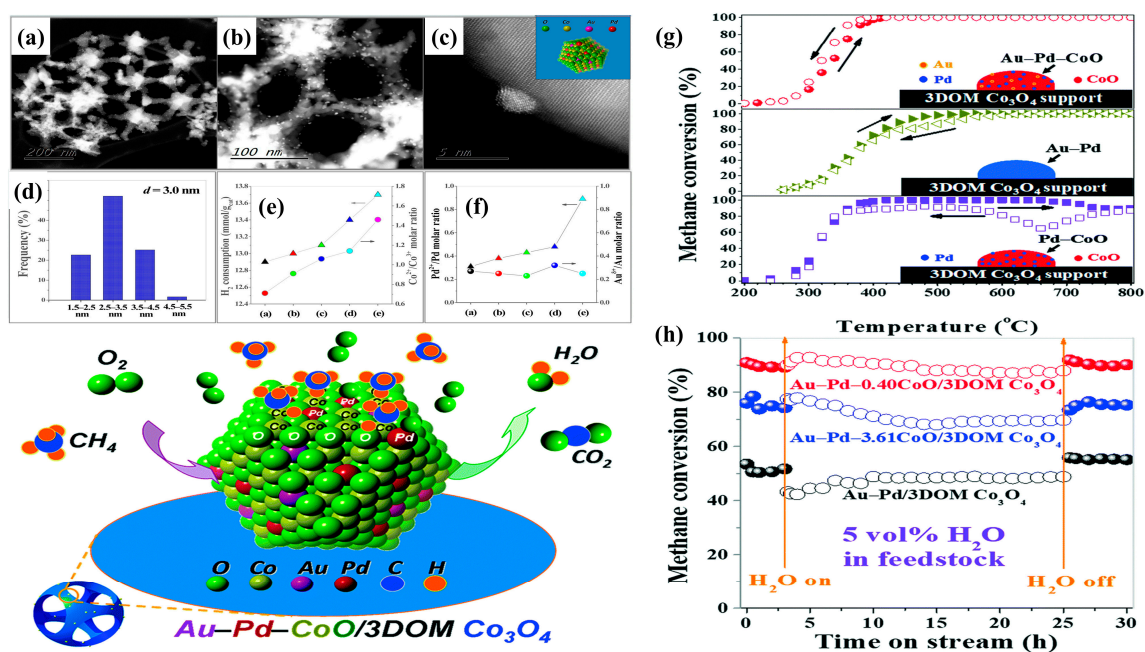


**Figure 11.** (a–c) HADDF-STEM images and (d) particle size distribution of Au-Pd-3.61CoO/3DOM  $\text{Co}_3\text{O}_4$ ; (e) hydrogen consumption and  $\text{Co}^{2+}/\text{Co}^{3+}$  molar ratio; (f)  $\text{Pd}^{2+}/\text{Pd}$  and  $\text{Au}^{\delta+}/\text{Au}$  molar ratios of (a) Au-Pd/3DOM  $\text{Co}_3\text{O}_4$ , (b) Au-Pd-0.19CoO/3DOM  $\text{Co}_3\text{O}_4$ , (c) Au-Pd-0.40CoO/3DOM  $\text{Co}_3\text{O}_4$ , (d) Au-Pd-0.90CoO/3DOM  $\text{Co}_3\text{O}_4$ , and (e) Au-Pd-3.61CoO/3DOM  $\text{Co}_3\text{O}_4$ ; (g) methane conversion; (h) methane conversion as a function of reaction time in the presence of 5.0 vol% water vapor in the feedstock over the samples at 340 °C. Reprinted with permission from Ref. [26]. Copyright 2017, copyright American Chemical Society.

### 3.4. Effects of H<sub>2</sub>O and SO<sub>2</sub> on Methane Combustion

H<sub>2</sub>O poisoning was a significant challenge for the supported noble metal materials in methane combustion at low temperatures. Bokhoven's group investigated the electronic states of palladium (Figure 12) and the effect of water co-dosing on CH<sub>4</sub> combustion using the ambient-pressure X-ray photoelectron spectroscopic (APXPS) technique [107]. The evolution of metallic palladium (Pd<sup>0</sup> at binding energy (BE) = 334.95 eV), surface palladium oxide (PdO<sub>x</sub> at BE = 335.6 eV), and bulk palladium oxide (PdO at BE = 336.7 eV) was studied in a gas mixture of CH<sub>4</sub>/O<sub>2</sub> with different ratios and the water coexisting case at 50–600 °C. The Pd<sup>0</sup> species was detected in the initial stage at 50 °C. The fraction of the surface PdO<sub>x</sub> species reached the maximal value at a certain temperature of 100–200 °C for the CH<sub>4</sub>/O<sub>2</sub> mixture and prolonged to 300 °C both in the pure O<sub>2</sub> and H<sub>2</sub>O co-feeding cases. The PdO species appeared in the absence of water at 250 °C, and was completely reduced to the Pd<sup>0</sup> species when the temperature reached 550 or 600 °C. However, the peak corresponding to the PdO species appeared in the presence of H<sub>2</sub>O only at 350 °C, and no quantitative reduction of PdO<sub>x</sub> happened, even at 600 °C. It was concluded that water inhibited the conversion of methane by converting the PdO<sub>x</sub> species to the Pd–OH species. Palladium hydroxyls blocked the coordinatively unsaturated Pd sites (Pd<sub>CUS</sub>) for methane adsorption and the adjacent oxidized sites (Pd–O) for the activation of methane to intermediates, instead of forming hydroxyl groups. Water was adsorbed at the surface oxygen vacancies and deprotonated to form a second hydroxyl at a neighboring Pd–O site; thus, water accumulation dramatically hindered the adsorption and migration of O<sub>2</sub> to restrict regeneration of the active sites as well as to suppress formation of the active PdO phase.

Dai and coworkers [108] fabricated the water-resistant catalysts for CH<sub>4</sub> low-temperature combustion using the stepwise strategy to generate the atomically dispersed tungsten species with tailored local coordination structures and electronic states at the catalytically active sites on Pd NPs (Figures 13 and 14). The Pd–O–W-like nanocomposite formed on the PdO surface with an atomic scale interface was responsible for the outstanding catalytic activity. The water adsorption energy decreased from 1.23 eV (at the Pd site on PdO) to 0.83 eV (at the Pd site on Pd–O–W), indicating a valid inhibition of water adsorption on the supported PdW sample, which effectively mitigated lattice oxygen deactivation obviously in the presence of H<sub>2</sub>O. Moreover, the oxygen adsorption energy downgraded from 1.12 eV (at the Pd site on PdO) to 1.99 eV (at the Pd site on Pd–O–W), further confirming a larger oxygen adsorption capacity of the supported PdW catalyst for excellent catalytic performance. The supported catalyst preferred a better resistance to water poisoning than the conventional catalysts for CH<sub>4</sub> oxidation via a hydroperoxyl-promoted species and a novel coexistence reaction mechanism of Mars van–Krevelen and Langmuir–Hinshelwood models over the catalyst in the presence of moisture. DFT calculations revealed that the upshift of the *d*-band center of palladium caused by the electron transfer from the atomically dispersed tungsten in the supported PdW sample was expected to enhance the oxygen adsorption and activation ability, which was associated with superior methane combustion activity and excellent water tolerance.

Cargnello and coworkers [109] developed an in situ water sorption strategy to remove the water formed during the process of CH<sub>4</sub> oxidation using zeolite, alumina, or CaO as a water sorbent (Figure 15). The doping of zeolite or Al<sub>2</sub>O<sub>3</sub> to the supported Pd catalyst could transiently decrease H<sub>2</sub>O concentration in a limited amount, thus leading to enhancement in activity below 300 °C. The hydroxylation of PdO happened quickly due to the limited number of sorption sites on zeolite or Al<sub>2</sub>O<sub>3</sub>, resulting in a poor activity of the Pd catalyst. On the contrary, the Pd catalyst diluted with a stronger CaO exhibited a sixfold improvement transient activity, which maintained a 10 h on-stream reaction compared with the sorbent-free sample. A thermodynamic model and detailed Gibbs free energy calculations were established to further prove the water durability of CaO. Although Gibbs free energy of water sorption on CaO was –21 kJ/mol with a sufficient number of sites, it was higher than that (–38.5 kJ/mol) of H<sub>2</sub>O adsorption on PdO at 300 °C. The number of

the adsorptive sites was equal to that on CaO, which was  $3.6 \times 10^4$  times more than that of the PdO sites, and the complete water sorption at the CaO sites could still be achieved due to the large number of the adsorptive sites. Based on the above results, mechanistic analysis declared that the water sorption efficiency was influenced by both sorption energy and number of the adsorptive sites.

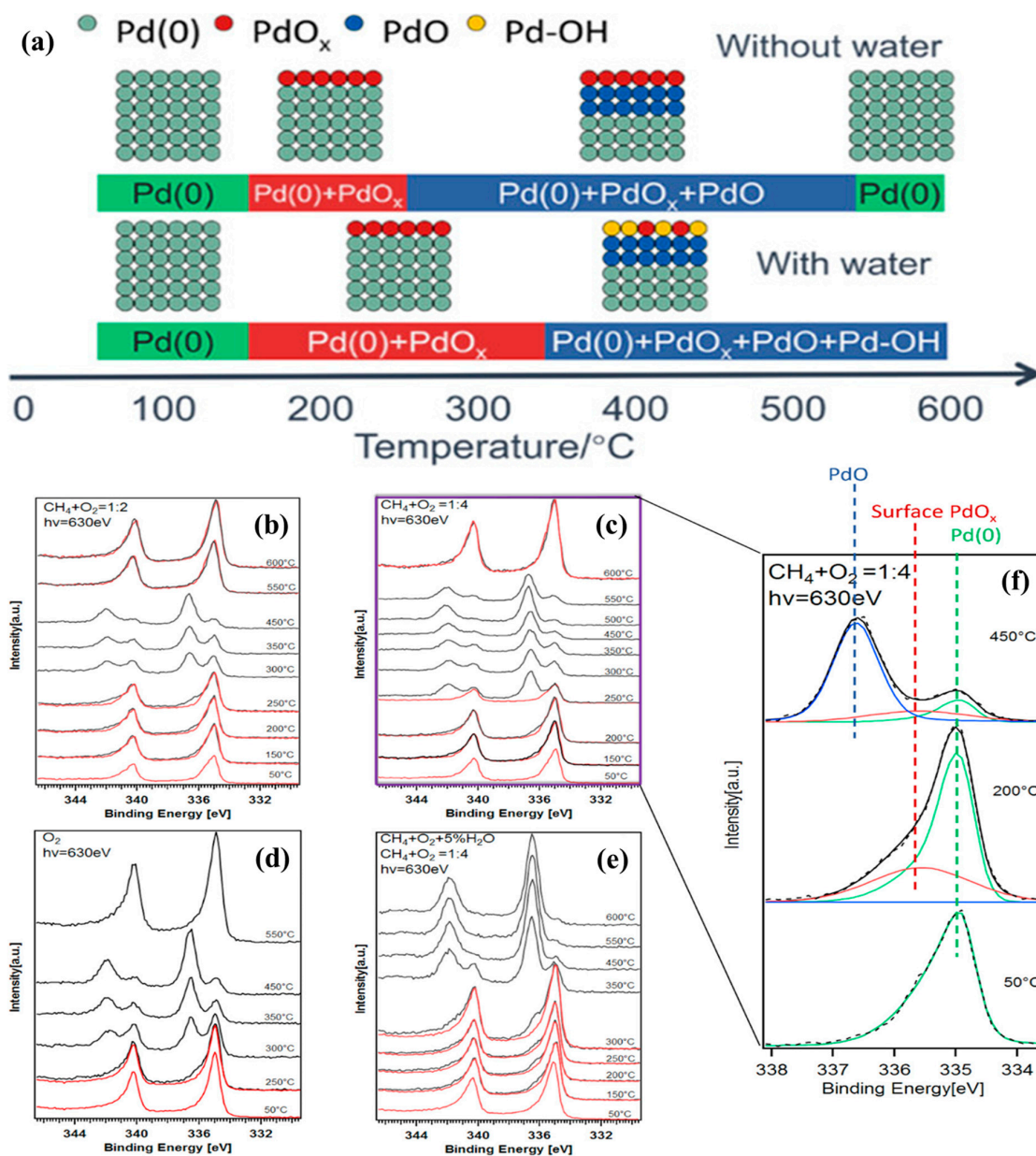


**Figure 12.** (a) The formation process and role of water on the structure of palladium catalyst. Steady-state Pd 3d photoemission spectra in gas atmosphere of (b) CH<sub>4</sub> + O<sub>2</sub> = 1:2, (c) CH<sub>4</sub> + O<sub>2</sub> = 1:4, (d) O<sub>2</sub> only, (e) CH<sub>4</sub> + O<sub>2</sub> + 5 vol% H<sub>2</sub>O (CH<sub>4</sub> + O<sub>2</sub> = 1:4) at different temperatures; and (f) deconvolution of Pd 3d<sub>5/2</sub> spectra. Reprinted with permission from Ref. [107]. Copyright 2020, copyright American Chemical Society.

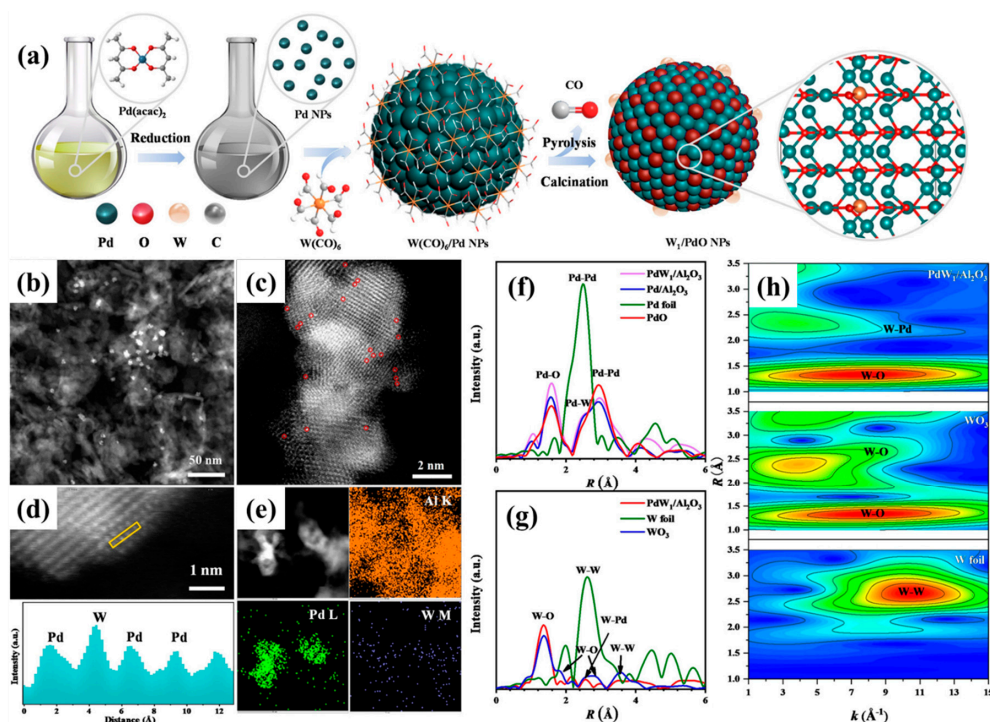


**Figure 13.** (a) Illustration of the preparation process of PdW<sub>1</sub>/Al<sub>2</sub>O<sub>3</sub>, HAADF-STEM images, and particle-size distributions (insets) of (b) PdW<sub>1</sub>/Al<sub>2</sub>O<sub>3</sub>; (c,d) aberration-corrected HAADF-STEM images and (e) EDX elemental mappings of PdW<sub>1</sub>/Al<sub>2</sub>O<sub>3</sub>. The Fourier transforms of the experimental EXAFS spectra of the as-obtained samples at the (f) Pd K-edge and (g) W L<sub>3</sub>-edge; (h) wavelet transform plots of PdW<sub>1</sub>/Al<sub>2</sub>O<sub>3</sub>, WO<sub>3</sub>, and W foil. Reprinted with permission from Ref. [108]. Copyright 2022, copyright John Wiley and Sons.

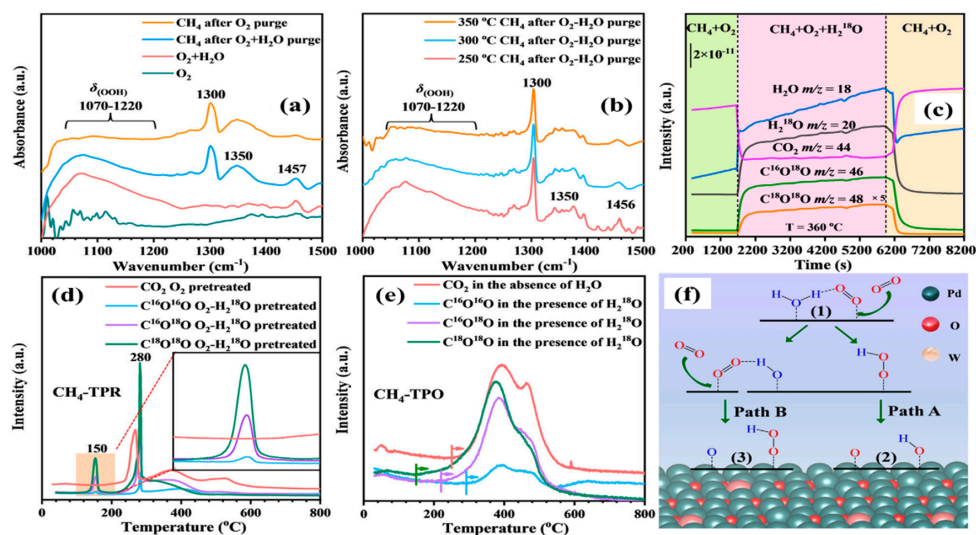


**Figure 14.** In situ DRIFTS spectra over PdW<sub>1</sub>/Al<sub>2</sub>O<sub>3</sub> (a) under different gas conditions at 250 °C and (b) at different temperatures under CH<sub>4</sub> after H<sub>2</sub>O-O<sub>2</sub> purge; (c) products profiles of CH<sub>4</sub>-TPSR over PdW<sub>1</sub>/Al<sub>2</sub>O<sub>3</sub> at 360 °C in the experiment of isotopic water introduction and cut-off with a reaction gas feed; (d) CO<sub>2</sub> profiles in CH<sub>4</sub>-TPR isotopic trace experiment over PdW<sub>1</sub>/Al<sub>2</sub>O<sub>3</sub> after O<sub>2</sub> or O<sub>2</sub>-H<sub>2</sub><sup>18</sup>O pretreatment; (e) CO<sub>2</sub> profiles in CH<sub>4</sub>-TPO isotopic trace experiment; and (f) reaction scheme for O<sub>2</sub> activation in the presence of H<sub>2</sub>O (the blue color means the element from H<sub>2</sub>O, whereas the red color means the element from oxygen). Reprinted with permission from Ref. [108]. Copyright 2022, copyright John Wiley and Sons.

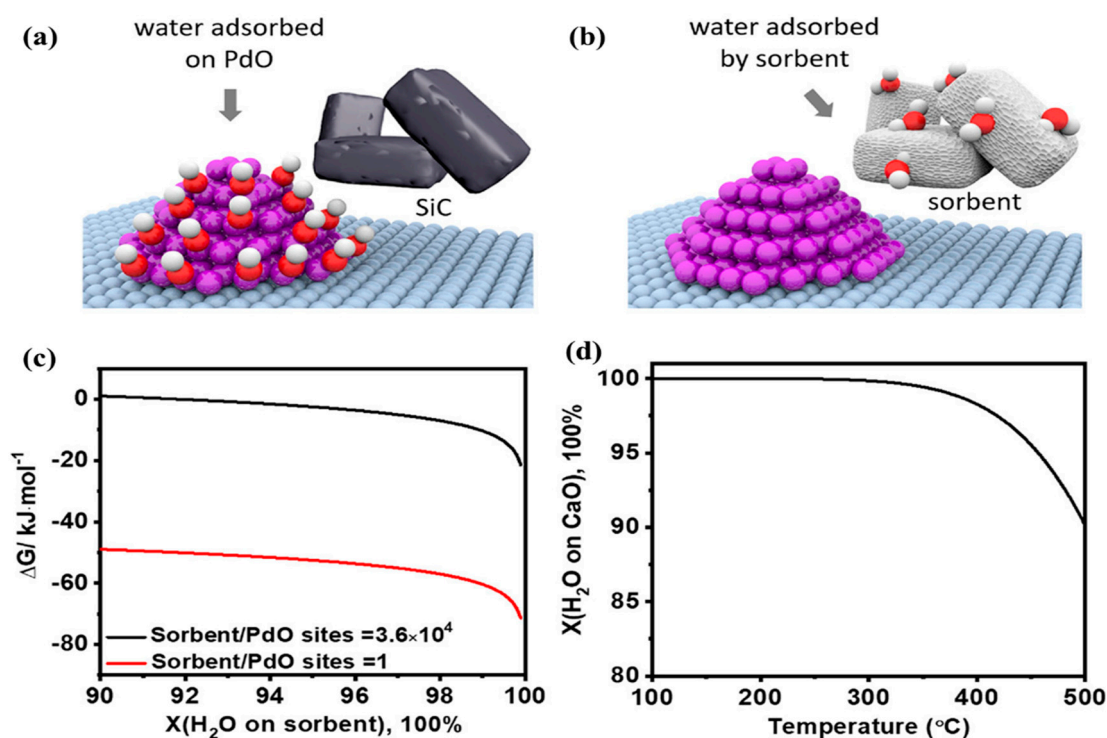


**Figure 15.** Schematic of sorption on either PdO or sorbent surface depending on the conditions: (a) reaction with SiC as an inert diluent where the activity slows as water produced adsorbs on PdO surfaces at high coverage and (b) one with a water sorbent where methane combustion occurs on active PdO surfaces with low water coverage; (c) required Gibbs free energy change of water sorption on a sorbent as a function of the percentage of water adsorbed by the sorbent; (d) fraction of water absorbed on CaO as a function of temperature. Reprinted with permission from Ref. [109]. Copyright 2020, copyright American Chemical Society.

In actuality, most of the catalysts are unavoidably poisoned by a trace amount of  $\text{SO}_2$  or accumulated sulfur under actual reaction conditions, which, hence, impairs the overall catalytic efficiency of the after-treatment system. In essence, the interaction between  $\text{SO}_2$  and supported noble metal catalysts is a heterogeneous reaction of  $\text{SO}_2$  with the active site or support, in which rich  $-\text{OH}$  groups, active oxygen species, and defects on the catalyst surface provide the necessary sites for  $\text{SO}_2$  adsorption and transformation [110]. Suvanto et al. studied the thin  $\text{PdSO}_4$  films formed on the Pd–Pt/ $\text{Al}_2\text{O}_3$  catalyst surface using the DFT calculations, and found that  $\text{PdSO}_4(110)$  and  $\text{PdSO}_4(111)$  which corresponded to  $\text{PdO}(100)$  and  $\text{PdO}(101)$  were the most possible poisoned index surface [111]. The first C–H dissociation of  $\text{CH}_4$  on  $\text{PdSO}_4(111)$ , which contained the coordinatively unsaturated palladium, was a favorable option, with an energy barrier of 0.74–0.87 eV similar to that of the metallic  $\text{Pd}^0$  reported before (Figure 16). Moderate activation energies offered reasonable understanding of appropriate methane conversions over  $\text{PdSO}_4$  under the dry conditions. Unfortunately, the presence of  $-\text{OH}$  groups was found to enhance the C–H dissociation barrier to terminal oxygen by 0.2 eV compared with the hydroxyl-free surface. Furthermore, water adsorption on  $\text{PdSO}_4(111)$  with an energy of  $-1.45$  eV ( $-140$  kJ/mol) was significantly stronger than that on  $\text{PdO}(101)$  with an energy of  $-0.82$  eV ( $-79$  kJ/mol), which occupied dominant competitive adsorption to bring about site blocking. The  $-\text{OH}$  groups weakened the adsorption on  $\text{PdSO}_4(111)$ , while strong adsorption energy of the  $-\text{OH}$  groups was thermodynamically favorable for forming adsorbed molecular water on the catalyst surface. The presence of surface  $-\text{OH}$  groups was responsible for the increased C–H dissociation barrier, strong  $\text{H}_2\text{O}$  adsorption, and associated site blockage, which revealed the observation that the  $\text{PdSO}_4/\text{Al}_2\text{O}_3$  sample poisoned by  $\text{SO}_2$  under the humid conditions showed low methane conversions. Noble-metal-based materials with

SO<sub>2</sub> intoxication gave rise to the surface sulfur deposition with the decreased methane oxidation activity. Moreover, the SO<sub>2</sub>-poisoned catalysts facilitated rearrangement of the crystal structure and modified electronic properties of the noble metals.

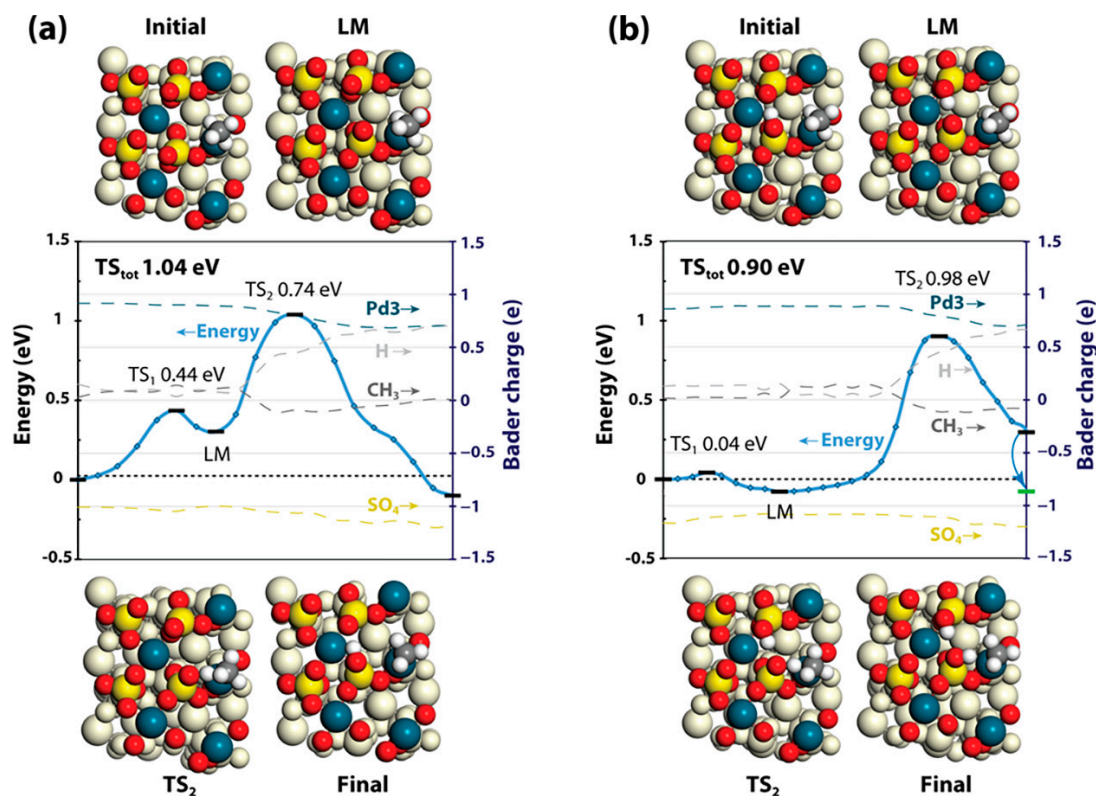


**Figure 16.** Energy profiles (solid line) predicted by the NEB and the associated Bader charges (dashed lines) for dissociation of methane to the S<sub>2</sub> position on (a) a clean PdSO<sub>4</sub>(111) surface and (b) a hydroxylated PdSO<sub>4</sub>(111) surface. The black bars on the energy curve denote minimum and TS structures, whereas small diamonds denote NEB images. The green bar in (b) denotes the energy of the final structure with reoriented hydroxyl groups. Negative Bader charge corresponds to an excess of electrons relative to isolated atoms, whereas positive Bader charge corresponds to the deficiency of electrons. Reprinted with permission from Ref. [110]. Copyright 2020, copyright American Chemical Society.

Previous investigation results indicated that SO<sub>2</sub> adsorption induced recrystallization of the Pt(111) facet to the Pt(100) facet via surface diffusion driven by the decreased surface free energy of Pt/Al<sub>2</sub>O<sub>3</sub> [112,113]. In particular, the SO<sub>2</sub>-poisoning effect was intensively investigated on the reactions (e.g., ring opening of methyl cyclopentane, hydrogenolysis, and isomerization) which were sensitive to surface structures of the catalysts as well as sulfur poisoning [112]. The sulfur species possessing an electronegative character could decrease electronic density of the Pt clusters, thus suppressing the adsorption ability of Pt toward the other adsorbates [114]. Recently, Peng et al. [97] developed an efficient strategy to synthesize the Pd–Ce nanowire-like catalysts with the good SO<sub>2</sub> tolerance in CH<sub>4</sub> combustion using the enhanced metal oxide interaction and core–shell confinement methods (Figures 17 and 18). The as-prepared Pd–CeNW@SiO<sub>2</sub> sample exhibited complete CH<sub>4</sub> combustion within 10 h of on-stream reaction in the simultaneous presence of sulfur dioxide and moisture at 450 °C. In situ DRIFTS spectra of SO<sub>2</sub> adsorption displayed featured bands at 1255 and 1110 cm<sup>−1</sup> assignable to PdSO<sub>4</sub>, which was considered to be the culprit for deactivation of the Pd-based catalysts. Fortunately, the porous shell structure of Pd–CeNW@SiO<sub>2</sub> exerted a shielding effect of SO<sub>2</sub> poisoning and a protection role for CeO<sub>2</sub> on Pd, which accounted for the excellent SO<sub>2</sub> tolerance.

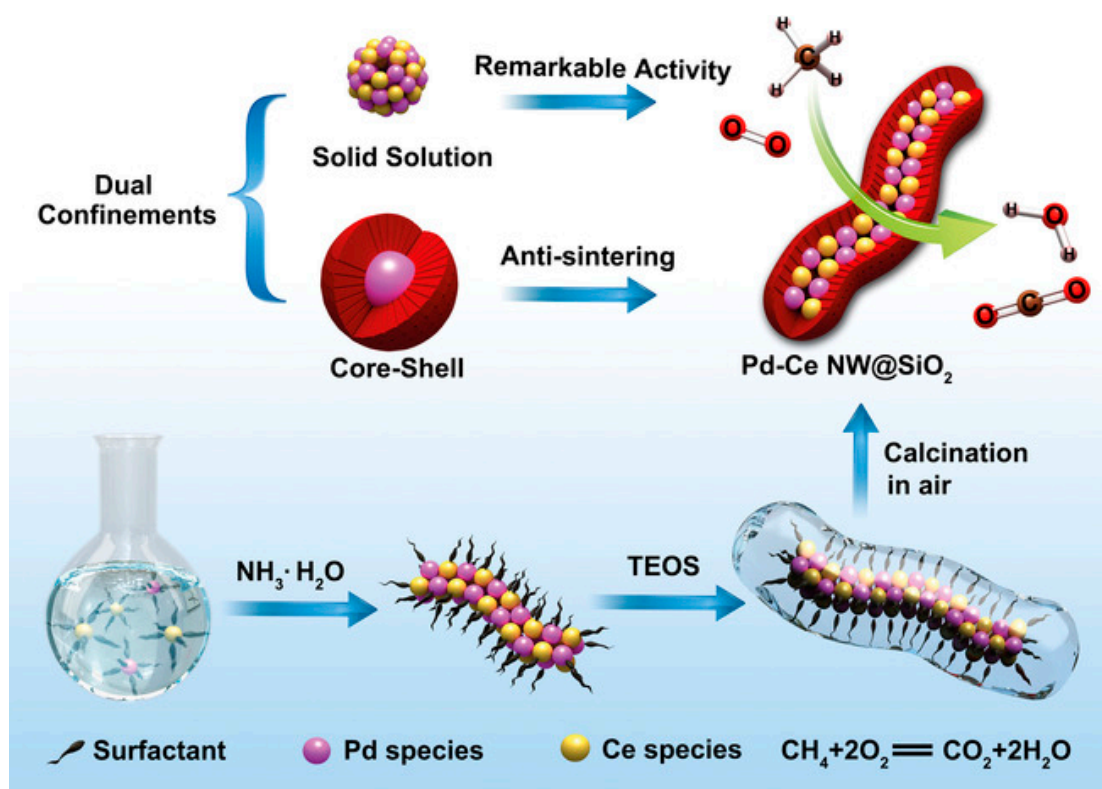


Figure 17. The formation process and catalytic application of Pd-CeNW@SiO<sub>2</sub>. Reprinted with permission from Ref. [97]. Copyright 2022, copyright John Wiley and Sons.

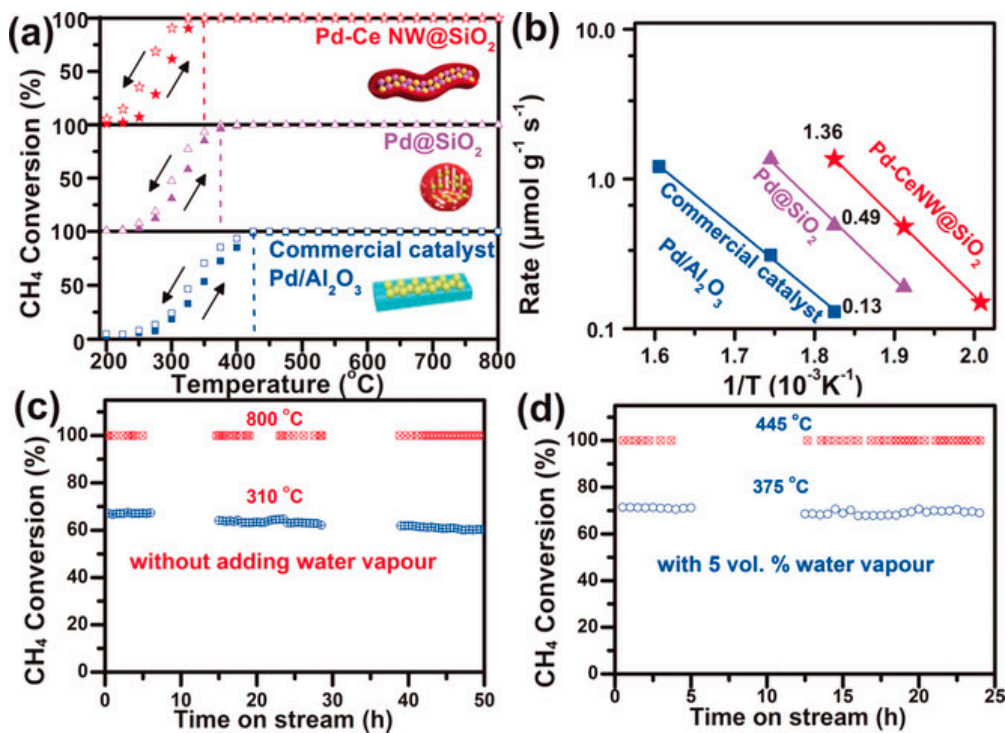


Figure 18. (a) Heating and cooling (5 °C/min) light-off curves of CH<sub>4</sub> conversion against temperature for Pd-CeNW@SiO<sub>2</sub> (1.5 wt% Pd), Pd@SiO<sub>2</sub> (1.5 wt% Pd), and a commercial Pd/Al<sub>2</sub>O<sub>3</sub> catalyst (2.0 wt% Pd); (b) Arrhenius plots, (c) high-temperature stability, and (d) water resistance of Pd-CeNW@SiO<sub>2</sub>. Conditions: 1 vol% CH<sub>4</sub>, 21 vol% O<sub>2</sub>, balanced with N<sub>2</sub>, WHSV = 36,000 mL/(g<sub>cat</sub> h). Reprinted with permission from Ref. [97]. Copyright 2022, copyright John Wiley and Sons.

#### 4. Conclusions and Perspectives

Well-ordered and developed 3D porous single- or mixed-metal oxides with intrinsic activity could disperse and stabilize the active transition-metal oxide or noble metal phases, thus exhibiting excellent methane combustion performance. Numerous studies on preparation, characterization, and methane oxidation activity, as well as promoted low-temperature oxidation activity, sintering resistance, and steam and SO<sub>2</sub> tolerance of the supported transition-metal oxide or noble metal catalysts were briefly summarized. Supported transition-metal oxide or noble metal catalysts with well-ordered 3D porous structures were successfully synthesized via the surfactant-assisted hard template and reduction routes to realize ultrahigh component dispersion and increased active sites. Partial substitution of the mixed oxides by heterovalent cations is considered to be a favorable strategy to tailor-make the coordination structures and surface electronic states to realize excellent redox ability, oxygen mobility, high surface reactivity, and good hydrothermal stability. The competitive adsorption of water and reactants on the catalyst surface and the promoted methane oxidation activity in the presence of a trace amount of moisture were discussed in detail. The combined use of DFT calculations and advanced in situ characterization techniques provided deep insights into understanding the reaction and SO<sub>2</sub> poisoning mechanisms. Herein, novel strategies were developed to generate specific materials with better SO<sub>2</sub> and moisture tolerance for successful methane oxidation applications. However, thermal stability and antipoisoning ability of the catalysts remain a big challenge. Therefore, the strong interaction between transition-metal oxide or noble metal and support should be further studied by establishing the fundamental kinetics models to realize more controllably efficient catalysts, so that these materials can be commercialized for industrial utilization.

The biggest challenge for commercial application of noble metals catalysts is deactivation caused by agglomeration and sintering at high temperatures. Supports with high surface areas, well-ordered pore structures, and narrow pore-size distributions provide a large number of catalytic active sites and favor stabilization of noble metal NPs. Noble metal NPs are anchored on the porous skeleton with regular arrangements to improve the dispersion of the active centers, and reduce the exposure extent to obtain high resistance to carbon deposition and sulfur dioxide tolerance. The pore structure can give rise to a large active surface area and better structure stability of active components to increase possibility of the interaction between reactants and active sites. This review provides a theoretical support for the design and synthesis of high-thermal-stability catalysts. Noble metals supported on ordered porous oxides would be the suitable catalysts for the commercial and industrial applications of methane combustion.

Complete CH<sub>4</sub> combustion plays a particular functional promoter role to achieve carbon neutrality via using natural gas as fuel. It offers potential and possibility for optimizing the use of methane resources for the researchers working on catalysis and materials science, and presents a new opportunity to develop the supported transition-metal oxide or noble metal catalytic materials with high performance, unique nanoporous configurations, and multifunctional components.

**Author Contributions:** Conceptualization, H.D.; Methodology, H.D.; Software, Y.L., J.D. and L.J.; Investigation, H.L.; Resources, H.D.; Data Curation, H.L.; Writing—Original Draft Preparation, H.L.; Writing—Review and Editing, H.D.; Visualization, Y.L., J.D. and L.J.; Supervision, H.D.; Project Administration, H.D.; Funding Acquisition, H.D. All authors have read and agreed to the published version of the manuscript.

**Funding:** This work was supported by the State's Key Project of Research and Development Plan (2022YFB3504101), National Natural Science Foundation Committee of China—Liaoning Provincial People's Government Joint Fund (U1908204), and Foundation on the Creative Research Team Construction Promotion Project of Beijing Municipal Institutions (IDHT20190503).

**Institutional Review Board Statement:** Not applicable.

**Informed Consent Statement:** Not applicable.

**Data Availability Statement:** All the relevant data used in this study have been provided in the form of figures and tables in the published article, and all data provided in the present manuscript are available to whom they may concern.

**Conflicts of Interest:** The authors declare no conflict of interest.

## References

1. Pfefferle, L.D.; Pfefferle, W.C. Catalysis in combustion. *Catal. Rev.* **1987**, *29*, 219–267. [[CrossRef](#)]
2. Wei, L.; Wang, Z.W.; Liu, Y.X.; Guo, G.S.; Dai, H.X.; Cui, S.P.; Deng, J.G. Support promotion effect on the SO<sub>2</sub> and K<sup>+</sup> co-poisoning resistance of MnO<sub>2</sub>/TiO<sub>2</sub> for NH<sub>3</sub>-SCR of NO. *J. Hazard. Mater.* **2021**, *416*, 126117. [[CrossRef](#)] [[PubMed](#)]
3. Gremminger, A.T.; Pereira de Carvalho, H.W.; Popescu, R.; Grunwaldt, J.-D.; Deutschmann, O. Influence of gas composition on activity and durability of bimetallic Pd-Pt/Al<sub>2</sub>O<sub>3</sub> catalysts for total oxidation of methane. *Catal. Today* **2015**, *258*, 470–480. [[CrossRef](#)]
4. Öcal, M.; Oukaci, R.; Marcelin, G.; Jang, B.W.-L.; Spivey, J.J. Steady-state isotopic transient kinetic analysis on Pd-supported hexaaluminates used for methane combustion in the presence and absence of NO. *Catal. Today* **2000**, *59*, 205–217. [[CrossRef](#)]
5. Raza, J.; Khoja, A.H.; Anwar, M.; Saleem, F.; Naqvi, S.R.; Liaquat, R.; Hassan, M.; Javaid, R.; Qazi, U.Y.; Lumbers, B. Methane decomposition for hydrogen production: A comprehensive review on catalyst selection and reactor systems. *Renew. Sust. Energ. Rev.* **2022**, *168*, 112774. [[CrossRef](#)]
6. Wang, Y.G.; Ren, J.W.; Wang, Y.Q.; Zhang, F.Y.; Liu, X.H.; Guo, Y.; Lu, G.Z. Nanocasted synthesis of mesoporous LaCoO<sub>3</sub> perovskite with extremely high surface area and excellent activity in methane combustion. *J. Phys. Chem. C* **2008**, *112*, 15293–15298. [[CrossRef](#)]
7. Chen, J.H.; Arandiyán, H.; Gao, X.; Li, J.H. Recent advances in catalysts for methane combustion. *Catal. Surv. Asia* **2015**, *19*, 140–171. [[CrossRef](#)]
8. Tang, X.F.; Li, J.H.; Hao, J.M. Synthesis and characterization of spinel Co<sub>3</sub>O<sub>4</sub> octahedra enclosed by the {111} facets. *Mater. Res. Bull.* **2008**, *43*, 2912–2918. [[CrossRef](#)]
9. Li, J.H.; Liang, X.; Xu, S.C.; Hao, J.M. Catalytic performance of manganese cobalt oxides on methane combustion at low temperature. *Appl. Catal. B* **2009**, *90*, 307–312. [[CrossRef](#)]
10. Chen, J.H.; Zhang, X.Y.; Arandiyán, H.; Peng, Y.; Chang, H.Z.; Li, J.H. Low temperature complete combustion of methane over cobalt chromium oxides catalysts. *Catal. Today* **2013**, *201*, 12–18. [[CrossRef](#)]
11. Zhu, Y.F.; Tan, R.Q.; Feng, J.; Ji, S.S.; Cao, L.L. The reaction and poisoning mechanism of SO<sub>2</sub> and perovskite LaCoO<sub>3</sub> film model catalysts. *Appl. Catal. A* **2001**, *209*, 71–77. [[CrossRef](#)]
12. Huang, H.F.; Sun, Z.; Lu, H.F.; Shen, L.Q.; Chen, Y.F. Study on the poisoning tolerance and stability of perovskite catalysts for catalytic combustion of volatile organic compounds. *React. Kinet. Mechan. Catal.* **2010**, *101*, 417–427. [[CrossRef](#)]
13. Cheng, J.; Wang, H.L.; Hao, Z.P.; Wang, S.B. Catalytic combustion of methane over cobalt doped lanthanum stannate pyrochlore oxide. *Catal. Commun.* **2008**, *9*, 690–695. [[CrossRef](#)]
14. Cheng, J.; Li, J.J.; Ma, C.Y.; Hao, Z.P. Catalytic combustion of methane over La<sub>2</sub>TM<sub>0.3</sub>Zr<sub>1.7</sub>O<sub>7-δ</sub> (TM = Mn, Fe, and Co) pyrochlore oxides. *Catal. Commun.* **2009**, *10*, 1170–1173. [[CrossRef](#)]
15. Aitbekova, A.; Zhou, C.; Stone, M.L.; Lezama-Pacheco, J.S.; Yang, A.-C.; Hoffman, A.S.; Goodman, E.D.; Huber, P.; Stebbins, J.F.; Bustillo, K.C.; et al. Templated encapsulation of platinum-based catalysts promotes high-temperature stability to 1100 °C. *Nat. Mater.* **2022**, *21*, 1290–1297. [[CrossRef](#)]
16. Bartley, J.K.; Dimitratos, N.; Edwards, J.K.; Kiely, C.J.; Taylor, S.H. A Career in catalysis: Graham J. Hutchings. *ACS Catal.* **2021**, *11*, 5916–5933. [[CrossRef](#)]
17. Agarwal, N.; Freakley, S.J.; McVicker, R.U.; Althahban, S.M.; Dimitratos, N.; He, Q.; Morgan, D.J.; Jenkins, R.L.; Willock, D.J.; Taylor, S.H.; et al. Aqueous Au-Pd colloids catalyze selective CH<sub>4</sub> oxidation to CH<sub>3</sub>OH with O<sub>2</sub> under mild conditions. *Science* **2017**, *358*, 223–227. [[CrossRef](#)]
18. Dai, H.X.; Hou, Z.Q.; Zhang, X.; Zhang, K.F. Catalytic performance of regularly morphological and porous catalysts for the oxidation of volatile organic compounds. *J. Beijing Univ. Technol.* **2019**, *45*, 1095–1114.
19. Dai, H.X.; Deng, J.G.; Xia, Y.S.; Zhang, R.Z.; Zhang, L. Hard-templating fabrication and catalytic applications of three-dimensionally ordered meso- and macroporous transition-metal oxides. *Inorg. Chem. Ind.* **2012**, *44*, 55–58.
20. Xu, P.; Zhang, X.; Zhao, X.T.; Yang, J.; Hou, Z.Q.; Bai, L.; Chang, H.Q.; Liu, Y.X.; Deng, J.G.; Guo, G.S.; et al. Preparation, characterization, and catalytic performance of PdPt/3DOM LaMnAl<sub>11</sub>O<sub>19</sub> for the combustion of methane. *Appl. Catal. A* **2018**, *562*, 284–293. [[CrossRef](#)]
21. Xia, Y.S.; Dai, H.X.; Jiang, H.Y.; Deng, J.G.; He, H.; Au, C.T. Mesoporous chromia with ordered three-dimensional structures for the complete oxidation of toluene and ethyl acetate. *Environ. Sci. Technol.* **2009**, *43*, 8355–8360. [[CrossRef](#)] [[PubMed](#)]
22. Xia, Y.S.; Dai, H.X.; Jiang, H.Y.; Zhang, L.; Deng, J.G.; Liu, Y.X. Three-dimensionally ordered and wormhole-like mesoporous iron oxide catalysts highly active for the oxidation of acetone and methanol. *J. Hazard. Mater.* **2011**, *186*, 84–91. [[CrossRef](#)] [[PubMed](#)]

23. Xia, Y.S.; Dai, H.X.; Jiang, H.Y.; Zhang, L. Three-dimensional ordered mesoporous cobalt oxides: Highly active catalysts for the oxidation of toluene and methanol. *Catal. Commun.* **2010**, *11*, 1171–1175. [[CrossRef](#)]
24. Deng, J.G.; Zhang, L.; Dai, H.X.; Xia, Y.S.; Jiang, H.Y.; Zhang, H.; He, H. Ultrasound-assisted nanocasting fabrication of ordered mesoporous MnO<sub>2</sub> and Co<sub>3</sub>O<sub>4</sub> with high surface areas and polycrystalline walls. *J. Phys. Chem. C* **2010**, *114*, 2694–2700. [[CrossRef](#)]
25. Xie, S.H.; Liu, Y.X.; Deng, J.G.; Zhao, X.T.; Yang, J.; Zhang, K.F.; Han, Z.; Arandiyani, H.; Dai, H.X. Effect of transition metal doping on the catalytic performance of Au–Pd/3DOM Mn<sub>2</sub>O<sub>3</sub> for the oxidation of methane and *o*-xylene. *Appl. Catal. B* **2017**, *206*, 221–232. [[CrossRef](#)]
26. Xie, S.H.; Liu, Y.X.; Deng, J.G.; Zang, S.M.; Zhang, Z.H.; Arandiyani, H.; Dai, H.X. Efficient removal of methane over cobalt-monoxide-doped AuPd nanocatalysts. *Environ. Sci. Technol.* **2017**, *51*, 2271–2279. [[CrossRef](#)]
27. Xie, S.H.; Liu, Y.X.; Deng, J.G.; Zhao, X.T.; Yang, J.; Zhang, K.F.; Han, Z.; Dai, H.X. Three-dimensionally ordered macroporous CeO<sub>2</sub>-supported Pd@Co nanoparticles: Highly active catalysts for methane oxidation. *J. Catal.* **2016**, *342*, 17–26. [[CrossRef](#)]
28. Wu, Z.X.; Deng, J.G.; Liu, Y.X.; Xie, S.H.; Jiang, Y.; Zhao, X.T.; Yang, J.; Arandiyani, H.; Guo, G.S.; Dai, H.X. Three-dimensionally ordered mesoporous Co<sub>3</sub>O<sub>4</sub>-supported Au–Pd alloy nanoparticles: High-performance catalysts for methane combustion. *J. Catal.* **2015**, *332*, 13–24. [[CrossRef](#)]
29. Zhao, X.T.; Liu, Y.X.; Deng, J.G.; Xu, P.; Yang, J.; Zhang, K.F.; Han, Z.; Dai, H.X. Mesoporous Pd<sub>x</sub>Pt alloys: High-performance catalysts for methane combustion. *Mol. Catal.* **2017**, *442*, 191–201. [[CrossRef](#)]
30. Ciuparu, D.; Lyubovskiy, M.R.; Altman, E.; Pfefferle, L.D.; Datye, A. Catalytic combustion of methane over palladium-based catalysts. *Catal. Rev.* **2002**, *44*, 593–649. [[CrossRef](#)]
31. Gélín, P.; Primet, M. Complete oxidation of methane at low temperature over noble metal based catalysts: A review. *Appl. Catal. B* **2002**, *39*, 1–37. [[CrossRef](#)]
32. Yang, J.; Guo, Y.B. Nanostructured perovskite oxides as promising substitutes of noble metals catalysts for catalytic combustion of methane. *Chin. Chem. Lett.* **2018**, *29*, 252–260. [[CrossRef](#)]
33. Bashan, V.; Ust, Y. Perovskite catalysts for methane combustion: Applications, design, effects for reactivity and partial oxidation. *Int. J. Energy Res.* **2019**, *43*, 7755–7789. [[CrossRef](#)]
34. Nkinahamira, F.; Yang, R.J.; Zhu, R.S.; Zhang, J.W.; Ren, Z.Y.; Sun, S.L.; Xiong, H.F.; Zeng, Z.Y. Current progress on methods and technologies for catalytic methane activation at low temperatures. *Adv. Sci.* **2022**, 2204566. [[CrossRef](#)]
35. Arandiyani, H.; Wang, Y.; Sun, H.Y.; Rezaei, M.; Dai, H.X. Ordered meso- and macroporous perovskite oxide catalysts for emerging applications. *Chem. Commun.* **2018**, *54*, 6484–6502. [[CrossRef](#)]
36. Zhang, C.X.; Zhao, P.Y.; Liu, S.X.; Yu, K. Three-dimensionally ordered macroporous perovskite materials for environmental applications. *Chin. J. Catal.* **2019**, *40*, 1324–1338. [[CrossRef](#)]
37. Velez, O.D.; Jede, T.A.; Lobo, R.F.; Lenhoff, A.M. Porous silica via colloidal crystallization. *Nature* **1997**, *389*, 447–448. [[CrossRef](#)]
38. Harkins, W.D. A general theory of the mechanism of emulsion polymerization. *J. Am. Chem. Soc.* **1947**, *69*, 1428–1444. [[CrossRef](#)]
39. Jiang, S.; Sudol, E.D.; Dimonie, V.L.; El-Aasser, M.S. Seeding as a means of controlling particle size in dispersion polymerization. *J. Appl. Polym. Sci.* **2008**, *108*, 4096–4107. [[CrossRef](#)]
40. Hartlen, K.D.; Athanasopoulos, A.P.T.; Kitaev, V. Facile preparation of highly monodisperse small silica spheres (15 to >200 nm) suitable for colloidal templating and formation of ordered arrays. *Langmuir* **2008**, *24*, 1714–1720. [[CrossRef](#)]
41. Lin, J.; Zhao, L.S.; Zheng, Y.; Xiao, Y.H.; Yu, G.T.; Zheng, Y.; Chen, W.; Jiang, L.L. Facile strategy to extend stability of simple component-alumina-supported palladium catalysts for efficient methane combustion. *ACS Appl. Mater. Interfaces* **2020**, *12*, 56095–56107. [[CrossRef](#)] [[PubMed](#)]
42. Lin, J.; Chen, Y.L.; Liu, X.J.; Chen, X.H.; Zheng, Y.; Huang, F.; Xiao, Y.H.; Zheng, Y.; Jiang, L.L. Microstructural property regulation and performance in methane combustion reaction of ordered mesoporous alumina supported palladium-cobalt bimetallic catalysts. *Appl. Catal. B* **2020**, *263*, 118269. [[CrossRef](#)]
43. Ryoo, R.; Joo, S.H.; Jun, S. Synthesis of highly ordered carbon molecular sieves via template-mediated structural transformation. *J. Phys. Chem. B* **1999**, *103*, 7743–7746. [[CrossRef](#)]
44. Yan, H.W.; Blanford, C.F.; Holland, B.T.; Smyrl, W.H.; Stein, A. General synthesis of periodic macroporous solids by templated salt precipitation and chemical conversion. *Chem. Mater.* **2000**, *12*, 1134–1141. [[CrossRef](#)]
45. Sadakane, M.; Horiuchi, T.; Kato, N.; Takahashi, C.; Ueda, W. Facile preparation of three-dimensionally ordered macroporous alumina, iron oxide, chromium oxide, manganese oxide, and their mixed-metal oxides with high porosity. *Chem. Mater.* **2007**, *19*, 5779–5785. [[CrossRef](#)]
46. Xu, J.F.; Liu, J.; Zhao, Z.; Xu, C.M.; Zheng, J.X.; Duan, A.J.; Jiang, G.Y. Easy synthesis of three-dimensionally ordered macroporous La<sub>1-x</sub>K<sub>x</sub>CoO<sub>3</sub> catalysts and their high activities for the catalytic combustion of soot. *J. Catal.* **2011**, *282*, 1–12. [[CrossRef](#)]
47. Arandiyani, H.; Dai, H.X.; Deng, J.G.; Wang, Y.; Sun, H.Y.; Xie, S.H.; Bai, B.Y.; Liu, Y.X.; Ji, K.M.; Li, J.H. Three-dimensionally ordered macroporous La<sub>0.6</sub>Sr<sub>0.4</sub>MnO<sub>3</sub> supported Ag nanoparticles for the combustion of methane. *J. Phys. Chem. C* **2014**, *118*, 14913–14928. [[CrossRef](#)]
48. Wang, Z.W.; Deng, J.G.; Liu, Y.X.; Yang, H.G.; Xie, S.H.; Wu, Z.X.; Dai, H.X. Three-dimensionally ordered macroporous CoCr<sub>2</sub>O<sub>4</sub>-supported Au–Pd alloy nanoparticles: Highly active catalysts for methane combustion. *Catal. Today* **2017**, *281*, 467–476. [[CrossRef](#)]
49. Wang, Y.; Arandiyani, H.; Scott, J.; Akia, M.; Dai, H.X.; Deng, J.G.; Aguey-Zinsou, K.-F.; Amal, R. High performance Au–Pd supported on 3D hybrid strontium-substituted lanthanum manganite perovskite catalyst for methane combustion. *ACS Catal.* **2016**, *6*, 6935–6947. [[CrossRef](#)]

50. Xu, P.; Zhao, X.T.; Zhang, X.; Bai, L.; Chang, H.Q.; Liu, Y.X.; Deng, J.G.; Guo, G.S.; Dai, H.X. Three-dimensionally ordered macroporous LaMnAl<sub>11</sub>O<sub>19</sub>- supported Pd nanocatalysts highly active for methane combustion. *Mol. Catal.* **2017**, *439*, 200–210. [[CrossRef](#)]
51. Li, X.Y.; Liu, Y.X.; Deng, J.G.; Xie, S.H.; Zhao, X.T.; Zhang, Y.; Zhang, K.F.; Arandiyán, H.; Guo, G.S.; Dai, H.X. Enhanced catalytic performance for methane combustion of 3DOM CoFe<sub>2</sub>O<sub>4</sub> by co-loading MnO<sub>x</sub> and Pd–Pt alloy nanoparticles. *Appl. Surf. Sci.* **2017**, *403*, 590–600. [[CrossRef](#)]
52. Pei, W.B.; Liu, Y.X.; Deng, J.G.; Zhang, K.F.; Hou, Z.Q.; Zhao, X.T.; Dai, H.X. Partially embedding Pt nanoparticles in the skeleton of 3DOM Mn<sub>2</sub>O<sub>3</sub>: An effective strategy for enhancing catalytic stability in toluene combustion. *Appl. Catal. B* **2019**, *256*, 117814. [[CrossRef](#)]
53. Pei, W.B.; Dai, L.Y.; Liu, Y.X.; Deng, J.G.; Jing, L.; Zhang, K.F.; Hou, Z.Q.; Han, Z.; Rastegarpanah, A.; Dai, H.X. PtRu nanoparticles partially embedded in the 3DOM Ce<sub>0.7</sub>Zr<sub>0.3</sub>O<sub>2</sub> skeleton: Active and stable catalysts for toluene combustion. *J. Catal.* **2020**, *385*, 274–288. [[CrossRef](#)]
54. Han, Z.; Fang, J.Y.; Xie, S.H.; Deng, J.G.; Liu, Y.X.; Dai, H.X. AuRu/ Meso -Mn<sub>2</sub>O<sub>3</sub>: A Highly Active and Stable Catalyst for Methane Combustion. *IOP Conf. Ser. Mater. Sci. Eng.* **2018**, *359*, 012022. [[CrossRef](#)]
55. Lou, Y.; Ma, J.; Hu, W.D.; Dai, Q.G.; Wang, L.; Zhan, W.C.; Guo, Y.L.; Cao, X.-M.; Guo, Y.; Hu, P.; et al. Low-temperature methane combustion over Pd/H-ZSM-5: Active Pd sites with specific electronic properties modulated by acidic sites of H-ZSM-5. *ACS Catal.* **2016**, *6*, 8127–8139. [[CrossRef](#)]
56. Petrov, A.W.; Ferri, D.; Kröcher, O.; van Bokhoven, J.A. Design of stable palladium-based zeolite catalysts for complete methane oxidation by postsynthesis zeolite modification. *ACS Catal.* **2019**, *9*, 2303–2312. [[CrossRef](#)]
57. Luo, L.; Wang, S.; Fan, C.; Yang, L.; Wu, Z.W.; Qin, Z.F.; Zhu, H.Q.; Fan, W.B.; Wang, J.G. Promoting effect of alkali metal cations on the catalytic performance of Pd/H-ZSM-5 in the combustion of lean methane. *Appl. Catal. A* **2020**, *602*, 117678. [[CrossRef](#)]
58. Chen, J.J.; Giewont, K.; Walker, E.A.; Lee, J.; Niu, Y.B.; Kyriakidou, E.A. Cobalt-induced PdO formation in low-loading Pd/BEA catalysts for CH<sub>4</sub> oxidation. *ACS Catal.* **2021**, *11*, 13066–13076. [[CrossRef](#)]
59. Han, Z.; Dai, L.Y.; Liu, Y.X.; Deng, J.G.; Jing, L.; Zhang, Y.X.; Zhang, K.F.; Zhang, X.; Hou, Z.Q.; Pei, W.B.; et al. AuPd/Co<sub>3</sub>O<sub>4</sub>/3DOM MnCo<sub>2</sub>O<sub>4</sub>: Highly active catalysts for methane combustion. *Catal. Today* **2021**, *376*, 134–143. [[CrossRef](#)]
60. Chen, C.-Q.; Li, W.; Cao, C.-Y.; Song, W.-G. Enhanced catalytic activity of perovskite oxide nanofibers for combustion of methane in coal mine ventilation air. *J. Mater. Chem.* **2010**, *20*, 6968. [[CrossRef](#)]
61. Arandiyán, H.; Scott, J.; Wang, Y.; Dai, H.X.; Sun, H.Y.; Amal, R. Meso-molding three-dimensional macroporous perovskites: A new approach to generate high-performance nanohybrid catalysts. *ACS Appl. Mater. Interfaces* **2016**, *8*, 2457–2463. [[CrossRef](#)] [[PubMed](#)]
62. Yuan, J.; Dai, H.X.; Zhang, L.; Deng, J.G.; Liu, Y.X.; Zhang, H.; Jiang, H.Y.; He, H. PMMA-templating preparation and catalytic properties of high-surface-area three-dimensional macroporous La<sub>2</sub>CuO<sub>4</sub> for methane combustion. *Catal. Today* **2011**, *175*, 209–215. [[CrossRef](#)]
63. Gao, Q.X.; Wang, X.F.; Wu, X.C.; Tao, Y.R.; Zhu, J.J. Mesoporous zirconia nanobelts: Preparation, characterization and applications in catalytic methane combustion. *Microporous Mesoporous Mater.* **2011**, *143*, 333–340. [[CrossRef](#)]
64. Zhang, Y.J.; Deng, J.G.; Zhang, L.; Qiu, W.G.; Dai, H.X.; He, H. AuO<sub>x</sub>/Ce<sub>0.6</sub>Zr<sub>0.3</sub>Y<sub>0.1</sub>O<sub>2</sub> nano-sized catalysts active for the oxidation of methane. *Catal. Today* **2008**, *139*, 29–36. [[CrossRef](#)]
65. Zhao, X.T.; Zhang, R.; Liu, Y.X.; Deng, J.G.; Xu, P.; Yang, J.; Han, Z.; Hou, Z.Q.; Dai, H.X.; Au, C.-T. In-situ reduction-derived Pd/3DOM La<sub>0.6</sub>Sr<sub>0.4</sub>MnO<sub>3</sub>: Good catalytic stability in methane combustion. *Appl. Catal. A* **2018**, *568*, 202–212. [[CrossRef](#)]
66. Guo, G.S.; Lian, K.; Gu, F.B.; Han, D.M.; Wang, Z.H. Three dimensionally ordered macroporous Pd–LaMnO<sub>3</sub> self-regeneration catalysts for methane combustion. *Chem. Commun.* **2014**, *50*, 13575–13577. [[CrossRef](#)] [[PubMed](#)]
67. Saalfrank, J.W.; Maier, W.F. Directed evolution of noble-metal-free catalysts for the oxidation of CO at room temperature. *Angew. Chem. Int. Ed.* **2004**, *43*, 2028–2031. [[CrossRef](#)] [[PubMed](#)]
68. Paredes, J.R.; Díaz, E.; Díez, F.V.; Ordóñez, S. Combustion of methane in lean mixtures over bulk transition-metal oxides: Evaluation of the activity and self-deactivation. *Energy Fuels* **2009**, *23*, 86–93. [[CrossRef](#)]
69. Liotta, L.F.; Wu, H.; Pantaleo, G. Co<sub>3</sub>O<sub>4</sub> nanocrystals and Co<sub>3</sub>O<sub>4</sub>–MO<sub>x</sub> binary oxides for CO, CH<sub>4</sub> and VOC oxidation at low temperatures: A review. *Catal. Sci. Technol.* **2013**, *3*, 3085–3102. [[CrossRef](#)]
70. Li, D.Y.; Li, K.Z.; Xu, R.D.; Zhu, X.; Wei, Y.G.; Tian, D.; Cheng, X.M.; Wang, H. Enhanced CH<sub>4</sub> and CO oxidation over Ce<sub>1-x</sub>Fe<sub>x</sub>O<sub>2-δ</sub> hybrid catalysts by tuning the lattice distortion and the state of surface iron species. *ACS Appl. Mater. Interfaces* **2019**, *11*, 19227–19241. [[CrossRef](#)]
71. Zhang, K.; Peng, X.B.; Cao, Y.N.; Yang, H.G.; Wang, X.Y.; Zhang, Y.Y.; Zheng, Y.; Xiao, Y.H.; Jiang, L.L. Effect of MnO<sub>2</sub> morphology on its catalytic performance in lean methane combustion. *Mater. Res. Bull.* **2019**, *111*, 338–341. [[CrossRef](#)]
72. Liotta, L.F.; Di Carlo, G.; Pantaleo, G.; Deganello, G. Catalytic performance of Co<sub>3</sub>O<sub>4</sub>/CeO<sub>2</sub> and Co<sub>3</sub>O<sub>4</sub>/CeO<sub>2</sub>–ZrO<sub>2</sub> composite oxides for methane combustion: Influence of catalyst pretreatment temperature and oxygen concentration in the reaction mixture. *Appl. Catal. B* **2007**, *70*, 314–322. [[CrossRef](#)]
73. Tao, F.F.; Shan, J.-J.; Nguyen, L.; Wang, Z.Y.; Zhang, S.R.; Zhang, L.; Wu, Z.L.; Huang, W.X.; Zeng, S.B.; Hu, P. Understanding complete oxidation of methane on spinel oxides at a molecular level. *Nat. Commun.* **2015**, *6*, 7798. [[CrossRef](#)] [[PubMed](#)]
74. Royer, S.; Duprez, D. Catalytic oxidation of carbon monoxide over transition metal oxides. *ChemCatChem* **2011**, *3*, 24–65. [[CrossRef](#)]

75. Li, H.F.; Lu, G.Z.; Qiao, D.S.; Wang, Y.Q.; Guo, Y.; Guo, Y.L. Catalytic methane combustion over  $\text{Co}_3\text{O}_4/\text{CeO}_2$  composite oxides prepared by modified citrate sol-gel method. *Catal. Lett.* **2011**, *141*, 452–458. [[CrossRef](#)]
76. Zhang, X.Y.; Liu, Z.M.; Wei, Z.L.; Du, X.C.; Gong, M.C.; Chen, Y.Q. Preparation of high performance methane combustion catalyst and its application to natural gas catalytic combustion fan-boiler. *Chin. J. Catal.* **2006**, *27*, 823–826. [[CrossRef](#)]
77. Yuan, X.; Meng, L.Q.; Xu, Z.W.; Zheng, C.H.; Zhao, H.B. CuO quantum dots supported by  $\text{SrTiO}_3$  perovskite using the flame spray pyrolysis method: Enhanced activity and excellent thermal resistance for catalytic combustion of CO and  $\text{CH}_4$ . *Environ. Sci. Technol.* **2021**, *55*, 14080–14086. [[CrossRef](#)]
78. Rui, Z.B.; Huang, Y.F.; Zheng, Y.; Ji, H.B.; Yu, X. Effect of titania polymorph on the properties of CuO/TiO<sub>2</sub> catalysts for trace methane combustion. *J. Mol. Catal. A Chem.* **2013**, *372*, 128–136. [[CrossRef](#)]
79. Li, J.H.; Fu, H.J.; Fu, L.X.; Hao, J.M. Complete combustion of methane over indium tin oxides catalysts. *Environ. Sci. Technol.* **2006**, *40*, 6455–6459. [[CrossRef](#)]
80. Zeng, S.H.; Fu, X.J.; Zhou, T.Z.; Wang, X.M.; Su, H.Q. Influence of pore distribution on catalytic performance over inverse  $\text{CeO}_2/\text{Co}_3\text{O}_4$  catalysts for  $\text{CH}_4/\text{CO}_2$  reforming. *Fuel Process. Technol.* **2013**, *114*, 69–74. [[CrossRef](#)]
81. Zarur, A.J.; Ying, J.Y. Reverse microemulsion synthesis of nanostructured complex oxides for catalytic combustion. *Nature* **2000**, *403*, 65–67. [[CrossRef](#)] [[PubMed](#)]
82. Habibi, N.; Arandiyani, H.; Rezaei, M. Mesoporous  $\text{MgO}\cdot\text{Al}_2\text{O}_3$  nanopowder-supported meso-macroporous nickel catalysts: A new path to high-performance biogas reforming for syngas. *RSC Adv.* **2016**, *6*, 29576–29585. [[CrossRef](#)]
83. Wang, Y.J.; Guo, M.N.; Lu, J.Q.; Luo, M.F. Mesoporous alumina supported PdO catalysts for catalytic combustion of methane. *Chin. J. Catal.* **2014**, *32*, 1496–1501. [[CrossRef](#)]
84. Zhang, J.J.; Li, J.W.; Zhu, J.Q.; Wang, Y.; Chen, B.H. Effect of promoter on the performance of Cu-Mn complex oxide monolithic catalysts for lean methane catalytic combustion. *Chin. J. Catal.* **2011**, *32*, 1380–1386. [[CrossRef](#)]
85. Du, X.C.; Liu, Z.M.; Luo, Y.Y.; Chen, Y.Q.; Gong, M.C. Methane combustion over  $\text{Co}_3\text{O}_4/\text{YSZ}-\gamma\text{-Al}_2\text{O}_3 + \text{CZY}$  monolithic catalysts. *Acta Chim. Sin.* **2005**, *63*, 1651–1655.
86. Chen, Q.Q.; Zhang, L.J.; Chen, Y.Q.; Wang, M.; Gong, M.C. Effect of  $\text{Ce}_{0.67}\text{Zr}_{0.33}\text{O}_2$  on Catalytic properties of  $\text{Fe}_2\text{O}_3/\text{Al}_2\text{O}_3$  catalyst for methane combustion. *Chem. J. Chin. Univ.* **2005**, *26*, 1704–1708.
87. Chen, Y.D.; Zhu, Y.; Wang, J.L.; Chen, Y.Q.; Gong, M.C. Influence of  $\text{CeZrYLaO}$  solid solution on performance of  $\text{Fe}_2\text{O}_3$ -based monolith catalyst for catalytic combustion of methane. *Chin. J. Inorg. Chem.* **2009**, *25*, 1771–1778.
88. Wang, Y.; Shang, H.Y.; Xu, H.D.; Gong, M.C.; Chen, Y.Q. Effects of ZnO content on the performance of  $\text{Pd}/\text{Zr}_{0.5}\text{Al}_{0.5}\text{O}_{1.75}$  catalysts used in lean-burn natural gas vehicles. *Chin. J. Catal.* **2014**, *35*, 1157–1165. [[CrossRef](#)]
89. Wang, Y.; Xu, H.D.; Shang, H.Y.; Gong, M.C.; Chen, Y.Q. Excellent complete conversion activity for methane and CO of  $\text{Pd}/\text{TiO}_2-\text{Zr}_{0.5}\text{Al}_{0.5}\text{O}_{1.75}$  catalyst used in lean-burn natural gas vehicles. *J. Energy Chem.* **2014**, *23*, 461–467. [[CrossRef](#)]
90. Svensson, E.E.; Nassos, S.; Boutonnet, M.; Järås, S.G. M Microemulsion synthesis of MgO-supported  $\text{LaMnO}_3$  for catalytic combustion of methane. *Catal. Today* **2006**, *117*, 484–490. [[CrossRef](#)]
91. Thaicharoensutcharittham, S.; Meeyoo, V.; Kitiyanan, B.; Rangsunvigit, P.; Rirksomboon, T. Catalytic combustion of methane over  $\text{NiO}/\text{Ce}_{0.75}\text{Zr}_{0.25}\text{O}_2$  catalyst. *Catal. Commun.* **2009**, *10*, 673–677. [[CrossRef](#)]
92. Zhang, Y.J.; Niu, J.R.; Wang, G.Z.; Li, D.; Dai, H.X.; He, H.; Qiu, W.G. Investigation on catalytic behaviors of  $\text{PdO}/\text{nano-Ce}_{0.6}\text{Zr}_{0.35}\text{Y}_{0.05}\text{O}_2$  in methane oxidation. *J. Rare Earths* **2006**, *24*, 1–5.
93. Zhang, Y.J.; Wang, G.Z.; Zhang, L.; Dai, H.X.; He, H.; Zi, X.H. Synthesis, characterization and catalytic properties of three-dimensional wormhole-like mesoporous  $\text{Ag}_2\text{O}/\text{Ce}_{0.6}\text{Zr}_{0.35}\text{Y}_{0.05}\text{O}_2$  nanoparticles in methane oxidation. *Chem. J. Chin. Univ.* **2007**, *28*, 1929–1934.
94. Zavyalova, U.; Scholz, P.; Ondruschka, B. Influence of cobalt precursor and fuels on the performance of combustion synthesized  $\text{Co}_3\text{O}_4/\gamma\text{-Al}_2\text{O}_3$  catalysts for total oxidation of methane. *Appl. Catal. A Gen.* **2007**, *323*, 226–233. [[CrossRef](#)]
95. Zheng, Y.N.; Li, K.Z.; Wang, H.; Zhu, X.; Wei, Y.G.; Zheng, M.; Wang, Y.H. Enhanced activity of  $\text{CeO}_2\text{-ZrO}_2$  solid solutions for chemical-looping reforming of methane via tuning the macroporous structure. *Energ. Fuel.* **2016**, *30*, 638–647. [[CrossRef](#)]
96. Zhang, Y.; Zhang, L.; Deng, J.G.; Dai, H.X.; He, H. Hydrothermal fabrication and catalytic properties of  $\text{YBa}_2\text{Cu}_3\text{O}_7$  single crystallites for methane combustion. *Catal. Lett.* **2010**, *135*, 126–134. [[CrossRef](#)]
97. Peng, H.G.; Rao, C.; Zhang, N.; Wang, X.; Liu, W.M.; Mao, W.T.; Han, L.; Zhang, P.F.; Dai, S. Confined ultrathin Pd-Ce nanowires with outstanding moisture and  $\text{SO}_2$  tolerance in methane combustion. *Angew. Chem. Int. Ed.* **2018**, *57*, 8953–8957. [[CrossRef](#)]
98. Cargnello, M.; Jaén, J.J.D.; Garrido, J.C.H.; Bakhmutsky, K.; Montini, T.; Gámez, J.J.C.; Gorte, R.J.; Fornasiero, P. Exceptional activity for methane combustion over modular  $\text{Pd@CeO}_2$  subunits on functionalized  $\text{Al}_2\text{O}_3$ . *Science* **2012**, *337*, 713–717. [[CrossRef](#)]
99. Arandiyani, H.; Dai, H.X.; Ji, K.M.; Sun, H.Y.; Li, J.H. Pt nanoparticles embedded in colloidal crystal template derived 3D ordered macroporous  $\text{Ce}_{0.6}\text{Zr}_{0.3}\text{Y}_{0.1}\text{O}_2$ : Highly efficient catalysts for methane combustion. *ACS Catal.* **2015**, *5*, 1781–1793. [[CrossRef](#)]
100. Xu, P.; Wu, Z.X.; Deng, J.G.; Liu, Y.X.; Xie, S.H.; Guo, G.S.; Dai, H.X. Catalytic performance enhancement by alloying Pd with Pt on ordered mesoporous manganese oxide for methane combustion. *Chin. J. Catal.* **2017**, *38*, 92–105. [[CrossRef](#)]
101. Yao, Y.X.; Giapis, K.P. Direct hydrogenation of dinitrogen and dioxygen via Eley-Rideal reactions. *Angew. Chem.* **2016**, *128*, 11767–11771. [[CrossRef](#)]
102. Kumar, K.V.; Porkodi, K.; Rocha, F. Langmuir-Hinshelwood kinetics—A theoretical study. *Catal. Commun.* **2008**, *9*, 82–84. [[CrossRef](#)]

103. Widmann, D.; Behm, R.J. Dynamic surface composition in a Mars-van Krevelen type reaction: CO oxidation on Au/TiO<sub>2</sub>. *J. Catal.* **2018**, *357*, 263–273. [[CrossRef](#)]
104. Jørgensen, M.; Grönbeck, H. First-principles microkinetic modeling of methane oxidation over Pd(100) and Pd(111). *ACS Catal.* **2016**, *6*, 6730–6738. [[CrossRef](#)]
105. Tang, Z.Y.; Zhang, T.; Luo, D.C.; Wang, Y.J.; Hu, Z.; Yang, R.T. Catalytic combustion of methane: From mechanism and materials properties to catalytic performance. *ACS Catal.* **2022**, *12*, 13457–13474. [[CrossRef](#)]
106. Stotz, H.; Maier, L.; Boubnov, A.; Gremminger, A.T.; Grunwaldt, J.-D.; Deutschmann, O. Surface reaction kinetics of methane oxidation over PdO. *J. Catal.* **2019**, *370*, 152–175. [[CrossRef](#)]
107. Li, X.S.; Wang, X.; Roy, K.; Bokhoven, J.A.; Artiglia, L. Role of water on the structure of palladium for complete oxidation of methane. *ACS Catal.* **2020**, *10*, 5783–5792. [[CrossRef](#)]
108. Hou, Z.Q.; Dai, L.Y.; Deng, J.G.; Zhao, G.F.; Jing, L.; Wang, Y.S.; Yu, X.H.; Gao, R.Y.; Tian, X.R.; Dai, H.X.; et al. Electronically engineering water resistance in methane combustion with an atomically dispersed tungsten on PdO catalyst. *Angew. Chem. Int. Ed.* **2022**, *134*, e202201655. [[CrossRef](#)]
109. Huang, W.X.; Zhang, X.R.; Yang, A.C.; Goodman, E.D.; Kao, K.C.; Cargnello, M. Enhanced catalytic activity for methane combustion through in situ water sorption. *ACS Catal.* **2020**, *10*, 8157–8167. [[CrossRef](#)]
110. Yang, W.W.; Gong, J.; Wang, X.; Bao, Z.H.; Guo, Y.B.; Wu, Z.L. A review on the impact of SO<sub>2</sub> on the oxidation of NO, hydrocarbons, and CO in diesel emission control catalysis. *ACS Catal.* **2021**, *11*, 12446–12468. [[CrossRef](#)]
111. Auvinen, P.; Hirvi, J.T.; Kinnunen, N.M.; Suvanto, M. PdSO<sub>4</sub> surfaces in methane oxidation catalysts: DFT studies on stability, reactivity, and water inhibition. *ACS Catal.* **2020**, *10*, 12943–12953. [[CrossRef](#)]
112. Somorjai, G. On the mechanism of sulfur poisoning of platinum catalysts. *J. Catal.* **1972**, *27*, 453–456. [[CrossRef](#)]
113. Harris, P.J.F. Sulphur-induced faceting of platinum catalyst particles. *Nature* **1986**, *323*, 792–794. [[CrossRef](#)]
114. Kitchin, J.R.; Nørskov, J.K.; Barteau, M.A.; Chen, J.G. Modification of the surface electronic and chemical properties of Pt(111) by subsurface 3d transition metals. *J. Chem. Phys.* **2004**, *120*, 10240–10246. [[CrossRef](#)] [[PubMed](#)]

**Disclaimer/Publisher's Note:** The statements, opinions and data contained in all publications are solely those of the individual author(s) and contributor(s) and not of MDPI and/or the editor(s). MDPI and/or the editor(s) disclaim responsibility for any injury to people or property resulting from any ideas, methods, instructions or products referred to in the content.